MECHANISMS OF ORDERED GAMMA PRIME PRECIPITATION IN NICKEL BASE SUPERALLOYS

Antariksh Rao Pratap Singh, B. Tech., M. Tech.

Dissertation Prepared for the Degree of

DOCTOR OF PHILOSOPHY

UNIVERSITY OF NORTH TEXAS

May 2011

APPROVED:

Rajarshi Banerjee, Major Professor
Srinivasan Srivilliputhur, Committee Member
Jincheng Du, Committee Member
Narendra Dahotre, Committee Member and Chair of the Department of Materials Science and Engineering
Junyeon Hwang, Committee Member
James D. Meernik, Acting Dean of the Toulouse Graduate School

Singh, Antariksh Rao Pratap. Mechanisms of ordered gamma prime precipitation in nickel base superalloys. Doctor of Philosophy (Materials Science and Engineering), May 2011, 154 pp., 10 tables, 45 illustrations, references, 196 titles.

Commercial superalloys like Rene88DT are used in high temperature applications like turbine disk in aircraft jet engines due to their excellent high temperature properties, including strength, ductility, improved fracture toughness, fatigue resistance, enhanced creep and oxidation resistance. Typically this alloy’s microstructure has L12-ordered precipitates dispersed in disordered face-centered cubic γ matrix. A typical industrially relevant heat-treatment often leads to the formation of multiple size ranges of γ¢ precipitates presumably arising from multiple nucleation bursts during the continuous cooling process. The morphology and distribution of these γ′ precipitates inside γ matrix influences the mechanical properties of these materials. Therefore, the study of thermodynamic and kinetic factors influencing the evolution of these precipitates and subsequent effects is both relevant for commercial applications as well as for a fundamental understanding of the underlying phase transformations. The present research is primarily focused on understanding the mechanism of formation of different generations of γ′ precipitates during continuous cooling by coupling scanning electron microscopy (SEM), energy filtered TEM and atom probe tomography (APT). In addition, the phase transformations leading to nucleation of γ′ phase has been a topic of controversy for decades. The present work, for the first time, gives a novel insight into the mechanism of order-disorder transformations and associated phase separation processes at atomistic length scales, by coupling high angle annular dark field (HAADF) – STEM imaging and APT. The results indicate that multiple competing mechanisms can operate during a single continuous cooling process leading to different generations of γ′ including a non-classical mechanism, operative at large undercoolings.

ACKNOWLEDGEMENTS

It gives me a great sense of gratitude to thank my advisor, Dr. Rajarshi Banerjee for his esteemed guidance and support throughout this research and giving me an opportunity to have him as my mentor. His keen insight in research and motivation and made me grow as a researcher and am indebted to him for building in the confidence in me to present this work. On a personal level, he has been there as a guardian through the crests and troughs of life and I deeply respect him and his family (Didi and Ritu) for everything that he has done for me.

I would also like to thank Dr. Hamish Fraser from Ohio State University; Dr. Babu Viswanathan and Dr. Jaymie Tiley from Air Force Research Laboratory and the faculties from my department- Dr. Narendra Dahotre, Dr. Srinivasan G. Srivilliputhur, Dr. Jincheng Du, Dr. Alan Needleman, Dr. Richard F. Reidy, Dr. Thomas Scharf, Dr. Nigel Shepherd, Dr. Nandika A. D'Souza for their constant support and guidance. Dr. Junyeon Hwang and Dr. Soumya Nag have always motivated me, guided me throughout my research and thank them for being like elder brothers at personal level.

I would also like to thank my friends Arun, Sundeep, Peeyush, Ankit, Anchal, Polly, Ye, Sandeep, Sailesh, Amanda, Derek, Lynn, Mohammad, Vaibhav and Benedict for making my stay at UNT a memorable one.

Last but not the least, I would like to thank my mother, father, sister, brother, my beloved fiancée and my extended family for their love, encouragement and support and make me stand where I am today. I dedicate this to Daddy, Mummy, Danny Bhaiya and Mona.

TABLE OF CONTENTS

ACKNOWLEDGEMENTS iii

LIST OF TABLES vii

LIST OF ILLUSTRATIONS viii

Chapters

1. INTRODUCTION 1

2. LITERATURE REVIEW 3
    - 2.1 Introduction 3
    - 2.2 Physical Metallurgy of Nickel Base Superalloys 4
    - 2.3 Influence of Cooling Rate on Precipitation of γ’ 9
    - 2.4 Multimodal Precipitation of γ′ During Continuous Cooling 12
    - 2.5 Transformation Mechanism Involving Ordering and Phase Separation 16
    - 2.6 Coarsening of γ′ 21
    - 2.7 References 24

3. PROCESSING AND CHARACTERIZATION TOOLS 31
    - 3.1 Alloy Preparation 31
    - 3.2 Thermal Treatment 32
    - 3.3 Experimental Tools 33
        - 3.3.1 Mechanical Cutting and Polishing 33
        - 3.3.2 Chemical and Electrochemical Procedures 33
        - 3.3.4 Scanning Electron Microscopy 34
        - 3.3.5 Transmission Electron Microscopy 36
        - 3.3.6 Synchrotron Based X-ray Diffraction 38
        - 3.3.7 Atom Probe Tomography 40
    - 3.4 References 44

4. INFLUENCE OF COOLING RATE ON THE MICROSTRUCTURAL EVOLUTION IN RENE 88DT....45

4.1 Introduction....45

4.2 Experimental Procedure....46

4.3 Variation in Microstructure as a Function of Cooling Rate....47

4.4 Compositional Analysis as a Function of Different Cooling Rates....57

4.5 Precipitation of γ' as a Function of Different Cooling Rate Conditions....64

4.6 Summary....69

4.7 References....70

5. FORMATION OF DIFFERENT GENERATIONS OF γ' PRECIPITATES DURING CONTINOUS COOLING....71

5.1 Introduction....71

5.2 Experimental Procedure....72

5.3 Multiple Nucleation Bursts of γ' Precipitates Probed In-situ Using Synchrotron Studies....73

5.4 Development of γ' Precipitates Size, Distribution and Morphology During Continuous Cooling....79

5.5 Chemical Partitioning Between γ' and γ for Different Generations of Precipitates....85

5.6 Formation Mechanism of Multiple Bursts of Nucleation....93

5.7 Summary....96

5.8 References....97

6. GROWTH OF DIFFERENT GENERATIONS OF γ' DURING AGING....98

6.1 Introduction....98

6.2 Experimental Procedure....99

6.3 Changes in Size, Distribution and Morphology of Primary γ' During Growth....101

6.4 Changes in Size, Distribution and Morphology of Secondary γ' During Growth....105

6.5 Changes in γ' and γ Composition During Growth....109

6.6 Summary....115

6.7 References....116

7. DECOMPOSITION PATHWAY INVOLVING ORDER-DISORDER TRANSFORMATION AND PHASE SEPARATION 117

7.1 Introduction....................117

7.2 Experimental Procedure....................119

7.3 Investigation of Early Stages of Decomposition Leading to γ′ Formation....................120

7.4 Growth of γ′ Precipitates During Isothermal Annealing....................136

7.5 Summary....................149

7.6 References....................150

8. SUMMARY AND FUTURE WORK 152

LIST OF TABLES

3.1 Bulk composition of Rene88DT 31

4.1 Variation in number density and inter-particle distance with cooling rate 56

4.2 γ′ compositions for WQ0, FC0 and SC0 condition..60

4.3 γ composition in WQ0, FC0 and SC0 condition...62

6.1 Primary γ′ composition in SC1, SC10 and SC15 condition...113

6.2 Tertiary γ′ composition in SC1, SC10 and SC15 condition...114

6.3 Depletion zone γ composition in SC1, SC10 and SC15 condition......................................114

7.1 Composition of γ′ as a function of aging time 145

7.2 Composition of γ as a function of aging time 146

7.3 Composition of Cr rich and Cr depleted regions and their volume fraction predicted by LBM 148

LIST OF FIGURES

2.1. Crystal structure of (a) γ and (b) γ′ 4

2.2 Schematic showing spinodal decomposition 8

3.1 Experimental set up of in-situ high energy x-ray diffraction at advanced photon Source 40

3.2 Schematic diagram of a three dimensional atom probe 41

3.3 The projection geometry of an atom probe sample 43

4.1 Energy-filtered transmission electron microscopy (EFTEM) images constructed using Cr M edge in the EELS spectrum from solutionized and water-quenched WQ0 sample. The γ′ precipitates, which are Cr depleted, exhibit the darker grey contrast in these Images 47

4.2 Energy-filtered transmission electron microscopy (EFTEM) images constructed using Cr M-edge in the EELS spectrum from solutionized and fast cooled FC0 sample. The γ′ precipitates, which are Cr depleted, exhibit the darker grey contrast in these images 49

4.3 Energy-filtered transmission electron microscopy (EFTEM) images constructed using Cr M-edge in the EELS spectrum from solutionized and slow cooled SC0 sample. The γ′ precipitates, which are Cr depleted, exhibit the darker grey contrast in these images 51

4.4 Energy-filtered transmission electron microscopy (EFTEM) images constructed using Cr M-edge in the EELS spectrum from solutionized and (a) fast cooled FC0 sample and (b) slow cooled SC0 sample, showing. The γ′ precipitates, which are Cr depleted, exhibit the darker grey contrast in these images 53

4.5 Energy-filtered transmission electron microscopy (EFTEM) images constructed using Cr M-edge in the EELS spectrum from solutionized and slow cooled SC0 sample, showing secondary and tertiary γ' precipitates. The γ′ precipitates, which are Cr depleted, exhibit the darker grey contrast in these images 55

4.6 (a) 3DAP reconstruction of Co (blue) and Al (red) atoms in WQ0 atom probe sample. The γ′ precipitates are the Al-rich red regions with Co-rich blue matrix. (b) Different depiction of the same WQ0 3-D reconstruction showing Cr = 14at% isosurfaces 57

4.7 (a) FC0 3-D reconstruction showing Cr = 14at% isosurfaces of primary and secondary γ′ precipitates. (b) SC0 3-D reconstruction showing Cr = 14at% isosurfaces of primary and secondary γ′ precipitates 59

4.8 Schematic showing the formation of different generations of γ′ precipitates with different cooling rates WQ0 and SC0......64

5.1 (a) Variation of (100) intensity at different temperatures during continuous cooling at 25ºCmin^{-1}, (b) Variation of (111) intensity at different temperatures during continuous cooling at 25ºCmin^{-1} 74

5.2 (a) Variation of (100) intensity at different temperatures during continuous cooling at 5ºCmin^{-1}, (b) Variation of (111) intensity at different temperatures during continuous cooling at 5ºCmin^{-1} 76

5.3 Intensity ratio plots for samples cooled at (a) 24ºCmin^{-1} and (b) 5ºCmin^{-1}............................77

5.4 (a) Backscatter SEM image showing primary γ′ precipitates in SC0, (b) Higher magnification backscatter image showing cuboidal to irregular shaped γ′..80

5.5 Energy-filtered transmission electron microscopy (EFTEM) images constructed using Cr M-edge in the EELS spectrum from solutionized and slow cooled SC0 sample (a) showing primary and secondary γ′ and (b) showing small tertiary γ′ between secondary γ′ and depletion zone. The γ′ precipitates, which are Cr depleted, exhibit the darker grey contrast in these images...............81

5.6 Frequency size distribution of multiple generations of γ′..83

5.7 (a) 3DAP reconstruction of Co (blue) and Al (red) atoms in SC0 atom probe sample. The γ′ precipitates are the Al-rich red regions with Co-rich blue matrix. (b) Different depiction of the same SC0 3-D reconstruction showing Cr = 14at% isosurfaces and Ni ions in green showing primary and tertiary γ′. (c) Another region of same SC0 sample 85

5.8 (a) Proxigram showing the composition profiles of Co, Ti, Cr, Al and Mo atoms across primary γ′/γ interface (b) enlarged view of Al and Ti composition profile close to interface, (b) enlarged view of Cr composition profile close to interface...87

5.9 (a) 2-D composition map of Cr showing variation in composition in the matrix (yellow being Cr depleted and red being Cr enriched), also showing Cr = 14at% isosurface (c) 2-D composition may of Cr showing some regions highly depleted in Cr, (c) Cr = 18at% isosurface showing primary γ′, depletion zone and interconnected network of γ′ 89

5.10 (a) Proxigram showing the composition profiles of Co, Ti, Cr, Al and Mo atoms across tertiary γ′/ γ interface (b) Comparison of Al and Cr composition profile across the interface for primary and tertiary γ′...92

5.11 (a) Schematic showing (a) primary γ′ and composition profile ahead of γ′ formed at low undercooling, (b) Non-equilibrium composition in far γ and second nucleation burst (c) Composition profile and third nucleation burst at very high undercooling..................................93

6.1 Secondary electron image of (a) SC1 (b) SC10 and (c) SC15 showing primary γ′ precipitates, in immersion mode of SEM...101

6.2 Normalized frequency size distribution for primary γ′ precipitates in (a) SC1 (b) SC10 and (c) SC15 condition 103

6.3 Energy-filtered transmission electron microscopy (EFTEM) images constructed using Cr M-edge in the EELS spectrum from solutionized, slow cooled and aged (a) SC1 sample showing primary, secondary and tertiary γ′ and (b) SC10 sample showing tertiary γ′ between secondary γ′ and depletion zone. The γ′ precipitates, which are Cr depleted, exhibit the darker grey contrast in these images 105

6.4 Energy-filtered transmission electron microscopy (EFTEM) images constructed using Cr M-edge in the EELS spectrum from solutionized, slow cooled and aged (a) SC15 sample showing primary, secondary and tertiary γ′ and (b) SC15 sample showing grown small tertiary γ′ between secondary γ′ and depletion zone. The γ′ precipitates, which are Cr depleted, exhibit the darker grey contrast in these images 107

6.5 Normalized frequency size distribution of secondary γ′ precipitates in SC1 and SC15 condition showing increased size of secondary γ′ 108

6.6 3D atom probe reconstruction with Ni ions in green and γ′ precipitates delineated by Cr = 14at% isosurface showing primary and tertiary γ′ in (a) SC1, (b) SC10 and (c) SC15 condition 109

6.7 Compositional profile of Al, Ti, Co, Cr and Mo across primary γ′ and depletion zone in (a) SC1, (b) SC10 and (c) SC15 condition 112

7.1 Selected area diffraction pattern of EWQ sample along <001> showing 4-fold symmetry, ordered spots and satellite reflections 120

7.2 (a) RAW HAADF-STEM image of EWQ taken along <011> zone, (b) Background subtracted same HAADF-STEM image 122

7.3 (a) RAW HAADF-STEM image of EWQ taken along <011> zone, (b) Background subtracted same HAADF-STEM image 123

7.4 (a) 3DAP reconstruction of EWQ sample with Ni ions in green and Cr = 18at% isosurface, (b) enlarged section of same reconstruction showing interconnected morphology 124

7.5 (a) Proximity histogram of Al, Ti, Cr, Co and Mo of Cr = 14at% isosurface, (b) 3DAP reconstruction of EWQ sample with Ni ions in green and Cr = 14at% isosurface 126

7.6 2-D compositional map showing (a) Al rich (red) and Al depleted regions (blue), (b) Cr rich (blue) and Al depleted regions (red) regions 128

7.7 Filtered HAADF-STEM image showing dark-disordered (blue), dark-ordered (yellow) and bright-disordered (red) regions 129

7.8 (a) Dark ordered region (b) bright disordered region (c) dark disordered region. (d) Intensity profiles along <002> direction in dark-ordered, bright disordered and dark disordered regions 131

7.9 (a) Simplified G-X plot showing Order-Disorder transformation pathway, (b) Schematic of growth of spinodal wave and ordering process with time 134

7.10 3DAP reconstruction showing Ni ions and in green and Cr = 14at% isosurface for (a) EWQ, (b) EWQ + 1min, (c) EWQ + 5min, (d) EWQ + 30min and (e) EWQ + 60min aged, sample ...136

7.11 Dark field image taken along <001> zone showing ordered γ′ in (a) EWQ +1min aged , (b) EWQ +5 min aged sample. Dark field image taken along <011> zone showing ordered γ′ in (c) EWQ +30 min aged, (d) EWQ +60 min aged sample 138

7.12 Frequency size distribution of γ′ precipitates using dark field imaged for (a) EWQ + 1min, (b) EWQ + 5min and (c) EWQ + 30min condition 141

7.13 Proxigram of Cr 14at% isosurface as a function of aging time, (a) EWQ, (b) EWQ + 1min, (c) EWQ + 5min, (d) EWQ + 30min and (e) EWQ + 60min aged, sample.................................144

7.14 Normalized LBM plot showing phase separation of Cr with aging 148

CHAPTER 1

INTRODUCTION

Various classes of materials have made a significant contribution to high temperature applications due to their remarkable properties. Their ability to tolerate extreme conditions has made them a strong candidate for jet engine and gas-based turbines. The efficiency of these engines and turbines depends directly on the operating temperatures close to the melting point of these materials. Nickel base superalloy is one class of these materials that have shown substantial resistance to time dependent irrecoverable mechanical degradation called creep. These structural materials have shown excellent mechanical properties maintained over long period of time due to the microstructural stability. Oxidation and corrosion resistance under such conditions also forms a unique characteristic of these alloys.

The strength of these alloys depends primarily of the ordered strengthening precipitates called gamma prime (γ') dispersed in the gamma (γ) matrix. The finite lifetime of these alloys depends on the microstructure and its evolution with time. The properties depend on the microstructure of the alloy, which are directly influenced by the composition and heat treatments involved. Optimal properties have been known to exist for microstructures that have multimodal distribution of precipitates. Even though, multimodal distribution of precipitates has been studied in the past, the interplay of thermodynamic and kinetic factors has been of interest and still being researched upon. In addition, the mechanism of formation of these ordered γ' precipitates involving ordering and phase separation has been a topic of controversy.

The contribution of this thesis is three fold. First, this study shows the effect of cooling rate on the morphology and distribution of γ' precipitates and variation in the partitioning of different alloying elements in a commercial nickel base superalloy, Rene88DT. Second, the mechanism of formation of different generations of γ' precipitates during continuous cooling of Rene88DT is proposed. This was achieved by studying the chemical partitioning of elements for different generations of γ' arising from the interplay between thermodynamic and kinetic factors. The third and final contribution of thesis is to give an insight to the phase transformation occurring at atomistic length scales. It is shown that in contradictory to classical nucleation mechanism that is assumed for different generations of γ', non-classical nucleation mechanism can exist for γ' formed at high undercoolings. A complete transformation pathway involving disorder-order transformation and phase separation by spinodal decomposition resulting in the formation of ordered γ' has been postulated in complex nickel base superalloy, Rene88DT.

CHAPTER 2

LITERATURE REVIEW

2.1 Introduction

Superalloys have become an integral part of land based gas turbines and blades and discs of jet engines in aviation industry. The performance and efficiency of these engines depend on the temperatures at which these engines operate and hence the temperatures that materials see inside the engine. Gas based turbines require materials that can withstand high temperatures and generate enough power. Titanium alloys are used when weight is a consideration, but due to their poor oxidation resistance their applications are limited to ones that operate at temperatures below 700^{o}C [1]. Some power plants use ferritic steels that have high strength and good creep resistance. But latest generation supercritical steam turbines require long life at temperatures around 750^{o}C. The increasing demand for higher efficiency turbine engines has led to the development of superalloys for turbine disc and blade applications that can resist higher temperatures beyond 800^{o}C [2]. One class of these materials, nickel base superalloys have shown excellent high temperature properties like strength, corrosion resistance due to their high temperature microstructural stability [3-7]. These materials also possess significant resistance to loading under static, creep and fatigue conditions. Superalloys in jet engines are used in different sections like blades and discs. Blades operate under very high pressure and temperature and therefore require excellent creep properties. This is achieved by usage of single crystals for blades. However the discs are usually polycrystalline materials. Rene88DT is one such material used for disc application in General Electric jet engines [8]. Even though these alloys have good properties, the microstructural changes due to change in operating temperatures can vary the properties of the material and hence it becomes very important to understand these changes.

2.2 Physical Metallurgy of Nickel Base Superalloys

Nickel superalloys usually have a lot of alloying elements present. These elements are often greater than ten in number where each element has a particular role in terms of the behavior. Most of the alloys contain significant amount of Co, Cr, Ti and Al. Some small amounts of boron, carbon, zirconium etc are also added. 4d and 5d block elements are also present in these superalloys, which make their chemistry fairly complex [4]. The behavior of each element depends on its position in the periodic table, and based on that elements can be divided into different classes where a set of elements show similar behavior. Ni, Co, Fe, Cr, Ru, Mo, Re and W have atomic radii close to Ni, partition to gamma (γ) phase and stabilize it. Al, Ta and Ti on the other hand have larger atomic radii and stabilize gamma prime (γ′). B, C and Zr form a different class of elements that segregate to grain boundaries of γ phase [8].

The microstructure of superalloy due to the presence of a number of alloying elements can exhibit different phases.

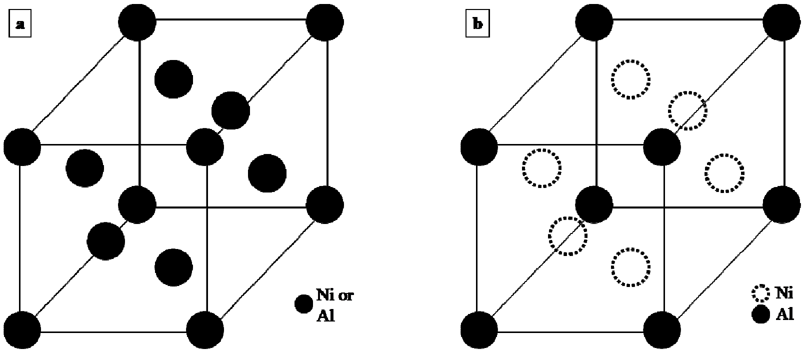

Figure 2.1. Crystal structure of (a) γ and (b) γ′.

(i) The gamma (γ) phase as shown in Fig. 2.1(a) which is a disordered phase and forms the matrix of superalloys, exhibits face centered cubic (FCC) structure and is the softer phase amongst different phases. [100] of γ phase is elastically softest direction along which the γ′ phase tends to grow [8].

(ii) The gamma prime (γ') phase as shown in Fig 2.1(b) is the ordered phase which gives strength to the material at elevated temperatures. This phase is coherent with the γ phase and possesses significant covalent bonding and has $L1_2$ ordered structure, similar to Ni_3Al where Al occupies the cube corners and Ni occupies the face centers. In multi component systems elements that partition to γ' typically occupy the Al sublattice, however mixed behavior has been observed for Cr, Fe and Mn. Lattice parameter of γ' is 3.59 A^o whereas that of γ is 3.58 A^o. Ti and Ta that have large atomic radii favor the Al sublattice whereas Co which has smaller atomic radii prefers Ni. The ordered nature of γ' has been directly observed by Hono [9] using ladder diagrams. This phase exhibits a cube-cube relationship with the γ phase in Ni-Al system.

$$\{100\}\gamma \,//\, \{100\}\gamma'$$

$$<010>\gamma \,//\, <010>\gamma'$$

Even when different elements are added, this relationship is still maintained. However, the misfit between the two phases as described changes,

$$\delta = 2 \text{ x } [(a_{\gamma'} - a_{\gamma}) / (a_{\gamma'} + a_{\gamma})]$$

where $a_{\gamma'}$ and a_{γ} are the lattice parameters of γ' and γ respectively. Partitioning of different elements changes this mismatch between the two phases which can significantly affect the properties of the superalloy.

In addition to γ and γ' phases, other phases can exist in nickel base superalloys depending on the composition. In nickel-iron superalloys that contain significant amount of Nb, the primary strengthening elements are not γ' but a body centered cubic structure that has $D0_{22}$ structure based on the composition Ni_3Nb [10]. The lattice parameters *a* and *b* of this phase are nearly equal to that of γ' but the *c* is doubled and therefore this phase is commonly knows as γ''. These precipitates have disc shaped morphology and impart excellent high temperature properties due to limited slip systems present in this phase. However tendency of nucleating δ phase [11-12] at the grain boundaries at the expense of γ'' has been observed which has orthorhombic structure. This phase does not impart any strength to the material even if present in significant amount. Elements like Cr, Mo, W and Re if present in excess quantities may lead to the formation of TCP or topologically close-packed phases that can vary in chemical composition and crystal structure like rhombohedral and orthorhombic. These phases have high packing density of atoms, degree of non-metallic bonding and complex crystal structures.

In many superalloys rich in Cr, Mo, Ti, Ta or Hf, carbide or boride phases can form in the presence of C and B in traces. These carbides and borides can vary in morphology and are often found in the inter-dentritic regions or at grain boundaries. The primary effect of these carbides and borides is to pin the grain boundaries and prevent grain boundary slipping at high temperatures thus enhancing the mechanical properties.

Rene88DT which is a multi-component nickel base superalloy has been used recently for its increased damage tolerance (hence DT) and fatigue crack growth compared to earlier generations of nickel base superalloy like Rene 95 for turbine disc applications [6, 7, 13]. It has a nominal composition: 13% Co, 16% Cr, 4% Mo, 4% W, 2.1% Al, 3.7% Ti, 0.7% Nb, 0.03% C and 0.015% B (all in wt%). The equilibrium volume fraction of γ' and γ are 43.4% and 56.6% respectively as calculated using PANDAT software. Equilibrium composition of γ' is 10.3% Al, 2.3% Co, 3.1% Cr, 0.2% Mo, 1% Nb, 10.4% Ti and 0.2% W (all in at%). Equilibrium composition of γ is 0.05% Al, 20.9% Co, 29.2% Cr, 4.1% Mo, 2.2% W (all in at%). This material is usually processed using powder metallurgy (PM) and develops polycrystalline microstructure with fine grain size due to PM processing. A typical heat-treatment that is used for this alloy consists of a solutionizing procedure for 30 to 60 minutes at 1150°C (2100°F) in the single γ phase field, followed by continuous cooling to room temperature at appropriate cooling rates, and subsequent aging for different time periods at temperatures such as 760°C (1400°F). The primary strengthening elements in this material are the γ' precipitates that are distributed inside the γ matrix. The precipitation mechanisms leading to γ' formation involve diffusion of solute and therefore come under the category of diffusional transformation. This may occur either by classical nucleation and growth or by spinodal decomposition. In classical nucleation and growth mechanism, a nucleus of equilibrium composition of different phase forms to reduce the total free energy of the system given by

$$\Delta G = -V\ \Delta Gv + A\gamma_I + V\ \Delta Gs$$

Where, ΔG is total free energy change associated with transformation, V is volume of nucleus, ΔGv is volumetric free energy change, A is surface area of nucleus, γ_I is interfacial energy, ΔGs is strain energy change. The nucleation process therefore involves an activation barrier $\Delta G^* = A16\pi\gamma_I^3 / 3\ (\Delta Gv - \Delta Gs)^2$ required for precipitation of second phase and a large compositional fluctuation. Also when homogeneous nucleation occurs, the rate of nucleation depends highly on the temperature or the undercooling at which the precipitation occurs given by $N_{hom} = \omega C_o \exp(\Delta G_m/kT) \exp(\Delta G^*/kT)$ where ω is a factor that includes vibrational frequency and area of critical nucleus, C_o are the number of atoms in nucleus of second phase, ΔG_m is the activation energy for atom migration, k is Boltzmann constant and T is temperature. During nucleation process the strain energy contribution is minimal due to very small size of nuclei and therefore precipitates at early stages have spherical shape to minimize interfacial energy. However, during growth process, the morphology of precipitates may change due to increase in strain energy discussed later in the literature.

The precipitate of a second phase may also occur by a different mechanism where there is no activation barrier for nucleation. This is usually found when the precipitation occurs at very low temperatures in some systems. Such a process known as spinodal decomposition occurs when the curvature of free energy is negative around the average composition of the system. Due to negative curvature, as shown in Fig. 2.2 the system can lower its energy by small compositional fluctuations growing with time to reach phases with equilibrium composition.

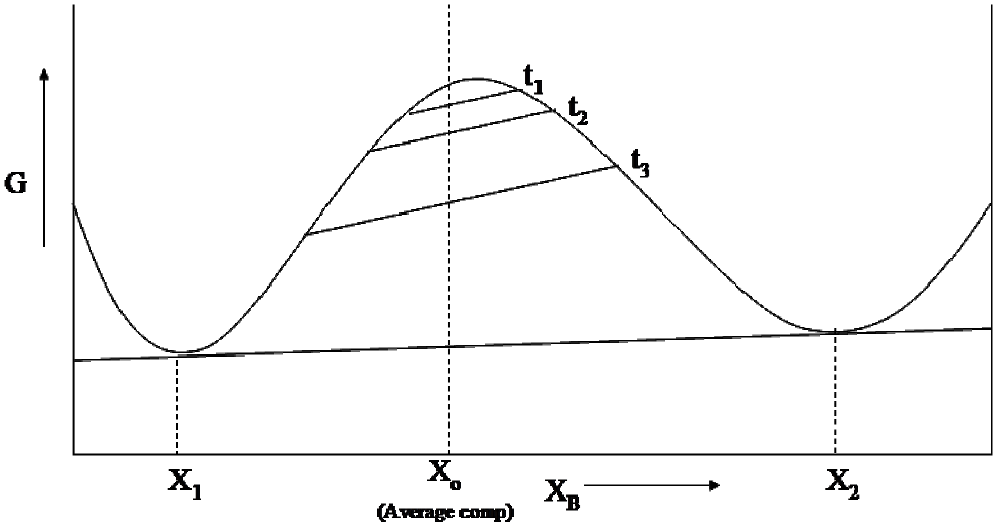

Figure 2.2. Schematic showing spinodal decomposition.

In multi component system as mentioned earlier different elements can preferentially go to Ni or Al sublattice depending on their site occupancy [14]. The inherent ordered nature of these ordered precipitates, which are stable even at high temperatures, gives this material very high strength and good creep properties at elevated temperatures. These properties are imparted to the alloy by a variety of mechanisms. These are formation of antiphase boundaries during dislocation interaction in the precipitates [15] and formation of stress fields arising from coherency of the precipitates and matrix. The partitioning of various elements like Al, Ti, Co, Cr etc cause changes in the lattice parameter [16] and therefore change the coherency of matrix and precipitates which can change the properties of material.

2.3 Influence of Cooling Rate on Precipitation of γ'

The partitioning of elements depends highly on the cooling rate (due to change in diffusivity) and hence the dependence of cooling rate on the composition of γ and γ' is important. Owing to polycrystalline nature of the matrix, the γ' precipitates are found to be both intra-granular as well as at the grain boundaries. However the distribution, size and morphology of these precipitates depend highly on the processing route and the heat treatments involved. It has been found that rate of cooling and grain size effect the serrations at the ground boundary during cooling affect the mechanical properties and therefore study of cooling rate effect on the microstructural evolution becomes extremely important. Variation in microstructure due to variations in cooling rate has been studied in the recent past. Formation of monomodal precipitates is observed at high cooling rates after solutionizing the material in the single γ phase field [17-24]. These precipitates possess relatively high nucleation density, which has been observed with different characterization techniques [22-26]. Due to limited growth of these precipitates they maintain close to spherical morphology [17]. However, in a slow cooled condition or when the material is cooled at relatively slower cooling rates after solutionizing, multiple size ranges of precipitates are formed. Even though study on multiple stage heat treatment leading to multiple size ranges of precipitates has been done in the past [27-30], formation of multiple size ranges of precipitates due to multiple nucleation events occurring [18, 19, 31-34] is still being researched upon. Even though there has been an extensive research done on the morphology of these precipitates using energy filtered transmission electron microscopy (EFTEM) and transmission electron microscopy (TEM), very limited work has been done on the mechanisms that lead to the formation of these precipitates. With the development of atom probe tomography, the compositional partitioning between the ordered γ' and disordered γ matrix leading to the different precipitate size distributions has been studied. Effect of cooling rates on the size distribution of the γ' precipitates and subsequently the properties has been of particular interest since the volume fraction, size, morphology and distribution can be controlled [35, 36]. This effect has also been compared with phase field modeling [19-21]. Tian studied Ni based PM alloy, FGH4096 and demonstrated that the average size of the primary γ' precipitates changes inversely with the cooling rate and that the morphology of primary γ' precipitates changes from butterfly like to spherical with increase in cooling rate. Some research results also showed increase in volume fraction of larger γ' precipitates with decrease in cooling rate [37]. The experimental results have also shown increase in hardness, yield strength and ultimate tensile strength with increase in cooling rate [38]. The results have shown a power law relationship between cooling rate and size scale of the precipitate (larger γ' precipitates only) for U720LI alloy [39]. Similar study was done by Mao [40] on Rene88 and concluded that the sizes of primary γ' ranged from 0.04 - 0.2 micron when the cooling rate varied from 11 to $167^{o}\mathrm{Cmin}^{-1}$ and that the size followed power law with cooling rate with an exponent of 0.47. All the studies showed a normal distribution of precipitate sizes for all the cooling rates both for primary (large sized) and secondary (small sized) precipitates. In such studies the γ' has also found to vary in shape between different cooling rates as a result of changing diffusivities. With the decrease in cooling rate the γ' precipitates were found to change their morphology from spherical to cuboidal. Babu et al. [18] studied the effects of cooling rate on the microstructure and chemical partitioning of various elements between γ and γ'. It was found that with increase in cooling rate the morphology of γ' particles changed from spherical to irregular shaped. Water quenched samples showed γ' with close to spherical morphology whereas slow cooled showed a bimodal distribution of precipitates with larger precipitates with cuboidal to irregular morphology. The size of larger precipitates was found to decrease with increase in cooling rate and number density increased. Negligible change in partitioning of elements for larger precipitates was found with change in cooling rate whereas changes in Al concentration was noted for smaller precipitates. Similar results were also reported by Jackson et al. [41]. He found out that the size of the precipitates decreased from 72nm to 37nm as the cooling rate increased from 0.08 to 0.33 Ks^{-1}. The number density was also found to increase with increase in cooling rate. Behrouzghaemi [42] showed morphological changes with change in cooling rate and got similar results. Mitchell and Preuss [43] studied the influence of cooling rate on the constrained and unconstrained lattice mismatch between γ and γ′ using high energy synchrotron x-ray diffraction in a polycrystalline UDIMET720 alloy. The constrained lattice mismatch was found to change little with cooling rate due to the presence of elastic strains in the material. However, the unconstrained lattice mismatch determined by extracting the γ′ from the matrix showed change in lattice mismatch with cooling rate possibly due to change in composition of Al and Ta inside the γ and γ′ which was speculated. Since the unconstrained lattice mismatch can only be truly related to the change in chemical composition, the mismatch calculated will only be due to partitioning of elements that have different atomic radii. It was deduced that higher amounts of Al was present in γ′ at faster cooling rate as compared to Ta, whereas at slower cooling rates higher amount of Ta was present in γ′. The slower cooling rate also showed a bimodal distribution of precipitates as compared to monomodal in case of faster cooling rate. Michell and Preuss [44] in their later study on alloy UC01 found out using differential scanning calorimetry experiments that γ′ precipitation temperature decreases with cooling rate and intermediate cooling rates resulted in minimum lattice mismatch. Grosdidier [45] analyzed the effect of cooling rate on the γ- γ′ transformation and γ′ morphology for two nickel based superalloys, AM1 and CMSX-2. It was found that the transformation temperature decreased with the increase in cooling rate and the γ' morphology changed from spherical to irregular with the decrease in cooling rate. Mackay and Natal [46] studied Ni-Al-Mo-Ta alloy and found out that forced air cooling resulted in the formation of coarser precipitates as compared to oil quenching, however, the sizes and cooling rates were not quantified in the study. All these studies alluded to that fact that with decrease in cooling rate the size distribution of γ' particles changes from unimodal to bimodal or multimodal. It also suggests that the mechanism of formation of these precipitates also varies with changing cooling rate. Therefore, the study of the cooling rate effect and the underlying mechanisms becomes important from the scientific point of view. This study is also relevant from industrial view point as processing of superalloys in industry typically involves two step heat treatment for optimizing, size, distribution and volume fraction of strengthening γ' precipitates for obtaining optimal mechanical properties. Since the first heat treatment involves cooling of material from solvus temperature, the distribution and size of precipitates becomes important.

2.4 Multimodal Precipitation of γ' During Continuous Cooling

The formation of multiple size ranges of γ' precipitates during slow cooling due to multiple nucleation events occurring is a complex process due to the interplay of multiple factors. In recent times this phenomenon has been researched upon, however, a clear understanding of the interplay of the factors is lacking and hence this work is aimed to understand these complex processes. Hwang et al. [47] studied the compositional variations between different generations of γ' precipitates using atom probe tomography and found out that the compositions of different size ranges of precipitates were different. In addition to that, the composition of γ matrix was also found to be different near the primary versus near secondary γ'

precipitates. An important observation was also made by Hwang that the interface width (compositional gradient) between precipitate and matrix for primary and secondary precipitates were different and that it was more for secondary than primary. In other words, the interface width was found to be sharp for primary and diffused for secondary. This was the first attempt to compare the interface widths between different generations of γ' precipitates. It alluded to the fact that the compositional partitioning between different generations of γ' and matrix is different. Formation of bimodal microstructures has been reported in several literatures, however, not much emphasis has been given on clearly understanding the formation of different generations of γ' experimentally [18, 19, 48-50]. Recently, the formation of bimodal/multimodal microstructure of γ' precipitates in superalloys has been simulated using phase field modeling. The phase field modeling modeling has a lot of advantages over other numerical simulations. It has the ability to predict realistic microstructures while incorporating effects of strain, diffusion fields around the precipitates, overlapping diffusion fields etc. Dynamic evolution of microstructures, variation in shapes and morphology of precipitates during growth and coarsening has also been successfully predicted using phase field modeling. Earlier, the phase field model could only be used for isothermal conditions while accounting for variations in thermodynamic parameters also called field variables like composition and long range order parameter. However for non isothermal conditions like continuous cooling experiments, the driving force for nucleation continuously changes. Langer-Schwartz [51] developed a new phase field model to account for this limitation which could predict microstructure involving concurrent nucleation and growth processes. It was able to predict particle size distribution (PSD) for non isothermal heat treatment conditions. However, one major limitation of Langer-Schwartz approach was that it was only able to predict the particle size distributions and not the interparticle spacing. In other words, for same PSD different microstructures could exist. Later, the work by Wendt and Hassen [52] and Kampmann and Wagner [53] accounted for the supersaturation and non linear contributions to capillarity. In recent work by researchers, the evolution of microstructure in superalloys was modeled using long range parameter that was solved using time dependent Ginzburgh-Langdau equation [54], whereas, the composition filed variable was described using Cahn-Hilliard diffusion equation [55]. These equations described the spatial variation of these field variables with time and thus can predict realistic microstructure. The free energy of the system that described in these equations itself had both chemical and elastic free energy components to account for strain effects involved in the transformation. The chemical free energy component was described by Cahn-Hilliard equations for non uniform systems which include the addition gradient energy term [56]. The elastic contributions were accommodated by the Kachaturyan's Green's function for homogenous elasticity [57] coupled with Vegards law to account for lattice mismatch occurring in the system due to compositional changes. Wen [20] simulated the microstructure evolution in superalloys for continuous cooling conditions and found out that at intermediate cooling rates, the first nucleation burst is shut off by soft impingement or the interaction of the diffusion fields around the precipitates. However with decreasing temperature during continuous cooling, supersaturation builds up and at high undecooling a second burst of nucleation occurs. Hence, a bimodal microstructure is obtained by two successive nucleation events. Simmons [58] in similar studies found out that at very high cooling rates the thermally activated processes like diffusion are not able to continue at low temperatures and soft impingement condition never arises and inter-particle spacing never reaches the diffusion distance. On the other hand, in non isothermal processes the first nucleation event is shut of by soft impingement and precipitates grow and coarsen with continuous decrease in temperature until sufficient buildup of supersaturation occurs which leads to second nucleation event. The nucleation continues until the inter-particle spacing reaches the diffusion distance. Sarosi [19] in their recent work on Rene101 in which the alloy was solutionized, cooled at $5^{o}Cmin^{-1}$ and air quenched at particular interrupt temperatures found out that bimodal distribution was obtained both for high interrupt temperatures and low interrupt temperatures. This was also confirmed using phase filed modeling on a binary Ni-Al system with various cooling sequences. However, it was postulated that the second nucleation burst during high and low interrupt temperatures occurred during air quenching and $5^{o}Cmin^{-1}$ cooling respectively and air quenching was not able to suppress nucleation for high interrupt temperature cooling sequences. This study even though didn't represent the true microstructure of continuous cooling heat treatments; it was able to demonstrate the concept of formation of bimodal microstructure arising due to two nucleation events. This phenomenon was also suggested by Furrer by his study on U720Li alloy resulting in multimodal distribution of γ' particles. Each nucleation event occurring at different temperature happens in different chemistry of γ phase. The initial nucleation event is controlled by nucleation kinetics of supersaturated matrix; however, the second nucleation event depends on diffusion kinetics at lower temperature, initially precipitated γ' and the solute lean γ matrix.

Gabb [59] developed a physics based kinetic model for γ' precipitation in nickel base superalloy and was verified and calibrated for PM processed CH98 alloy. This model was based on classical nucleation and diffusion growth processes and considered different thermodynamic factors such as excess free energy, supersaturation build up, nucleation, growth and coarsening. This model was able to predict mean γ' sizes, volume fraction and number densities. It gave reasonable predictions of multiple nucleation events and was validated with experimental procedures. Radis [60] in his recent study on U720Li investigated the multiple nucleation events experimentally and by modeling during continuous cooling condition. Three different population of γ′ precipitates were observed, however due to limitation of experimental procedures, the size distribution was only limited to primary precipitates. The computer simulation for the precipitation process was done using MatCalc software [61-63], which is based, on classical nucleation theory extended for multicomponent systems [61, 64, 65]. The simulations were in a good agreement with the experimental observations; however, it was found that the simulation results were very sensitive to the diffusional mobilities. In addition, this study did not discuss the composition of the precipitates and all the growth processes resulted in spherical precipitates, which was also the assumption. The simulation also neglected the effect of coarsening of precipitates and its influence on the later nucleation bursts.

2.5 Transformation Mechanism Involving Ordering and Phase Separation

The precipitation of ordered γ′ phase has been a topic of great interest for a long time. During continuous cooling of supersaturated γ phase from the solvus temperature, the precipitation of γ′ can occur via different mechanisms i.e. nucleation and growth or spinodal decomposition. The precipitation mechanism would depend on free energy plot of the system and the average composition of the matrix. However, this process of precipitation becomes more complex due to the disorder-order transformation of γ to γ′ phase. It is well known theoretically and validated experimentally in many systems that phase separation and ordering processes can occur simultaneously during decomposition; however, the transformation pathway in many systems is not very well understood and has been researched upon for decades. Different approaches have been proposed in binary alloy systems in which clustering and ordering seems to play crucial role in determining the precipitation of coherent, metastable of stable $L1_2$ ordered phase in a disordered FCC matrix. It is known that spinodal decomposition in early stages results in a modulated structure, however, Ardell and Nicholson [66] in their study on Ni-6.71wt% Al alloy demonstrated that spinodal decomposition is not a pre requisite for a modulated structure when an alloy is quenched from high temperature. They showed that periodic arrangement of γ' particles can result from alignment during coarsening and that the sizes of the particles follow $t^{1/3}$ law. The TEM observations showed that the alignment of γ' particle is a result of elastic interactions between precipitates and the matrix and this alignment is more pronounced with increasing volume fraction of γ' (increasing supersaturation). Phillips [67] also showed using transmission electron microscopy that when Ni-12.7at% Al is quenched, precipitation of γ' phase occurs by classical nucleation and growth mechanism. It was also demonstrated that these ordered domains exhibited cuboidal shape during initial stages when their size was 5nm. These precipitates also showed alignment when coarsened at 600 and 700^{o}C. Hill and Ralph [68] however showed that in Ni-14wt% Al quenched alloy using atom probe FIM investigations showed a continuous phase separation mechanism for γ' precipitation. They demonstrated that by selection one particular wavelength of compositional modulation, aging of the material provides a negative interdiffusion coefficient. Cahn in his earlier study showed that using general diffusion equation for spinodal decomposition [69] in elastically isotropic medium and including the effect of strain [70] results in a solution that has a negative interdiffusion coefficient. The study by Hill and Ralph resulted in an interdiffusion coefficient of -4×10^{-19} for two probing directions <110> and <111>. Wendt and Hassen [71] refuted the results of Hill and Ralph based on two observations: all the wave numbers with $b < b_c$ (critical wave number) did not increase with aging time and the composition profile for their shortest aging time revealed precipitates that had stoichiometric Ni_3Al composition. Wendt and Hassen with same alloy composition demonstrated that from initial stages the Al enriched regions had the composition of fully developed γ'. During initial stages of aging, the particle size remained constant and the number density increased and in later stages particles grew in proportion to $t^{1/3}$. Gentry and Fine's study on Ni-13.8at% Al [72] showed that that the supersaturated solid solution became increasingly inhomogeneous during aging. This corresponded to a decomposition of supersaturated solid solution though compositional fluctuations those were large in extent but small in degree. Their work was indicative of the transformation proposed by Cahn-Hilliard non classical nucleation or spinodal decomposition. However, in their study on Ni-11.1at% Al the results showed that the decomposition path for this alloy was different and proceeded by classical nucleation and growth in which the compositional modulations are large in degree but small in extent. Corey [73] also showed similar results for a non stoichiometric Ni-Al alloy. However, they suggested a transformation mechanism for Ni-17at% Al rapidly helium quenched alloy. They proposed that first the supersaturated solid solution orders completely by a vacancy jump mechanism which is a second order transition and then the ordered phase spinodally decomposes which requires diffusion down a chemical potential gradient.

Ni-Ti system is similar to Ni-Al system as γ' with $L1_2$ structure is formed in this system. The equilibrium Ni_3Ti phase has a hexagonal structure; however, at high supersaturations a metastable $L1_2$ structure is formed before precipitation of hexagonal Ni_3Ti. This is primary found in systems with Ti > 10% [74]. Various experimental investigations have been done to explicate the decomposition mechanism in Ni-Ti alloys. The work by Israel and Fine [75] on solutionized and ice brine quenched Ni-10at% Ti alloy at a quench rate of approximately $1000^{o}C/min$ and subsequently annealed suggests that the process of phase transformation involved spinodal decomposition. Ni_6Ti precipitates are formed by spinodally decomposition which requires less diffusion and with time these grow and reach a critical size after which these precipitates grow as normal precipitates. With time growth of Ni_3Ti occurs and takes over Ni_6Ti. The formation of intermediate metastable γ' phase Ni_3Ti before the formation of stable hexagonal Ni_3Ti was also shown by Saito and Watanabe [76] in Ni-12at% Ti; however, the mechanism of formation of these γ' phases by either nucleation and growth or spinodal decomposition was not clearly identified. However, study by Laughlin [77] on Ni -10at% Ti and Ni-12at% Ti using TEM revealed than in as quenched alloy the phase separation occurs via spinodal decomposition. In addition to that, the mechanism of formation of γ' was also proposed. It was proposed that in both these alloys ordering reaction starts after that spinodal reaction suggesting that the ordering instability lies below the spinodal curve. Appearance of satellite spots around the center spot and absence of superlattice reflection in selected area diffraction pattern for as quenched situation and appearance of superlattice reflection with aging confirmed the presence of this transformation pathway. These results were similar to those observed in Cu-Ti alloys [78-80]. Cerri and coworkers [81, 82] studied the early stages of ordering and phase separation in Ni-1.5at% Ti alloy that was water quenched and aged at 540^oC for different time periods. Even though special precautions were taken while water quenching, it was not possible to suppress the ordering reaction in the system during quenching. Using x-ray and transmission electron microscopy it was observed that metastable Ni_3Ti was formed during quenching and in beam small angle-neutron scattering (SANS) measurements showed that phase separation occurs while aging. Even though order-disorder transformation path was not determined, it was shown that a state of partial order can be attained without extended compositional fluctuations in Ni-Ti. Sinclair et al. [83] in his study on Ni-14at% Ti suggested a transformation pathway. They used field ion microscopy to probe the initial stages of decomposition and found out that formation of metastable ordered phase Ni_3Ti in a supersaturated matrix happens via continuous ordering followed by phase separation by spinodal decomposition. It was also shown that in as quenched state, the nature of the interface between Ni_3Ti and the matrix was diffused that that it became sharper with aging. It was also found out that the spinodal temperature of this alloy was 880 +/- 70°C. Kostorz and coworkers [84, 85] used high resolution electron microscopy and small-angle neutron scattering techniques and showed that at low and moderate temperatures in supersaturated matrix of Ni-Ti, decomposition starts via continuous ordering followed by phase separation. Except for low supersaturations, this mechanism operates in low to moderate temperature range (500-700°C). Ungar with Lambrigger and Kostorz [86] also showed using high resolution and high sensitivity x-ray difffractometry that decomposition of N-Ti dilute solution involves phase separation by spinodal decomposition. Grune and Haasen [87] in their study on Ni-12at% Ti showed that in water quenched sample, phase transformation occurs by spinodal ordering and that the amplitude and wavelength of the concentration wave increases with aging time indicative of spinodal decomposition as proposed by Cahn. The experimental results were compared to computer simulations showing similar results. Therefore, it can be concluded that Ni-Ti illustrates phase separation by spinodal decomposition well.

In addition to these systems, Ni-Al-Cr [89, 90] and other superalloys [91] have also been investigated for order-disorder transformation and phase separation. However, nothing conclusive has been found out regarding the transformation mechanism involved. Ordering and clustering processes were found to be complete after 15 min of aging of Ni-5.2at%Al-14.7at%Cr at 600°C by Schmuk [92]. However, the interfacial energy and coarsening rate calculated were interpreted using classical nucleation theory which gave a critical nucleus size of 0.5nm. Wood

[93, 94] in his work on Nimonic80A and APK1 showed using APFIM and transmission electron microscopy that phase separation in these alloys which contain high chromium content involve spinodal decomposition and suggested that critical amount of Cr has to be rejected out of precipitate to form ordered γ' which occurs after phase separation. Therefore the role of Cr is important in phase separation mechanisms.

2.6 Coarsening of γ'

The change in morphology during coarsening of γ' has been of significant interest and been studied by a lot of researchers. The effect of misfit on the change in morphology of γ' has been important in superalloys. Ricks et al. [95] showed that with the increasing aging time the shape of γ' precipitates changes from spherical to cuboidal to array of cubes. Initially, when the γ' nucleates, it attains spherical morphology to minimize the interfacial energy (dependent on surface area) since the contribution due to strain energy resulting from lattice misfit is low (dependent on volume). During growth, the contribution of strain energy increases and the precipitates attain cuboidal morphology. However, further growth of the precipitates leads to increase in strain energy and system tries to minimize the free energy by splitting of γ' precipitates. This is because the decrease in strain energy is more than increase in interfacial energy. Doi and coworkers [96] created a theoretical model which agreed with the experimental investigations that the effect of strain resulting from lattice misfit can cause splitting of γ' precipitates into eight cuboids. The model also suggested that for very low lattice misfits the precipitates would not split and above certain lattice misfit the precipitates can split to form parallel platelets. Kachaturyan [97] did a theoretical analysis of the effect of strain on the change in morphology during coarsening and suggested that strain induces splitting of γ' precipitates.

However, the model was based on the assumption that the elastic constant of matrix and precipitate were same and that they both were coherent. The model was also valid for low γ' volume fraction systems where the interactions between neighboring precipitates were negligible. The model matched well with the experimental investigations done [96, 98]. γ' splitting phenomenon was also investigated by Hazotte [99] using finite element modeling and showed that the splitting of coherent γ' precipitates occurs due to the effect of strain energy. Tsukada [100] used phase field simulations to understand the role of elastic inhomogeneity on the coarsening process and showed that the particle size distribution becomes broader during coarsening with increase in volume fraction which is consistent with the investigations by Vaithyanathan and Chen [101]. However, this is limited to low volume fraction and at high volume fraction where the strain fields of neighboring precipitates interact, this effect is minimized and the splitting may not occur with increasing volume fraction. This effect of splitting is however not considered by the coarsening theories available. Precipitates growing at the expense of the smaller ones require diffusion of solute through the matrix resulting in coarsening also known as Oswald ripening [102]. Precipitate coarsening model developed by Lifshitz and Slyozov [103] and Wagner [104] also known as LSW theory of coarsening was based on zero volume fraction of precipitates such that the diffusion field of the precipitates do not interact with each other. Also, the effect of strain was neglected. The LSW theory was modified later by Ardell [105] to take into account the non-zero volume fraction of precipitates, which showed that the rate of coarsening increased with increase in equilibrium volume fraction of precipitates. Encountered modified theory (LSEM) was developed by Davies [106] which accounted for particle coalescence of two particles and change in the distribution of the particles. Several numerical and analytical models were developed later [107-111] for finite volume fraction of γ' precipitates; however, these models predicted different results using the same microscopic equations. These coarsening models were developed for isothermal heat treatments. Zhao [112] developed a mathematical model for Oswald coarsening in non–isothermal conditions, when the particle volume fraction continuously decreased. However, calculations for this model were carried out for liquid-liquid phase transformation in Zn-Pb system and therefore the effect of strain was not included in the model. Modified LSW predicted that increasing the volume fraction increases the coarsening rate; however, it has been observed in a number of γ' forming systems like Ni-Al [113], Ni-Ti [114], Ni-Ge [115], Ni-Ga [116] and Ni-Si [117,118] that the coarsening rate at low volume fractions decreases with increasing volume fraction and remain constant for very high volume fractions, typically 0.8 or greater. This anomaly has been successfully explained by trans-interface diffusion controlled coarsening model (TIDC) developed by Ardell and Ozolins [119]. This model suggests that the coarsening is controlled by the interface between disordered and ordered phase and the rate constants are independent of the change in volume fraction at large volume fractions which is more consistent with the experimental results [120-122].

2.7 References

[1] J.C. Williams, E.A. Starke, Acta Mater. 51 (2003) 5775

[2] R. Schafrik, R. Sprague, Advanced Materials and Pro. 162 (2004) 33

[3] W. Betteridge, S.W.S Shaw, Mater. Sci. Tech. 3 (1987) 682

[4] C.T. Sims, N.S. Stoloff, W.C. Hagel, Superalloys II: High-Temperature Materials for Aerospace and Industrial Power, New York: John Wiley and Sons (1987)

[5] K.A. Green, T.M. Pollock, H. Harada, Superalloy 2004: Proceedings of the Tenth International Symposium on the Superalloys, TMS (2004)

[6] D.D. Krueger, R.D. Kissinger, R.D. Menzies, C.S. Wukusick, U.S. Patent 4,957,567

[7] S.T. Wlodek, M. Kelly, D.A. Alden, in: R.D. Kissinger, D.J. Deye, D.L. Anton, A.D. Cetel, M.V. Nathal, T.M. Pollock, D.A. Woodford (Eds.), Superalloys, Warrendale (1996) 129

[8] R.C. Reed, The Superalloys: Fundamentals and Applications, Cambridge University Press, Cambridge (2006)

[9] K. Hono, Private communication, The National Institute of Materials Science, Tsukub Science City, Japan (2003)

[10] E.E. Brown, D.R. Muzyka, Nickel-iron alloys, in C.T. Sims, N.S. Stoloff, W.C. Hagel, Superalloys II: High-Temperature Materials for Aerospace and Industrial Power 1987; New York: John Wiley and Sons 165

[11] J.W. Brooks, P.J. Bridges, in D.N. Duhl, G. Maurer, S. Antolovich, C. Lund ad S. Reichman, eds, Superalloys 1988 Warrendale, PA: The Metallurgical Soc. (1988) 33

[12] R. Cozar, A. Pineau, Met. Trans. 4 (1973) 47

[13] D.D. Krueger, R.D. Kissinger, R.G. Menzies: in Superalloys 1992, S.D. Antolovich, R.W. Stusrud, R.A. Mackay, D.L. Anton, T. Khan, R.D. Kissinger, D.L. Klarstrom, eds., TMS-AIME, Warrendale (1992) 277

[14] A.V. Karg, D.E. Fornwalt, O.H. Kriege, J Inst. Met. 99 (1971) 305

[15] D. Hull, D.J. Bacon, Introduction to Dislocations; Butterworth-Heinemann Ltd

[16] Y. Mishima, S. Ochiai, T. Suzuki, Acta Metall. 33 (1985) 1161

[17] J.Y. Hwang, R. Banerjee, J. Tiley, R. Srinivasan, G.B. Viswanathan, H.L. Fraser, Metall. Mater. Trans. A. 40 (2009) 24

[18] S.S. Babu, M.K. Miller, D.A. Vitek, S.A. David, Acta Mater. 49 (2001) 4149

[19] P.M. Sarosi, B. Wang, J.P. Simmons, Y. Wang, M.J. Mills, Scripta Maert. 57 (2007) 767

[20] Y.H. Wen, J.P. Simmons, C. Shen, C. Woodword, Y. Wang, Acta Mater. 51 (2003) 1123

[21] Y.H. Wen, B. Wang, J.P. Simmons, Y. Wang, Acta Mater. 54 (2006) 2087

[22] D.N. Seidman, K.E. Yoon, R.D. Noebe, Acta Mater. 55 (2007) 1145

[23] D.N. Seidman, K.E. Yoon, R.D. Noebe, Acta Mater. 55 (2007) 1159

[24] C.K. Sudbrack, K.E. Yoon, Z. Mao, R.D. Noebe, D. Isheim, D.N. Seidman, Electron Microscopy: Its Role in Materials Science. Mike Meshii Symposium, Proceedings of Symp. (2003) 43

[25] G.B. Vishwanathan, P.M. Sarosi, M.F. Henry, D.D. Whitis, W.W. Milligan, M.J. Mills, Acta Mater. 53 (2005) 3041

[26] P.M. Sarosi, G.B. Vishwanathan, D.D. Whitis, M.J. Mills, Ultramicro. 103 (2005) 83

[27] H. J. Penkalla,J. Wosika, A. Czyrska Filemonowiczb, Materials Chemistry and Phy. 81 (2003) 417

[28] E. Balikci, D. Erdeniz, Metall. Mater. Trans. A. 41 (2010) 1391

[29] E. Balikci, A. Raman, R.A. Mirshams, Metall. Mater. Trans. A. 28 (1997) 1993

[30] E. Balikci, R.A. Mirshams, A. Raman, Z. Metallkd. 20 (1999) 132

[31] D.U. Furrer, H.J. Fecht, Scripta Mater. 40 (1999) 1215

[32] J. Mao, K.M. Chang, W. Yang, K. Ray, S.P. Vaze, D.U. Furrer, Metall. Trans. A. 32 (2001) 2441

[33] J. Mao, K.M. Chang, W. Yang, D.U. Furrer, K. Ray, S.P. Vaze, Mater. Sci. Eng. A. 332 (2002) 318

[34] R. Radis, M. Schaffer, M. Albu, G. Kothleitner, P. Polt, E. Kozeschnik, Proceedings of the International Symposium on Superalloys. (2008) 829

[35] G. Tian, C. Tia, Y. Wen, G. Liu, B. Fu, Rare Met. 27 (2008) 410

[36] F. Torster, G. Baumeister, J. Albrecht, G. Lütjering, D. Helm, M.A. Daeubler, Mater. Sci. Eng. A. 234-236 (1997) 189

[37] S.A. Sajjadi, H.R. Elahifar, H. Farhangi, J. Alloys Cmpd. 455 (2008) 215

[38] M. P. Jackson, R.C. Reedm, Mater. Sci. Eng. A. 259 (1999) 85

[39] J. Mao, K.M. Chang, W. Yang, K. Ray, Metall. Mater. Trans. A. 32 (2001) 2441

[40] J. Mao, K.M. Chang, D.U. Furrer, Mater. Design Approaches and Exp. (2001) 309

[41] M.P. Jackson, M.J. Starnik, R.C. Reed, Mater. Sci. Eng. A. 264 (1999) 26

[42] S. Behrouzghaemi, R.J. Mitchell, Mater. Sci. Eng. A. 498 (2008) 266

[43] R.J. Mitchella, M. Preussb, M.C. Hardya, S. Tinc, Mater. Sci. Eng. A. 423 (2006) 282

[44] R.J. Mitchell, M. Preuss, S. Tin, M.C. Hardy, Mater. Sci. Eng. A. 473 (2008) 158

[45] T. Grosdidier, A. Hazotte, A. Simon, Mater. Sci. Eng. A. 256 (1998) 183

[46] R.A. MacKay, M.V. Nathal. In: B.L. Bramfit, R.C. Benn, C.R. Brinkman, G.F. Vander Voort, Editors, MICON86: Optimization of Processing, Properties, and Service Performance

Through Microstructure Control (ASTM STP 979 ed.), American Society for Testing and Materials, Philadelphia (1988) 202

[47] J.Y. Hwang, S. Nag, A.R.P. Singh, R. Srinivasan, J. Tiley, G.B. Viswanathan, H.L. Fraser, R. Banerjee, Metall. Mater. Trans. A. 40 (2009) 24

[48] N. El-Bagour, A. Nofala, Mater. Sci. Eng. A. 527 (2010) 7793

[49] N. El-Bagour, M. Walya, A. Nofala, Mater. Sci. Eng. A. 487 (2008) 152

[50] G. Boussinot, A. Finel, Y. Le Bouar, Acta Mater. 57 (2009) 921

[51] J.S. Langer, A.J. Schwartz, Phys. Rev. 21 (1980) 948

[52] H. Wendt, P. Haasen, Acta Metall. 31 (1983) 1649

[53] R. Kampmann, R. Wagner. In: Decomposition of alloys: the early stage, New York (1983) 91

[54] J.D. Gunton, M.S. Miguel, P.S. Sahni, in: C. Domb, J.L. Lebowitz (Eds.), Phase Transitions and Critical Phenomena, New York (1983) 267

[55] J.W. Cahn, J.E. Hilliard, J. Chem. Phys. 28 (1958) 258

[56] J.W. Cahn, J.E. Hilliard, J. Chem. Phys. 31 (1959) 688

[57] A.G. Khachaturyan, Theory of Structural Transformations in Solids, New York, (1983) 198

[58] J.P. Simmonsa, Y. Wen, C. Shen, Y.Z. Wang, Mater. Sci. Eng. A. 365 (2004) 136

[59] T.P. Gabb, D.G. Backman, D.Y. Wei, D.P. Mourer, D. Furrer, A. Garg, D.L. Ellis, Superalloys 2000, Proceedings of the Ninth International Symposium on Superall. (2000) 405

[60] R. Radis, M. Schaffer, M. Albu, G. Kothleitner, P. Polt, E. Kozeschnik, Acta Mater. 57 (2009) 5739

[61] J. Svoboda, F.D. Fischer, P. Fratzl, E. Kozeschnik, Mater. Sci. Eng. A. (2004) 166

[62] E. Kozeschnik, J. Svoboda, P. Fratzl, F.D. Fischer, Mater. Sci. Eng. A. 385 (2004) 157

[63] E. Kozeschnik, J. Svoboda, F.D. Fischer, Calphad 28 (2005) 379

[64] K.G.F. Janssens, D. Raabe, E. Kozeschnik, M.A. Miodownik, B. Nestler, Computational materials engineering: an introduction to microstructure evolution. Oxford: Elsevier (2007)

[65] E. Kozeschnik, J. Svoboda, F.D. Fischer, Proceedings of the international conference solid–solid phase transformations in inorganic materials, PTM 2005, Phoenix (2005) 301

[66] A.J. Ardell, R.B. Nicholson, Acta Metall. 14 (1966) 1295

[67] V.A. Phillips, Acta Metall. 14 (1966) 1533

[68] S.A. Hill, B. Ralph, Acta Metall. 30 (1982) 2219

[69] J.W. Cahn, Acta Metall. 10 (1962) 179 and 907

[70] J.W. Cahn, Trans. Am. Inst. Min. Engrs. 242 (1968) 166

[71] H. Wendt, P. Haasen, Acta Metall. 31 (1983) 1649

[72] W.O. Gentry, M.E. Fine. Acta Metallurgica 20 (1972)181

[73] C.L. Corey, B.Z. Rosenblum, G.M. Greene, Acta Metall. 21 (1973) 837

[74] W.A. Soffa, D.E. Laughlin, Acta Metall. 37 (1989) 3019

[75] D.H.B. Israel, M.E. Fine, Acta Metall. 11 (1963) 1051

[76] K. Saito, R. Watanabe, Trans. of National Research Inst. for Met. 11 (1969) 153

[77] D.E. Laughlin, Acta Metall. 24 (1975) 53

[78] D.E. Laughlin, PhD Thesis, M.I.T Cambridge, MA 1973

[79] D.E. Laughlin, J.W. Cahn, Metall. Trans. 5 (1974) 492

[80] D.E. Laughlin, J.W. Cahn, Acta Metall. 23 (1975) 329

[81] A. Cerri, R. Schmelczer, P. Schwander, G. Kostorz, A.F. Wright, Mater. Res. Soc. Symp. Proc. 82 (1987) 169

[82] A. Cerri, B. Schonfeld, G. Kostorz, Phy. Rev. B. 42 (1990) 958

[83] R. Sinclair, J.A. Leake, B. Ralph, Phys. Stat. Sol. 26 (1974) 285

[84] H. Yoshida, M. Arita, A. Cerri, G. Kostorz, Acta Metall. 34 (1986) 1401

[85] G. Kostorz, Dynamics of Ordering Processes in Condensed Matt., Plenum Press, New York

[86] T. Ungar, M. Lambrigger, G. Kostorz, Mater. Sci. Eng. A. 138 (1991) 147

[87] R. Grune, P. Haasen, Journal De Phys. 47 (1986) C2-259

[89] D. Blavette, A. Bostel, Surface Science Lett. 177 (1986) L994

[90] C.B. Morrison, Y. Zhou, R.D. Noebe, D.N. Seidman, Phil. Mag. 90 (2010) 219

[91] A. Buchon, A. Bostel, D. Blavette, Colloque De Phys. 50 (1989) C8-401

[92] C. Schmuck, P. Caron, A. Hauet, D. Blavette, Phil. Mag. A. 76 (1997) 527

[93] J.V. Wood, P.F. Mills, A.R. Waugh, J.V. Bee, J. Mater. Sci. 15 (1980) 2709

[94] J. Wood, P.F. Mills, J.K. Bingham, J.V. Bee, Metall. Trans. A. 10 (1979) 575

[95] R.A. Ricks, A.J. porter, R.C. Ecob, Acta Metall. 31 (1983) 43

[96] M. Doi, T. Miyazaki, T. Wakatsuki., Mater. Sci. Eng. 67 (1984) 247

[97] A.G. Kachaturyan, S.V. Semenovskaya, J.W. Morris, Acta Metall. 36 (1988) 1563

[98] T. Miyazaki, M. Imamura, T. Kozaki, Mater. Sci. Eng. 54 (1982) 9

[99] A. Hazotte, T. Grosdidier, S. Denis, Scripta Mater. 34 (1996) 601

[100] Y. Tsukada, Y. Murata, T. Koyama, M. Morinaga, Defect and Diffusion Forum 297-301 (2010) 376

[101] V. Vaithyanathan, L.Q. Chen, Acta Mater. 50 (2002) 4061

[102] W.Z. Ostwald, Phys. Chem. 34 (1901) 495

[103] I.M. Lifshitz, V.V. Slyozov, J Phys. Chem. Sol. 19 (1961) 35

[104] C.Z. Wagner, Elektrochem. 65 (1961) 581

[105] A.J. Ardell, Acta Metall. 20 (1972) 61

[106] C.K.L. Davies, P. Nash, R.N. Stevens, Acta Metall. 28 (1980) 179

[107] A.D. Brailsford, P. Wynblatt, Acta Metall. 27 (1979) 489

[108] P.W. Voorhees, M.E. Glicksman, Acta Metall 32 (1984) 2001

[109] N. Akaiwa, P.W. Voorhees, Phs. Rev. E. 49 (1994) 3860

[110] J.A. Marqusee, J.J. Ross, Chem. Phys. 80 (1984) 536

[111] M. Tokuyama, K. Kawasaki, Physica A. 123 (1984) 386

[112] J. Zhao, J. Guo, J. Jia, Q. Li, Trans. NFsoc. 5 (1995) 67

[113] A. Maheshwari, A.J. Ardell, Acta Metall. 40 (1992) 2661

[114] D.M. Kim, A.J. Ardell, Scripta Mater. 43 (2000) 381

[115] D.M. Kim, A.J. Ardell, Acta Mater. 51 (2003) 4073

[116] D.M. Kim, A.J. Ardell, Metall. Mater. Trans. A. 35 (2004) 3063

[117] J.H Cho, A.J. Ardell, Acta Mater. 45 (1997) 1393

[118] J.H Cho, A.J. Ardell, Acta Mater. 46 (1998)5907

[119] A.J. Ardell, V. Ozolins, Nat. Mater. 4 (2005) 30

[120] D.K. Sudbrack, D. Isheim, R.D. Noebe, N.S. Jacobson, D.M. Seidman, Microsc. Microanal. 10 (2004) 355

[121] R. Srinivasan, R. Banerjee, J.Y. Hwang, G.B. Viswanathan, J. Tiley, D.M. Dimiduk, Phys. Rev. Lett. 102 (2009) 086101

[122] J. Tiley, G.B. Viswanathan, R. Srinivasan, R. Banerjee, D.M. Dimiduk, H.L. Fraser, Acta Mater. 57 (2009) 2538

CHAPTER 3

PROCESSING AND CHARACTERIZATION TOOLS

3.1 Alloy Preparation

This chapter includes the processing steps involved in fabrication of the materials, the thermal treatments involved and characterization of the materials by various techniques. The material used in our study is Rene88DT, a multicomponent nickel base superalloy that was fabricated at Wright- Patterson Air Force Research Lab. This chapter discusses the details of heat treatments and the characterization equipment used to analyze the microstructure of the material. This work has been brought to result by a collaboration of various tools and heat treatment equipment at different facilities at AFRL, Ohio State University and University of North Texas as discussed in later sections.

Rene88DT was produced as part of research work by Defense Advanced Research Projects Agency, Defense Sciences Office (Engine Systems Prognosis, Contract Nos. HR0011-04-C-0001 and HR00011-04-C-0002). This material was forged into a disc under the program to see the effect of microstructure on the mechanical properties of the alloy. The material for present study was taken by cutting a piece from the bore and rim section of the forged disc. Table 3.1 contains the bulk composition of Rene 88 DT that was measured.

Table 3.1. Bulk composition of Rene88DT.

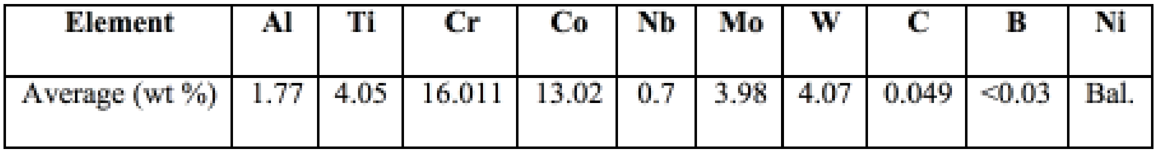

Element	Al	Ti	Cr	Co	Nb	Mo	W	C	B	Ni
Average (wt %)	1.77	4.05	16.011	13.02	0.7	3.98	4.07	0.049	<0.03	Bal.

Depending on the availability of the material, the cut piece was sectioned into needle shaped specimens for atom probe study and flat specimens for SEM, TEM and other characterization.

3.2 Thermal Treatments

The heat treatments of the samples obtained were performed at two Air Force Research labs. The material was solutionized at 1150^{o}C above the supersolvus temperature (1126^{o}C) for 30 min to dissolve all γ', from single γ phase and cooled at various cooling rates depending on the heat treatment schedule. For slow cooled (SC) and fast cooled (FC) treatment the material was solutionized in a vacuum furnace to prevent any oxidation of the material. Subsequently, the solutionized samples were cooled at 24^{o}Cmin^{-1} and 280^{o}Cmin^{-1} for SC and FC condition. Slow cooled samples were cut from these heat treated condition and then aged for 1, 10, and 15 hours at 760^{o}C in a vacuum furnace and air quenched. Another piece of material cut from the bore was solutionized and water quenched in a non-vacuum furnace to allow rapid quenching using water. To get the cooling rate information, holes were drilled in the sample and thermocouples were inserted. Post solutionizing, the samples were quenched at a rate > 300 ^{o}Cmin^{-1}. A cooling rate greater than 300^{o}Cmin^{-1} is expected from the experiment due to do the delay in heat transfer from specimen to data acquisition system. For even faster cooling rates, thin sections of the alloy (< 2mm) were solution treated in the single γ phase-field at 1150°C for 60 minutes in vacuum followed by a very rapid quench in ice-water that was kept in an inert argon atmosphere. The purpose of the very rapid quench was to arrest or capture the formation of the ordered γ' precipitates at the earliest stage. Following quenching, the samples were aged at 760^{o}C for 1, 5, 30 and 60 min.

3.3 Experimental Tools

3.3.1 Mechanical Cutting and Polishing

After the heat treatments, the samples were sectioned for scanning electron microscopy and transmission electron microscopy studies. Small sections of the material were cut using TechCut 4^{TM}, a rotatory low speed saw for metal cutting. A high concentration diamond metal bonded wafering blade (5” x 0.015” x ½ “) was used to cut the specimen with a cutting fluid to minimize friction heating of the specimen. The needle shaped specimens (1” x 1/12” x 1/12”) were coarse polished using 600 grit silicon carbide paper to obtain a needle with tip radius of approximately 100 micron. For metallographic analysis, the alloyed samples were first mounted using a hot molding compound PROBEMET (by Buehler®) in a Buehler Simplimet automatic mounting press. The mounts were then polished using silicon carbide abrasive paper by LECO Corpration®, varying from 400, 600, 800 and 1200 grit. After coarse polishing, the mounts were fine polished using alumina powder with particle size 1 micron, 0.3 micron, and 0.05 micron on a polishing cloth. The polished samples were cleaned using methanol, acetone and ultrasonicated to remove both organic and inorganic from the sample surface. These samples were then used for SEM, FIB, TEM and atom probe studies.

3.3.2 Chemical and Electrochemical Procedures

Prior to SEM analysis the mounted samples were polished and etched using 15ml HCl + 10ml Glycerol + 5ml HNO_3 for 15 seconds. This light etching substantially enhanced the contrast between the γ and γ' phases in the secondary electron imaging mode of the SEM. This solution etches the γ phase and therefore permits differentiation of γ' particles from the matrix. The time of etching needs to be controlled as this etchant can etch γ' if etched for long.

The samples in form of needles for atom probe investigations after mechanical polishing using abrasive paper were electrochemically sharpened to tip with < 70nm diameter. The samples were polished using ElectroPointer^{TM} by Simplex Scientific. The electro polishing of the samples was achieved in 2 steps. The tips were first coarse polished using 5% perchloric acid in acetic acid (bal) and 25V. For fine polishing 2% perchloric acid in butyl cellusolve was used with 15V. These tips were then cleaned with acetone and plasma cleaned before putting in the Local Electrode Atom Probe (LEAP) for analysis.

3.3.3 Scanning Electron Microscopy

Scanning electron microscope was used to study the coarse precipitates' size and morphology in the polished samples. This study was done using Nova NanoSEM 230^{TM} by FEI installed at CART (Center for Advanced Research and Technology) user facility in University of North Texas. It has high resolution field emission gun column with a beam landing energy 50V – 30kV. This system is fitted with In-lens SE detector (TLD-SE), In-lens BSE detector (TLD-BSE) Everhardt-Thornley SED, low vacuum SED (LVD), IR-CCD, TV-rate solid-state BSED, TV-rate low vacuum solid-state BSED (GAD) along with electron backscattered diffraction (EBSD) and energy dispersive x-ray spectroscopy (EDS) system.

3.3.4 Focused Ion Beam

Dual Beam SEM/FIB system at University of North Texas was used for sample preparation. This system is FEI Nova 200 NanoLab, a dual column; ultra high resolution filed emission scanning electron microscope and focused ion beam fitted with EDS system with spectrum imaging control. The ion column generates an accelerated gallium (Ga) ion beam using an electric field 5-10kV and focused onto a particular region that can be used for etching materials and platinum deposition using gas injection system (GIS) is available for nanoscale prototyping. The vertical high resolution SEM column is at 52^o with the ion column which permits in situ visualization of the selected region being milled by ion beam. This equipment in present study was used for two primary purposes.

(i) Sample preparation for TEM: The extreme water quenched (EWQ) samples for TEM were made using FIB system due to small size of specimen (to achieve faster quench rates). This technique helps to prepare TEM samples that are ~100nm thick and are typically 20 x 5micron in size. Therefore, this preparation method is suitable for site specific analysis or to analyze features that are few microns in size. Initially, the mounted and polished specimen was brought to eucentric height of 5mm (working distance) and tiled to 52^o such that the sample surface was perpendicular to ion column. A region (2micron x 25micron) was selected on the sample surface and platinum was deposited to protect the region of interest. A trench was milled using Ga ion beam on either side of the region using a stepped pattern. The sample was tilted back to 0^o and undercut. Nano manipulator omniprobe was inserted into the chamber and attached to the corner of the selected region and the region was cut from the sides and lifted out with the omniprobe. This rectangular micron sized sample was attached to a semi circular copper grip and thinned down to 500nm thickness from 2 micron using 30kV Ga ion beam and then at 5kV thinned down until the specimen becomes electron transparent. This sample on semi circular copper grid was then put in TEM holder and loaded into the TEM. The low kV milling (5kv) also removed the Ga implantation and amorphized material from the sample to be analyzed.

(ii) Sample preparation for Atom Probe: Apart from electropolishing, FIB technique can also be used to prepare samples for atom probe. The samples that were not in the form of needles were used to prepare FIB based atom probe samples. The process is similar to that of TEM sample preparation by FIB, however, instead of tilting to 52^o and cutting a trench, a wedge was cut by tilting the stage to 22^o. This wedge was then lifted out from the sample using omniprobe and attached on micro posts on a microtip array. This process allows user to make multiple samples with a single lift out. Then attached wedges were then sharpened to obtains tips with <100nm diameter. These tips were cleaned using 5kV ion beam to remove few nanometers of material implanted with Ga ion from the sharpened tips [1, 2]. The prepared tips were then plasma cleaned and put into the LEAP system.

3.3.5 Transmission electron microscopy

Transmission electron microscopy was done on two different TEMs, 200KV FEI Technai G^2 F20 S-Twin (S)TEM at University of North Texas and FEI Titan^{TM} 80-300. Technai is a 200 kV TEM with a high current Shotkey field emitter electron gun with a point to point resolution of 0.24nm and 0.14nm information limit at Ohio State University. The energy spread of the electron gun is 0.7eV or lesser at 200kV. The Technai microscope has a Super-Twin objective lens with 1.2mm Chromatic (C_c) and spherical aberration (C_s) coefficients. Sample holders were capable of going upto $\pm 40^o$ eucentric tilt. It also has a Fishione high sensitivity high angle annular dark field (HAADF) detector as an attachment for STEM imaging. The high resolution STEM imaging resolution for this microscope is 0.19nm. It is also equipped with a low system background EDS detector for microanalysis. The fully computer controlled specimen holder permitted usage of a variety of holders from single tilt, double tilt and tomography holders. The basic diffraction, dark field and bright field imaging, scanning transmission electron microscopy imaging (STEM), and EFTEM of samples were done using both the FEI Technai microscope and FEI Titan microscope [3].

Some of the more detailed high resolution TEM and STEM imaging were performed on FEI Titan^{TM} 80-300 microscope. Titan is fitted with a Cs corrector and a monochromator. The Cs correctors are of dual hexapole type and they over compensate the positive Cs of lens system and thereby limit the third order spherical aberration. The chromatic aberration is also reduced by the 300kV Wein filter monochromator resulting in a beam energy spread less than 0.1eV. In addition to this, Titan is also made with a high speed digital search and view camera replacing the conventional fluorescent viewing screen. The microscope has a 0.2nm point resolution and information limit of 0.07nm. The HRSTEM resolution is 0.13nm. HRSTEM studies were done using the axis Fischione® HAADF STEM detector [3]. In HAADF-STEM an incident converged beam is used to image the specimen with sub angstrom probe diameter. The electrons that are incoherently scattered are collected at high angle that eliminates the contrast due to diffraction (~3^{o}). The intensity of the collected electrons, which is proportional to Z^2 where Z represents atomic mass, directly gives a contrast to image. The contrast mechanism is based on Rutherford scattering. Scattering due to small atoms at high angles result in less coherent transmitted beam and hence less intensity (dark) as compared to heavier atoms, which scatter at comparatively lower angle, hence appear brighter.

Conventional TEM samples were made from 3mm diameter discs punched out of thin foils of the alloy prepared by mechanical polishing. The mechanical polishing of the electric discharge machined (EDM) thin slices of alloy samples were performed using 240, 400, 600, 800 and 1200 grit silicon carbide papers to attain a final thickness of 50-70 micron before punching. The punched 3mm disks of the alloy samples were subjected to dimple grinding on Gatan

Dimple Grider^{TM} using 1μm diamond paste to attain a dimpled region thickness of 20μm. Subsequently these dimpled samples were subjected to argon (Ar) ion milling in either Gatan Precision Ion polisher (PIPS) or Fishione 1010. Ion milling in Gatan PIPS^{TM} system was done initially using two 5kV Ar ion guns oriented at an angle of 4^{o} from top and bottom surface of the sample followed by a final milling at 2kV at 0.5 degrees from top and bottom of the sample. The milling in Fishione 1010 ion milling unit was performed by using two 5-2kV Ar ion beams at angles from 10^{o} to 6^{o}. For TEM samples used to perform aberration corrected HRSTEM and HRTEM imaging, an additional low energy milling of the samples were performed in Fishione 1040 nanomill^{TM}. In that process a 50-2000V Ar ion beam is selectively rastered on the region of interest facilitating a removal of the amorphous damage that can be caused during high kV milling stages of prior sample preparation steps.

3.3.6 Synchrotron based X-ray Diffraction

The Advanced Photon Source (APS) is a national user facility funded by Department of Energy (DOE). High brilliance x-rays generated by APS were used for performing the in-situ high energy x-ray diffraction experiments for capturing γ' nucleation events during continuous cooling. Such high energy x-rays are generated from the electrons that are emitted from a heated cathode at 1100^{o}C. The electrons are subsequently accelerated to 450MeV, travelling at 99.999% of speed of light in a linear accelerator before injecting them into a booster synchrotron. In booster synchrotron the electrons are further accelerated by a series of electromagnets to 7GeV. This enhances the speed of electrons and they travel at a speed greater than 99.999999% of the speed of light. Subsequently these electrons are injected into a 1.105km circumference storage ring where these electron beams are bent and focused to a narrow beam travelling in circular path using electromagnets. The storage ring has several straight and curved regions. A series of powerful alternating pole magnets that are inserted in the straight section of the storage ring undulates the electron beams. This leads to the emission of high brilliance x-rays along a tangential direction of the storage ring. Such devices are known as insertion devices. Such x-ray beams emitted are further collimated and directed to experimental halls in the beam line [5]. The sample analyzed in this work was kept in the beam path of 11IDC beamline in an atmosphere controlled TS1500 Linkam furnace. A schematic diagram of the experimental set up is given in Fig 3.1. The 0.5mm by 0.5mm sized 115keV x-ray beam passes through a background free window before interacting with sample under study. The diffraction patterns were collected on a Perkin Elmer 2D detector. The time-temperature cycling of TS1500 Linkam furnace and data acquisition was remotely controlled through scripts. The temperature of the furnace was recorded in a time-temperature file and also was remotely monitored through a video camera focused on the temperature controller display. 2D circular ring diffraction patterns from the sample were recorded with one-minute intervals. For better statistics multiple images were integrated during each exposure. After the completion of the heat treatment, the integrated images were processed using Fit2D, a 2D data analysis program. Batch processing was used for processing all images at once. Subtraction of spurious peaks from background was done using a standard mask file. Subsequently the data was integrated to generate intensity versus theta plot. The sample to detector distance was kept at 1788.165mm. The wavelength of the x-ray beam was given as 0.107980A^o corresponding to beam energy of 115keV. The X and Y pixel of the direct beam were given as 1026.583 and 997.0520 respectively. The radial integrated data was sent to output as a bitmap image and a chi file. The theta versus intensity data from chi file was copied and pasted in a Microsoft excel file for further detailed analysis. Subsequently the time evolution of

[100] γ' and [111] $\gamma' + \gamma$ peaks were studies from the selected data files after specific intervals from the beginning of the ageing experiment to end of ageing.

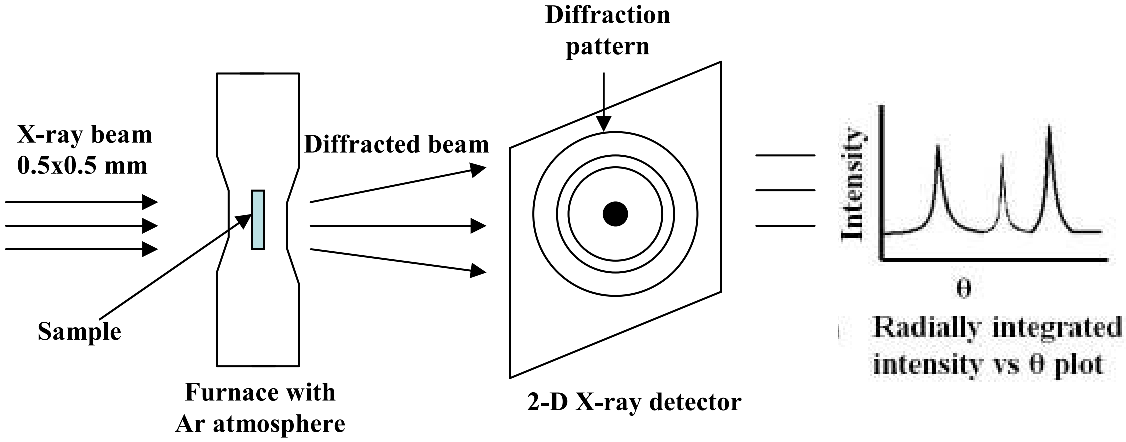

Figure 3.1. Experimental set up of in-situ high energy x-ray diffraction at advanced photon source.

3.3.7 Atom Probe Tomography

A new generation, Local Electrode Atom Probe (LEAP) 3000X HR three-dimensional atom probe (3DAP) from Imago Scientific Instruments (Now CAMECA) was used for all the analysis presented in the current work. This 3DAP system is equipped with voltage and laser pulsed mode of evaporation. High mass to charge spectrum resolution was attained due to the advanced reflectron system in which the flight path of the atoms is increased leading to increased differentiation between isotopes of atoms.

During atom probe analysis, individual atoms from the tip of a sharp needle shaped specimen with tip diameter of about 50-100nm are field evaporated by applying either a pulsing voltage or a pulsed laser beam in addition to an applied stead state standing voltage across an electrode and the sample. This pulsating voltage was kept at 20% of the steady voltage. During laser mode 0.2nJ of laser energy was used. These field-evaporated ions are accelerated towards a position sensitive single atom detector. The single atom position sensitive detector is made of a microchannel plate with cross delay line detector. The time of flight of individual ions are recorded from the time difference of the applied pulse to atom detection at the position sensitive detector [6]. A schematic of the experimental set up for atom probe tomography is given in Fig. 3.2.

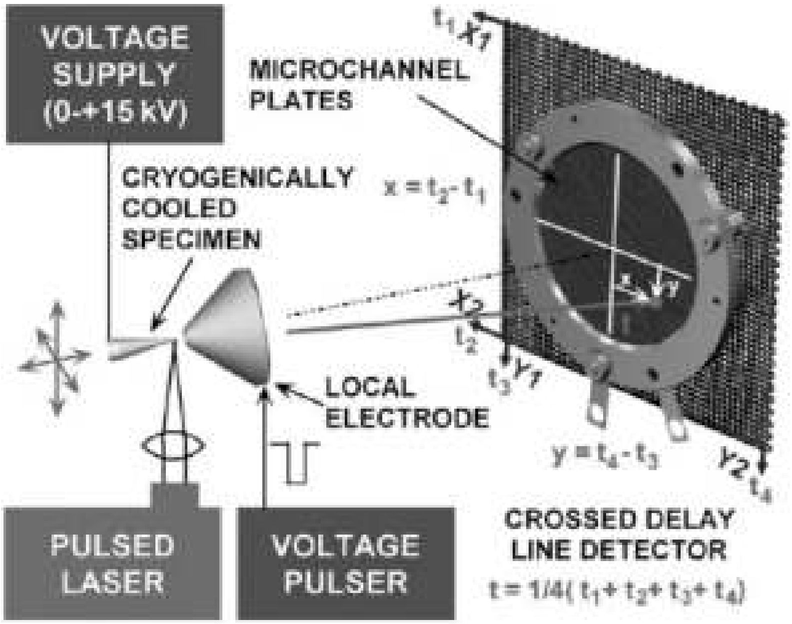

Figure 3.2. Schematic diagram of a three dimensional atom probe [6].

Field evaporation of the atoms is done by applying about 10-40Vnm^{-1}, which causes ionization of surface atoms. The initial stage of field evaporation is a thermally activated ion escape over an activation barrier followed by a second stage of post field ionization. From the first stage to second stage the ionic charge can go from 1-3e to n*e, where e is a single electron charge and n is an integer. The field emission rate constant (k) can be given by the following equation [6].

$$K = A \exp [-Q(F)/k_b t]$$

Where A is a constant, Q(F) is the activation energy for field evaporation which is a function of applied field (F), T is temperature and k_b is the Boltzmann constant. The field F at which the activation energy Q(F) is zero is known as the zero Q evaporation field. The practical values of Q(F) is usually slightly greater than zero. The pulsed voltage or laser beam applied to the specimen provides the initial "jump start" required by providing the excess activation energy for start of field evaporation [6]. The evaporation field F at the tip of a sample of radius R on application of voltage V is given by

$$F = V / K * r_t$$

K is a numerical constant with a value between 2 to 5. Since F is inversely proportional to r, sharper needles cause higher field amplification [10]. This is why, individual atom probe sample tips are made to be less than 100nm in diameter to attain the evaporation fields required even at lower applied voltages (typically 500V to 11000V). Mass to charge ratio (m/n) of ions can be derived by equating potential energy of ion just before field evaporation (neV) to kinetic energy just after field evaporation ($1/2*mv^2$) to obtain the following relationship [7].

$$m/n = Const * V * (t^2/d^2)$$

The constant has been estimated as 0.1929796 for V in kVs, time (t) in nano-seconds, d in mm and m in atomic mass unit (amu). The time of flight is estimated by the field free drift tube situated between the sample and position sensitive detector also known as "time of flight spectrometer". Using the cross delay line detector the x and y coordinates of the ion impact are calculated. The real atom coordinates on the sample is determined by

$$X = x / M \; ; \; Y = y / M$$

Where M is magnification given by ($d/\beta r_t$) where d is specimen to detector distance, β is the image compression factor, and r_t is the tip radius [7]. The image compression factor is a projection parameter with a default value of 1.65 used in the software; however, it can be changed. A schematic diagram of the projection geometry is shown in Fig 3.3 [8].

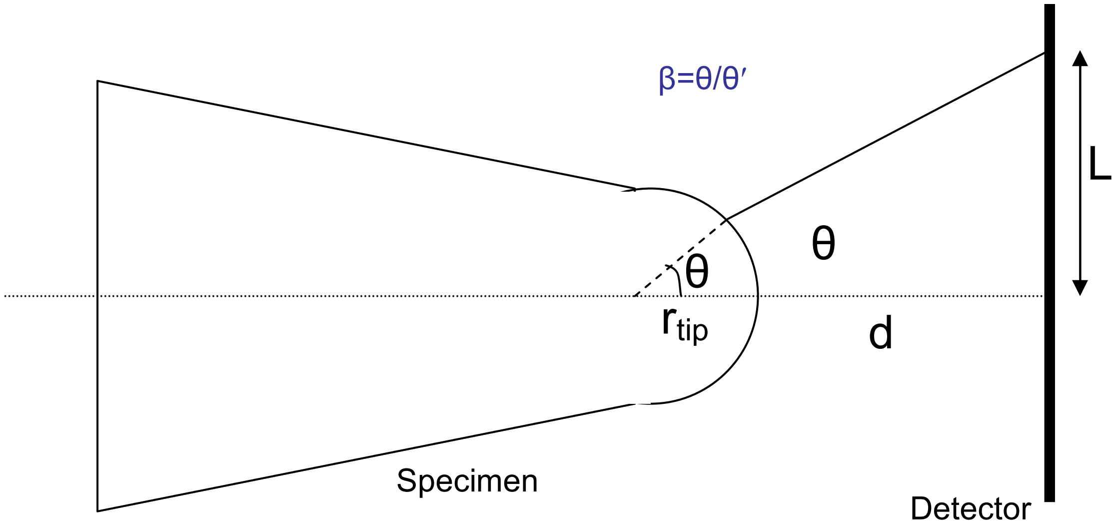

Figure 3.3. The projection geometry of an atom probe sample.

A straight flight path three-dimensional atom probe typically has 50-60% detection efficiency due to loss of ions which strike the walls of microchannel. The detection efficiency further reduces to 37% in a reflectron based high resolution three dimensional atom probe due to additional loss of ions hitting the mesh infront of the reflectron lenses, on entry and exit points [7].

The straight flight path 3 dimensional atom probe (3DAP) systems have an energy differential to the applied pulsing voltage. This causes a slight variation in the time of flight for elements because of a spread in the evaporation time of ions within a single pulse. This aberration leads to a reduction of mass to charge spectrum resolution. Hence an energy compensating electromagnetic lens assembly named as a reflectron lens is introduced to improve the mass to charge spectrum resolution [6-8]. The reflectron lens consists of a series of annular ring of electrodes with a reflecting plate at the end that causes the deceleration and reflection of ions from the sample towards the single atom detector. The maximum peak resolution is achieved by maintaining an optimized ratio of the applied voltage (V) and reflectron voltage (V_r) along with a ratio of flight path outside reflectron (d_f) to be four times of the flight path inside reflectron lens (d_r). This energy compensating reflectron lens makes the time of flight of ions independent of slight variations in energy of pulsing voltage resulting in a higher resolution in mass to charge spectrum [6-8].

3.4 References

[1] K. Thompson, D. Lawrence, D.J. Larson, J.D. Olson, T.F. Kelly, B. Gorman, Ultramicro. 107 (2007) 131

[2] J. Mayer, L. A. Giannuzzi, T. Kamino, J. Michael, MRS Bull. 32 (2007) 400

[3] FEI Technai G2 F20 series Product data sheet

[4] FEI TitanTM Product Brochure

[5] http://www.aps.anl.gov/About/APS_Overview/

[6] M.K. Miller, R.G. Forbes, Mater. Char. 60 (2009) 461

[7] M.K. Miller, Atom probe tomography, Springer publications, New York

[8] A.E. Marquis, J.M. Hyde, Mater. Sci. Eng. R. 69 (2010) 37

CHAPTER 4

INFLUENCE OF COOLING RATE ON THE MICROSTRUCTURAL EVOLUTION IN RENE88DT

4.1 Introduction

As discussed in the literature review, the cooling rate has a significant effect on the microstructural variation in nickel base superalloys. This variation in microstructure also has a significant effect on the mechanical properties of the material and therefore the study of the effects governing these changes becomes very important at the commercial as well as fundamental level. In the past few years, atom probe has been an important tool in the characterization of nickel base superalloys at the atomic scale [1-3]. The compositional changes between the γ and γ' phases have been investigated using integrated concentration profiles also known as ladder diagrams. Atom probe field ion microscopy (APFIM) has been conventionally used to establish these diagrams [4] However, with the incorporation of local electrode atom probe with large field of view detector for faster data acquisition, no only the time for data generation has reduced but also it has yielded more quantitative information on wide variety of materials at nanoscale [5]. Thus, atom probe has proved to be an important tool in the characterization of atomic scale microstructural and compositional changes; however, at a larger scale, TEM is still widely used for microstructural characterization. Therefore, atom probe when coupled with TEM can provide important information regarding the structure, morphology and compositional variations in the γ' along with the matrix. Furthermore, energy filtered transmission electron microscopy (EFTEM) techniques have been used quite successfully in order to distinguish these precipitates from the matrix, based on the partitioning behavior of different elements [6]. Hence, in the present study these techniques have been used to understand the effect of cooling rate on the microstructural evolution in Rene88 DT. Present chapter focuses on these aspects in the Rene88DT alloy, subjected to a super-solvus treatment in the single γ phase field, followed by cooling to room temperature employing three different cooling rates.

4.2 Experimental Procedure

Small samples of Rene88DT were solutionized above the γ-γ′ solvus temperature of 1150°C for 30 min (γ′ solvus for this alloy is 1124ºC [7]). Following the supersolvus heat treatment the material was cooled at three different rates of >300ºCmin^{-1}, 280ºCmin^{-1} and 24°Cmin^{-1}, corresponding to the water quenched, fast cooled and slow cooled conditions respectively. WQ0, FC0 and SC0 terms will be used for these heat treatment conditions from now on for convenience, where first two alphabets refer to the corresponding cooling rate. 0 is used as there is no post annealing done after cooling to room temperature. Transmission electron microscopy (TEM) samples were prepared using conventional electropolishing techniques followed by argon ion milling using a Fishione Model 1010 system. Images were obtained using the Cr M-edge (at 42 eV) in the energy-filtered TEM (EFTEM) mode on a FEI Tecnai F20 microscope operating at 200 kV, as described elsewhere [6]. Sharp needle-like specimens (with a tip radius of 100nm) for 3DAP tomography studies in the LEAP microscope were prepared using standard electropolishing techniques [8]. The 3DAP experiments were carried out using a LEAP 3000 local electrode atom probe (LEAP™) system from Imago Scientific Instruments Inc. in the electric-field evaporation mode at a temperature of 60K, with the evaporation rate varying from 0.5% to 1.0% and a pulsing voltage at 20% of the steady-state applied voltage. Data analysis was performed using the IVAS 3.0 software from Imago Scientific Instruments Inc.

4.3 Variation in Microstructure as a Function of Cooling Rate

The results of the experimental analysis are show below and also been discussed.

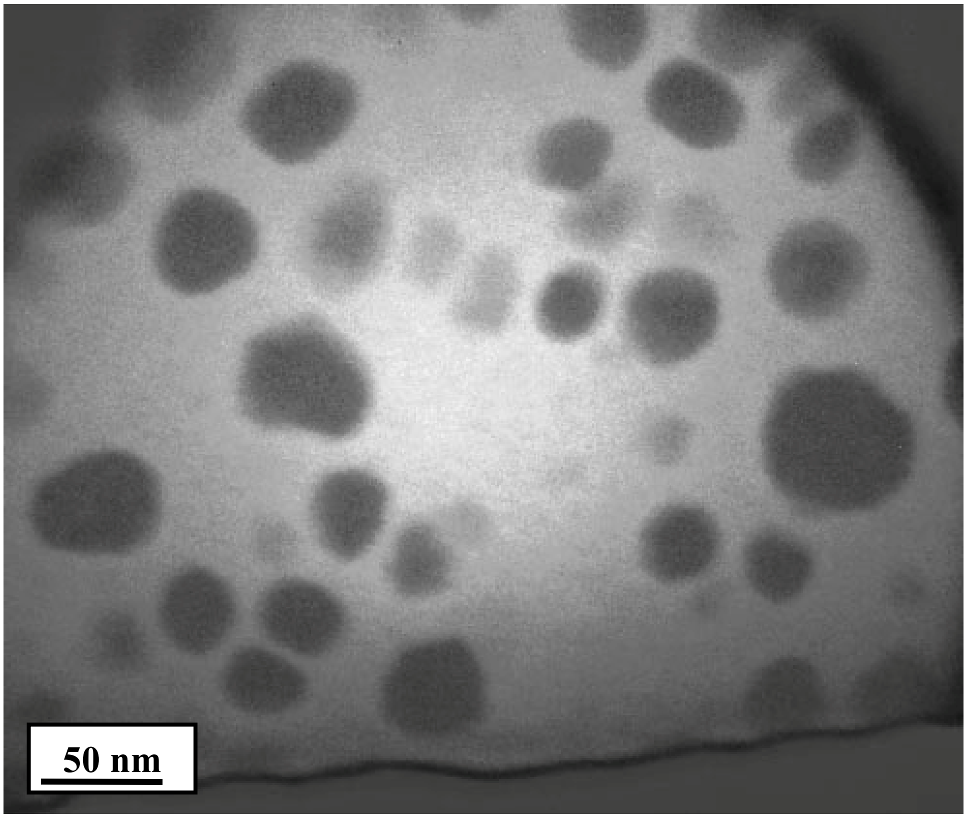

Figure 4.1. Energy-filtered transmission electron microscopy (EFTEM) images constructed using Cr M-edge in the EELS spectrum from solutionized and water-quenched WQ0 sample. The γ′ precipitates, which are Cr depleted, exhibit the darker grey contrast in these images.

An EFTEM image of water quenched WQ0 TEM sample recorded using the Cr M-edge (42 eV) is shown in Fig. 4.1. The darker regions correspond to Cr depleted γ′ precipitates while the brighter regions correspond to the γ matrix enriched in Cr [3]. The micrograph shows precipitates γ′ distributed in the γ matrix and this micrograph can be considered as representative microstructure of bulk material. The microstructure as shown in Fig. 4.1 exhibits a monomodal size distribution of γ′ precipitates with particle diameters ranging from 10 - 40nm for this fastest cooled condition. It is well known that nucleation rate increases exponentially with the undercooling ΔT required for precipitation of new phase. As seen in the TEM micrograph, such a high density of γ′ precipitates observed in this sample is indicative of the fact that they formed at very high under-coolings where the density of nucleation sites is expected to be high. Along with the variation in size of the precipitates, there exists a contrast between γ′ particles as well. This variation in contrast between different precipitates (smaller appearing lighter and larger appear darker) is due to the averaging effect of the 2D projected TEM image of γ′ precipitates embedded in a γ matrix. The overlapping of γ phase with γ′ particles for small sizes reduces the contrast of those particles and hence appears lighter. There also seems to be a variation in shape between various γ′ particles. A careful observation of the microstructure shows that some of the larger particles have developed facets. Therefore from Fig. 4.1 it can be qualitatively deduced that while the smaller precipitates exhibit a more spheroidal morphology, the larger precipitates tend to have partially faceted and planar interfaces as they grow in size. This is due to the fact that during growth of γ′ phase, the particles tend to grow along the elastically soft direction of the γ phase which is <001> and develop cuboidal structure. However, since all the precipitates have not developed facets and formed cuboidal morphology, it suggests that these precipitates are still in the growth regime and restricted in their further evolution due to fast cooling rates achieved and limited diffusion. From the micrograph, where the sizes of γ′ appear to be in the similar range it can be concluded that all the precipitates formed during a single nucleation event.

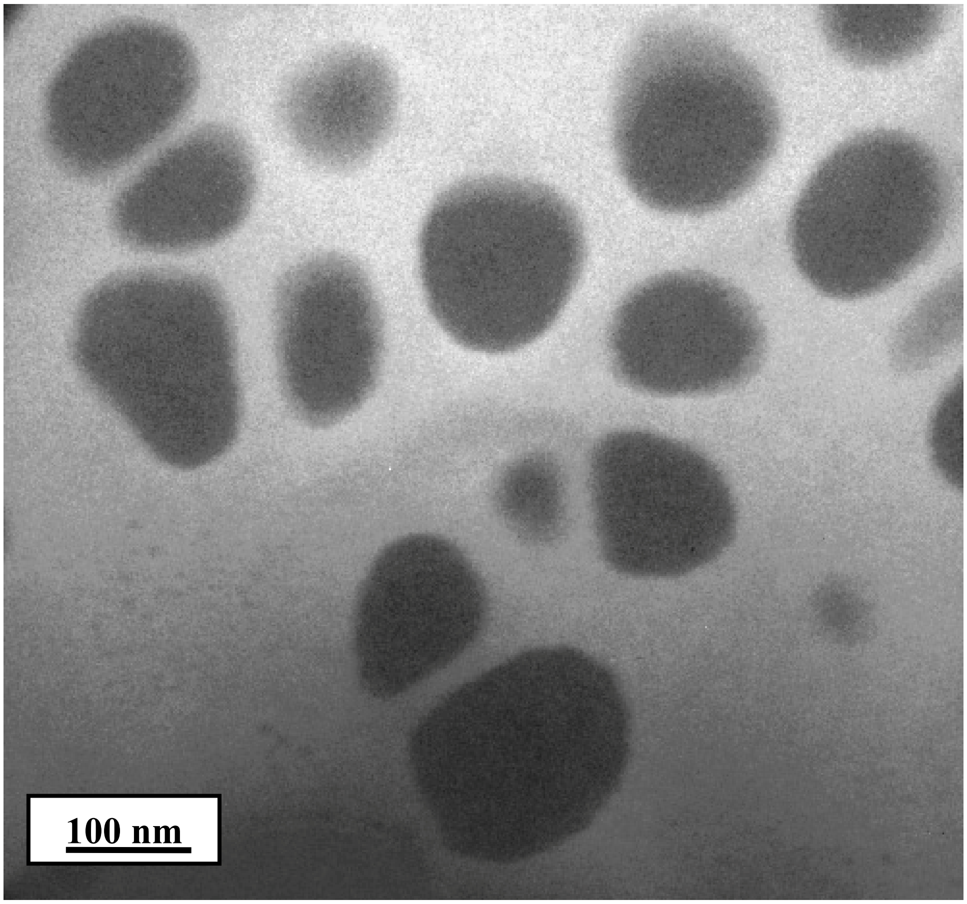

Figure 4.2. Energy-filtered transmission electron microscopy (EFTEM) images constructed using Cr M-edge in the EELS spectrum from solutionized and fast cooled FC0 sample. The γ′ precipitates, which are Cr depleted, exhibit the darker grey contrast in these images.

The situation is different when the alloy is cooled at comparatively slower cooling rate (FC0) as compared to water quenched. In FC0, microstructure developed is significantly different where multiple bursts of nucleation give rise to bimodal size distribution of γ′ precipitates. This is evident from the low magnification EFTEM image in Fig. 3.2 where the larger primary γ′ precipitates appear to be more cuboidal whereas smaller secondary γ′ precipitates are barely visible. The density of primary γ′ precipitates also seems to be comparatively lower than WQ0 suggesting these precipitates were formed at lower undercoolings as compared to ones in WQ0. Thus it can be claimed from this observation that the γ′ precipitation by nucleation burst in FC0 condition occurs at a much higher temperature as compared to WQ0. In addition do that in FC0 condition due to slower cooling rate, the primary γ′ precipitates experience higher growth and coarsening rates as a result of faster diffusion of elements at lower undercooling (higher temperature). Consequently, as shown in Fig. 4.2, these precipitates grow larger in size (~100nm) with relatively faceted interfaces for many precipitates. In addition to higher diffusion rates experienced in the sample, due to slower cooling rate in FC0 case compared to WQ0, the γ′ precipitates get more time for growth during cooling and which adds to increase in size of these precipitates also resulting in more faceted structure. In the EFTEM micrograph, away from the larger precipitates a higher density of much smaller precipitates can be observed.

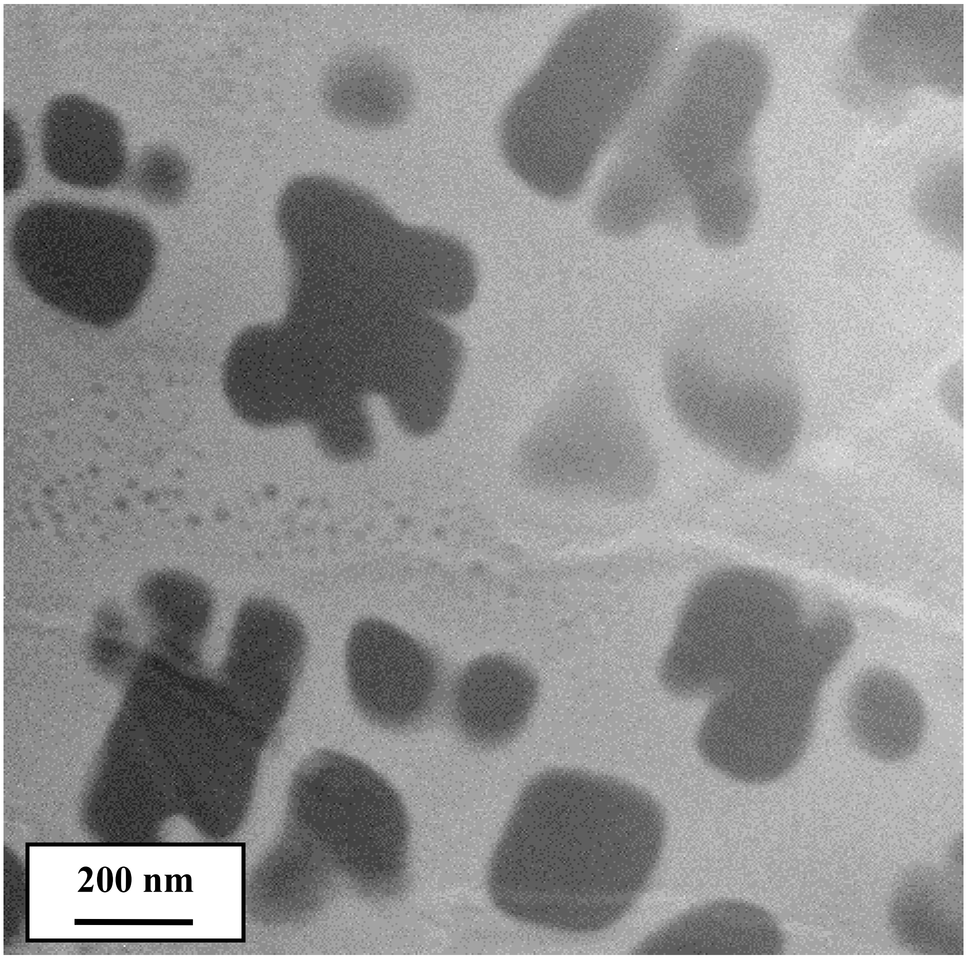

Figure 4.3. Energy-filtered transmission electron microscopy (EFTEM) images constructed using Cr M-edge in the EELS spectrum from solutionized and slow cooled SC0 sample. The γ′ precipitates, which are Cr depleted, exhibit the darker grey contrast in these images.

When the sample is cooled at even slower cooling rate ($24^{o}Cmin^{-1}$) or SC0 the distribution of γ′ precipitates with two distinct size ranges is much more evident. These precipitates appear to have a bimodal/multimodal distribution in the EFTEM micrograph as seen in Fig. 4.3. Following the same argument, it appears that growth and coarsening of γ′ precipitates occur even faster at lower undercooling levels, giving rise to much larger sized precipitates (~200nm). The larger precipitates have non-spherical morphologies (from cuboidal to irregular), largely with faceted interfaces. The effect of increase in strain energy with the increase in precipitate size results in change in morphology of γ′ precipitates [9-11]. Therefore, in SC0 condition, due to higher growth rates, the precipitates tend to attain non spherical morphology as shown in Fig. 4.3. In addition to that the coarsening of the precipitates either by the Oswald's ripening process or by coagulation from a random distribution of particles varies in different directions, resulting in an irregular morphology of precipitates as seen in the EFTEM image. However, smaller secondary γ' precipitates being substantially more in numbers appear to nucleate at a larger undecooling. Also they retain a nearly spherical morphology due to diffusion-limited growth of precipitates at low temperatures. Even though the larger precipitates appear to have grown and coarsened significantly in comparison to FC0 and WQ0, the matrix doesn't appear to be homogeneous with the presence of depletion free zones around the large precipitates. It can be deduced that due to continuous cooling, the matrix doesn't have enough time to reach equilibrium. The lower diffusivity at larger undercoolings is also responsible for the formation of "γ'-free depletion zones" around larger primary γ' precipitates (Fig. 4.3) formed due to the lack of long-range equilibration of the γ matrix composition away from a growing primary γ' precipitate during continuous cooling. As the name suggests, "depletion zones" are characterized by the absence of secondary γ' precipitates. As will be discussed later, these smaller particles, precipitated due to the second burst of nucleation, typically nucleate in large numbers in regions away from the depletion zone.

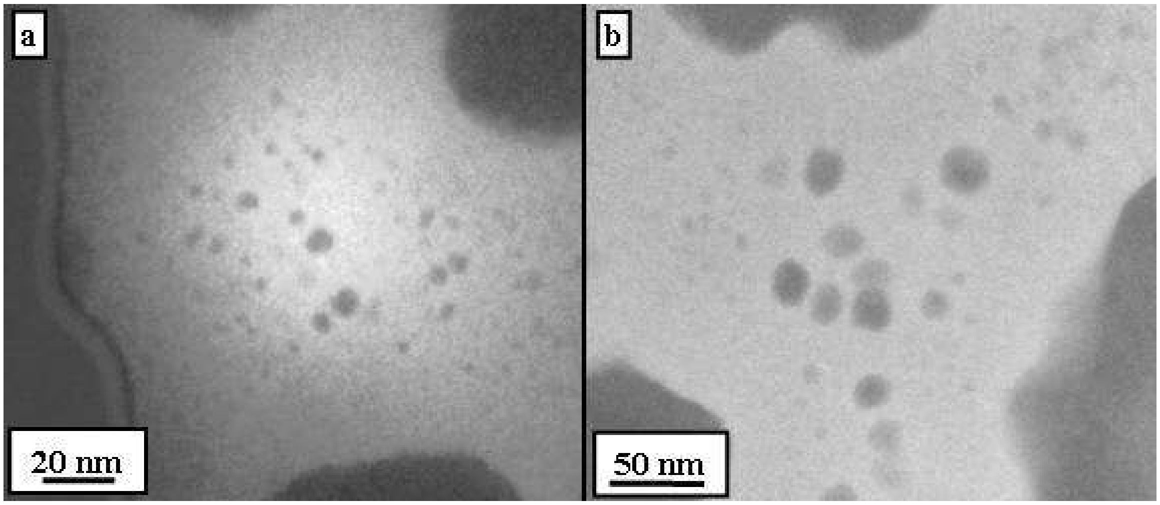

Figure 4.4. Energy-filtered transmission electron microscopy (EFTEM) images constructed using Cr M-edge in the EELS spectrum from solutionized and (a) fast cooled FC0 sample and (b) slow cooled SC0 sample, showing. The γ′ precipitates, which are Cr depleted, exhibit the darker grey contrast in these images.

Secondary γ′ precipitates possibly caused due to a second burst of nucleation event are more clearly visible in the high magnification EFTEM images from the FC0 and SC0 samples (Figs. 4.4(a) and (b) respectively). It is evident from the micrograph that the secondary γ′ population in SC0 is comparatively larger than that in FC0. Quantitative analysis of the secondary γ′ precipitates shows that average precipitate sizes are substantially smaller (<10nm) in the FC0 sample as compared with the SC0 sample (~25nm). Few rational arguments for this variation in size can be proposed: (i) In case of the slow cooled sample (SC0), the secondary γ′ precipitates experience longer time periods for growth due to the slower cooling rate as compared with the FC0 sample. (ii) The cooling rate can dictate the temperature at which secondary γ′ precipitates form. From previous experimental and computation studies it might be argued that the γ′ precipitates in FC0 condition may have nucleated at a lower temperature as compared to those in SC0 condition [9, 11, 13]. This suggests that the growth kinetics for secondary γ′ precipitates is slower in FC0 as compared to SC0 and thus remain smaller. This would also mean that there should be a compositional variation between secondary γ' population of FC0 and SC0. However, it is very difficult to conclusively state this mainly due to the complexity and interplay of different thermodynamic and kinetic phenomenon concurrently occurring in the system. (i) Continuous cooling is a non equilibrium cooling process since the system doesn't get infinite time to reach equilibrium at every temperature that dynamically deals with coarsening of primary γ' precipitates (ii) The diffusion fields of neighboring γ' precipitates start interacting with each other as they grow inside the matrix. (iii) Variation in super-saturation of matrix away from the γ' depleted regions, which provide the driving force for further nucleation, along with the partitioning tendencies of different elements in a multi-component alloy system. Also, one important thing to note is that the growth of these precipitates would also depend on the change in composition of the matrix during cooling which may be different in SC0 and FC0, as change in composition will change the chemical potential of elements between γ' and γ' phase. The change in composition changes the diffusivity of elements. A more elaborate discussion on this would be taken up later.

In addition to the difference in size of the primary γ' in FC0 and SC0 samples, there is also a variation in the thickness of the "depletion zone" around them. Figs. 4.4(a) and (b) clearly show that the depletion zone is larger in case of the SC0 (~50nm) sample as compared to the FC0 (~25nm) sample. The fact that system gets more time to grow during slow cooling, allows more partitioning of elements between γ' precipitates and the matrix resulting in wider depletion zone.

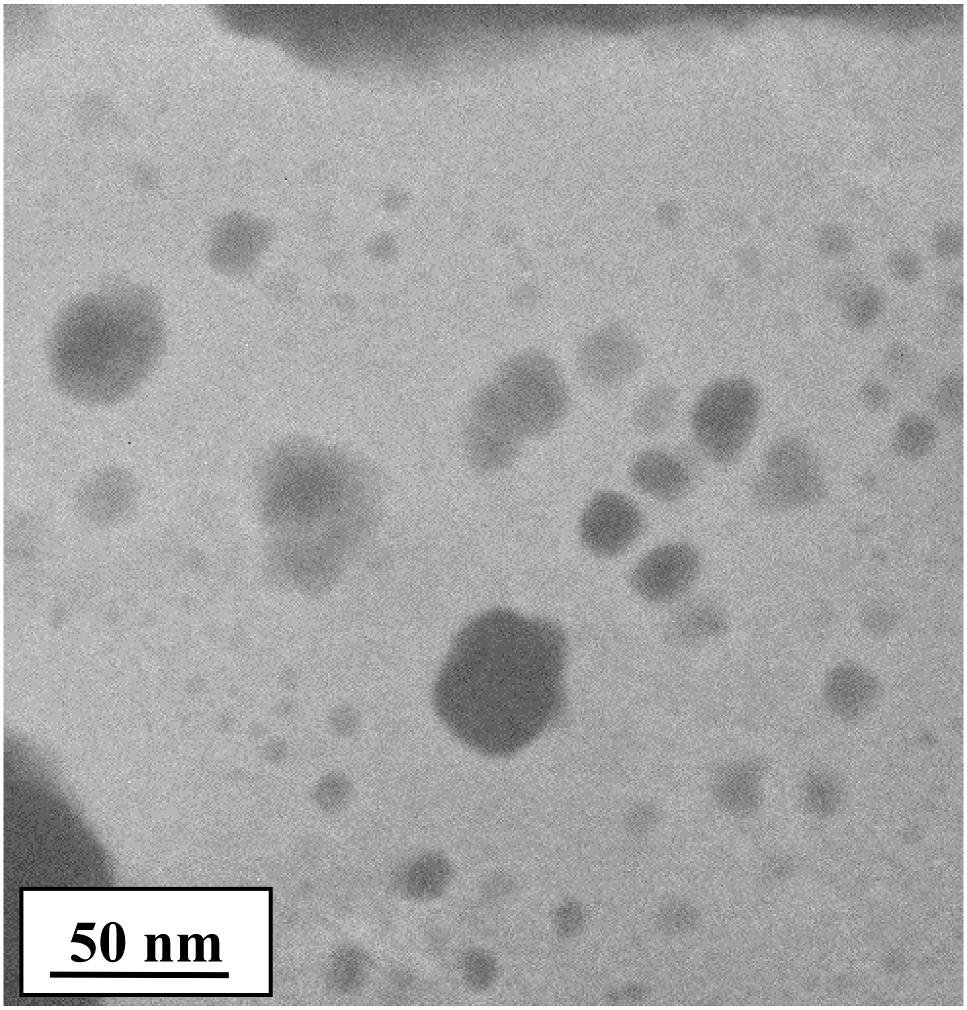

Figure 4.5. Energy-filtered transmission electron microscopy (EFTEM) images constructed using Cr M-edge in the EELS spectrum from solutionized and slow cooled SC0 sample, showing secondary and tertiary γ′ precipitates. The γ′ precipitates, which are Cr depleted, exhibit the darker grey contrast in these images.

Fig. 4.5 shows a different region of the sample that was slow cooled at 24ºCmin^{-1} (SC0). In the figure, apart from the secondary γ′ precipitates, a higher density of even smaller precipitates can be seen around them. This suggests that a third burst of γ′ precipitation might have taken place at lower temperatures (higher undercooling) as compared with the secondary nucleation burst. Some of the secondary γ′ precipitates seem to have developed faceted interfaces with the matrix suggesting that even the secondary γ′ precipitates get significant time for growth;

however, the smaller tertiary γ' population still maintains spherical morphology. Recent simulations, based on classical nucleation and growth theory, have predicted the formation of such trimodal microstructures [12].

The primary γ' population was quantified for the nucleation density using EFTEM images of the two heat treated conditions: FC0 and WQ0 and SEM images of SC0. If "N" is the number of precipitates and A is the area in μ^2 in which the precipitates are dispersed, then nucleation density N′ can be defined as $N' = N/A$ particles/ μm^2. Average interparticle spacing can then be defined as $\lambda = 1/\sqrt{(N')} - \langle N \rangle$ where $\langle N \rangle$ is the average size of particle in μm. Results of N′ and λ are shown in Table 4.1 below

Table 4.1. Variation in number density and inter-particle distance with cooling rate.

Cooling Condition	**WQ0**	**FC0**	**SC0**
Precipitate Density N′ (number/ μm^2)	759	46	8
λ (μm)	0.01	0.05	0.15

The results clearly indicate that the nucleation density increases with increase in cooling rate and the interparticle spacing decreases. This result also suggests that the time of nucleation event changes with cooling rate; with higher cooling rate more undercooling is required to precipitate γ'.

4.4 Compositional Analysis as a Function of Different Cooling Rates

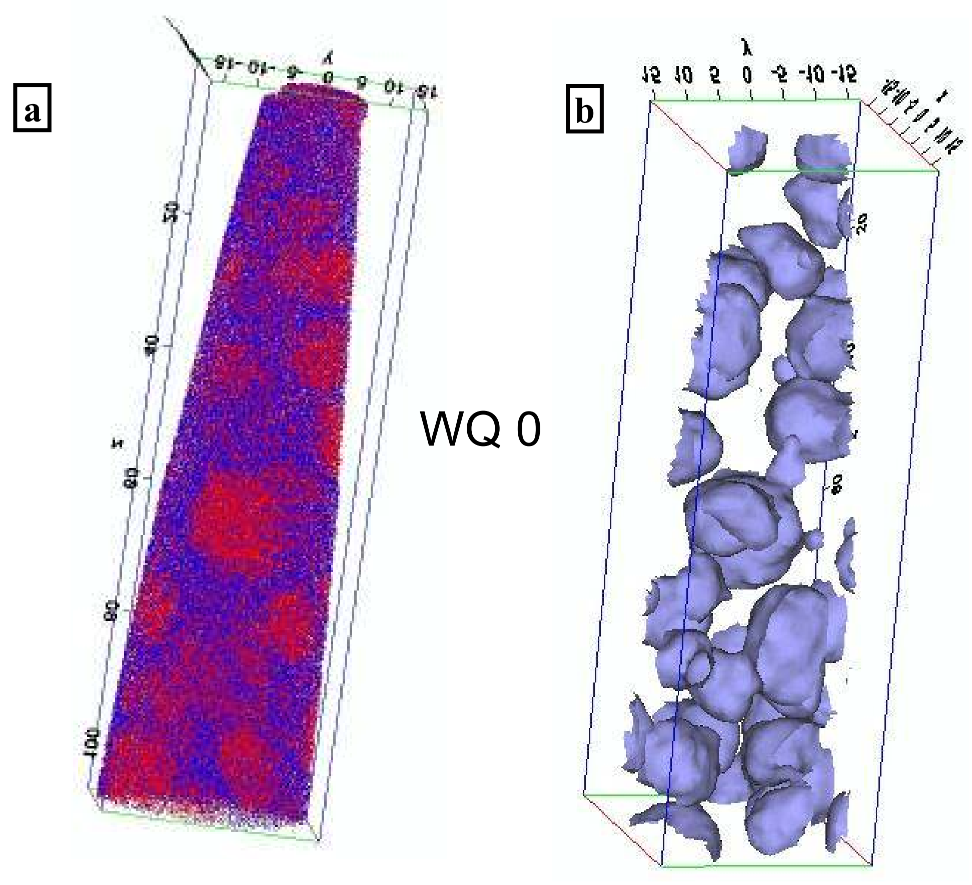

Figure 4.6. (a) 3DAP reconstruction of Co (blue) and Al (red) atoms in WQ0 atom probe sample. The γ′ precipitates are the Al-rich red regions with Co-rich blue matrix. (b) Different depiction of the same WQ0 3-D reconstruction showing Cr = 14at% isosurfaces.

A 3-dimensional atom probe (3DAP) reconstruction of water quenched sample is shown in Fig. 4.6. Fig 3.6(a) shows reconstruction of field evaporated atoms (only Al and Cr shown) that were collected from the water quenched sample (WQ0). Only two ions were chosen for pictorial representation because it gives better visualization. The 3D atomic rendition can be clearly seen with compositionally phase separating regions; regions rich in Al ions (red) demarcate the γ′ precipitates while the remaining γ matrix is Cr rich (blue). The reconstruction clearly suggests that the Al-rich γ′ precipitates (~10-15nm) fall within the same size-scale as those measured from EFTEM. These precipitates are more clearly delineated in Cr = 14at% iso-concentration or isosurfaces plotted in Fig. 4.6(b). Here the 3D contour plot demarcated the regions that contained less than 14at%Cr, thus showing only the γ′ precipitates. The value of 14at%Cr was chosen because it lies halfway between the equilibrium Cr content in γ and γ′ regions, determined via a proximity histogram analysis of the γ/γ′ interface [8, 14]. The isosurface analysis shows a high density of precipitates in close agreement with the EFTEM analysis Fig. 4.6(a). Presence of some interconnected regions due to overlapping diffusion fields can also be seen in the reconstruction. Such "necked" regions have been discussed in detail in previous papers [6, 8]. It is however difficult to quantitatively compare the density of precipitates in atom probe reconstruction with EFTEM as the sampled volume and number of precipitates are significantly different in both the techniques. Due to the sampled volume limitation in atom probe, a statistical analysis of precipitates of the order of ~25nm becomes rather challenging. However, the morphology of the precipitates can be directly compared and it can be seen from the above analysis that true morphology of γ′ precipitates is close to spherical as was seen in EFTEM. Also, due to random distribution of γ′ precipitates inside the matrix, during growth some of the precipitates develop non spherical morphology also seen in 3-D reconstruction.

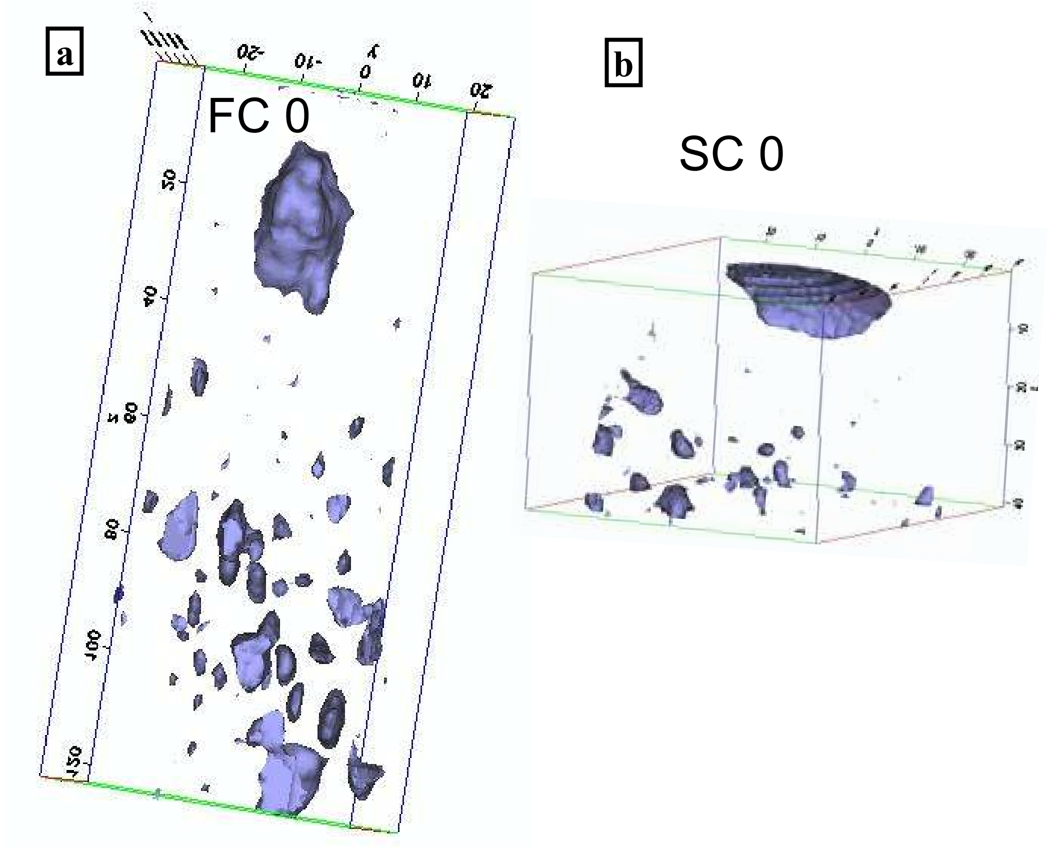

Figure 4.7. (a) FC0 3-D reconstruction showing Cr = 14at% isosurfaces of primary and secondary γ′ precipitates. (b) SC0 3-D reconstruction showing Cr = 14at% isosurfaces of primary and secondary γ′ precipitates.

Figs. 4.7(a) and (b) show similar iso-surface reconstructions with 14at% Cr for fast cooled (FC0) and slow cooled (SC0) samples respectively. Both reconstructions capture a part of primary γ′ precipitate along with several smaller secondary (or maybe tertiary) γ′ precipitates. In between them lies the depletion zone where no γ′ precipitation occurs. One thing to note from 3DAP as well as EFTEM results is that the γ′ precipitates closer to the depletion zone are smaller in size than the ones that are further away. The isosurface analysis also indicates that the depletion zone of primary γ′ in SC0 (~ 40nm) is more than that in FC0 (~20nm) which is in close agreement with the EFTEM analysis (Fig. 4.2). As seen from the 3-D reconstructions, the sizes of the fine scale precipitates are of the order of the smallest precipitates seen in EFTEM micrograph of FC0 and SC0. This alludes to the fact that these precipitates nucleated at very high undercooling where growth of precipitates is expected to be minimal, kinetics being slowest at that temperature. However, due to small sampling volume, a statistical comparison of these fine scale γ' precipitates cannot be performed.

Table 4.2. γ' compositions for WQ0, FC0 and SC0 condition.

	Monomodal γ' precipitates		**Primary γ' Precipitates**				**Secondary γ' precipitates**			
	WQ 0		**FC 0**		**SC 0**		**FC 0**		**SC 0**	
	At %	**Error %**	**At %**	**Error %**	**At %**	**Error %**	**At %**	**Error %**	**At %**	**Error %**
Co	8.83	1.3	7.08	0.2	6.7	0.2	7.73	0.9	7.25	1.8
Ti	10.67	1.3	10.43	0.2	9.17	0.2	9.05	1.0	7.97	1.3
Cr	4.68	0.9	2.48	0.1	1.77	0.1	4.98	0.7	8.12	1.8
Al	10.49	1.1	12.19	0.2	9.03	0.2	11.71	1.1	9.71	1.6

Compositional analysis using IVAS™ software was done after the EFTEM to establish the arguments given for variation in microstructure with variation in cooling rate. After γ' precipitates of different size-scales (primary and secondary) were identified using the isosurface plots, their compositions were determined using the IVAS™ software. This was done by isolating the γ' precipitates from the reconstruction and measuring the bulk composition of primary γ' and secondary γ' precipitates separately. For simplicity, only the primary alloying elements, Co, Cr, Al, and, Ti were considered in this analysis though all the alloying elements in this alloy can analyzed using 3D atom probe, as discussed previously [8]. Table 4.2 summarizes the compositions of the primary and secondary γ' precipitates as a function of the cooling rate with statistical errors. The compositions given in the table suggest that that the primary γ' precipitates in SC0 and FC0 conditions have compositions closer to equilibrium (higher Al and Ti content while being depleted in Cr and Co) as compared to the monomodal γ' precipitates in the WQ0 sample. This is possibly be due to the fact and as proposed earlier that primary γ' precipitates during slow and fast cooling (SC0 and FC0 conditions) form at much lower undercoolings or at higher temperatures where the faster diffusion rates permit these precipitates to grow by partitioning elements and achieve a near-equilibrium composition. This does not happen in the water-quenched case (WQ0) where the nucleation burst occurs at a substantially lower temperature (higher undercooling) and where the growth of the γ' precipitates is reduced. This is clearly the case when one compares the Co and Cr content, which are 6-7at% and 1-2.5at% respectively in the primary γ' precipitates for both FC0 and SC0 conditions; while in case of the monomodal γ' precipitates in the WQ0 case, the corresponding values are 8.8at% and 4.6at%. In contrast, the difference in the contents of Al and Ti between the primary γ' precipitates (SC0 and FC0 samples) and the monomodal γ' precipitates (WQ0 sample) is negligible. This indicates that the diffusivities of Cr and Co are substantially lower than those of Al and Ti. Based on the same logic, the far-from-equilibrium compositions of the secondary γ' precipitates (in terms of Co and Cr enrichment, and Al and Ti depletion) in FC0 and SC0 conditions does make sense, as we know that these precipitates nucleate at much lower temperatures (higher undercooling). Thus the secondary γ' precipitates are 1-2at% enriched in Cr and Co and depleted in Al and Ti with respect to the corresponding primary γ' precipitates in SC0 and FC0 conditions. Also, from the precipitate analysis it can be also found out that the smaller γ' particles in SC0 forming close to the depletion zone are highly enriched in Cr and Co and are therefore farthest from equilibrium. It should also be noted here that the compositions of γ' precipitates in WQ0 and secondary/tertiary precipitates in FC0 and SC0 are also different. The compositions of γ' precipitates in WQ0 are closer to equilibrium as compared to SC0 and FC0 which suggests two possibilities for the variation in the partitioning of elements: (i) γ' precipitates in WQ0 are possibly formed at lower undercooling as compared to FC0 and SC0 which results in change in diffusivity of elements, (ii) The matrix composition when these precipitates form are different in different heat treatment conditions. In addition to these factors, the time available for growth of the precipitates might be different in different heat treated conditions.

Table 4.3. γ composition in WQ0, FC0 and SC0 condition.

SC 0	**γ near primary γ′**		**γ far from primary γ′**		**γ near secondary γ′**	
	At %	**Error %**	**At %**	**Error %**	**At %**	**Error %**
Co	18.63	0.3	13.71	0.3	15.38	1.2
Ti	0.68	0.1	1.21	0.1	2.68	0.5
Cr	24.36	0.4	24.51	0.4	23.75	1.6
Al	1.97	0.1	1.67	0.1	3.76	0.6

Based on the same arguments, the matrix composition would also be different in different conditions. This was confirmed by measuring the actual composition of the γ phase near the primary γ', near secondary γ' and far away from primary γ'. The terms "near" and "far" qualitatively correspond to distance from 14at% Cr isosurface into the matrix. From Table 4.3, which compiles the matrix compositions for different regions in SC0 sample, it can be said that the composition of γ near the secondary γ' is also far away from equilibrium in terms of excess Al and Ti and depleted Cr and Co. In fact the compilation clearly shows that γ composition is close to equilibrium in regions nearer to the primary γ' particles than further away. These near-equilibrium regions are identified by higher amounts of γ-stabilizing elements like Cr and Co and lower γ'-stabilizing elements like Al and Ti (refer Table 4.3). These regions are less conducive for further nucleation of γ' phase and thus are labeled as “depletion zones”. This also complements the fact that once the equilibrium is reached in terms of composition, no further driving force for nucleation is available and hence results in precipitate free zones around the primary γ' precipitates.

4.5 Precipitation of γ′ as a Function of Different Cooling Rate Conditions

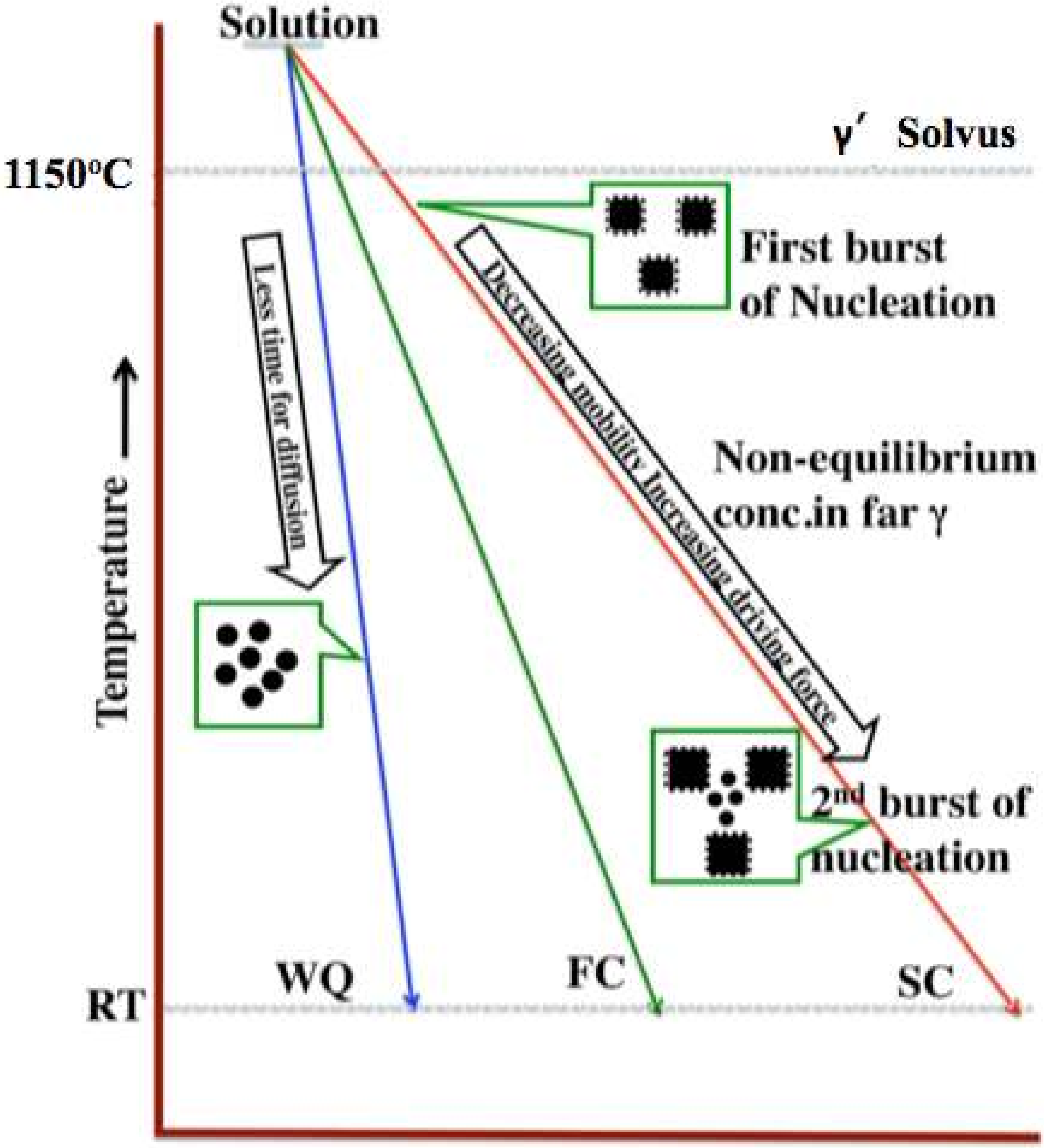

Figure 4.8. Schematic showing the formation of different generations of γ′ precipitates with different cooling rates WQ0 and SC0.

With above results and arguments based on the 3DAP composition data and EFTEM analysis, the precipitation mechanism that involves the complexity of concurrently occurring thermodynamic and kinetic phenomenon during various cooing rates can be explained. The effect of cooling rate on the overall γ′ precipitation mechanism can be explained via the schematic drawn in Fig. 4.8. For all three cooling rates, as the sample is cooled below the solutionizing temperature, with increasing undercooling, the volumetric free energy term, ΔG_v, continues to increase until the critical nucleation barrier ΔG^* is sufficiently low, permitting the first burst of nucleation to take place. However, for precipitation event to occur some critical composition of the phase to be precipitated (γ′) has to occur. This would be dependent on the kinetic factors as well, which differ with cooling rate. In case of water quenching treatment (WQ0), due to the faster cooling rates (>300°Cmin^{-1}), the under-cooling is maximum when the above mentioned nucleation event occurs (leftmost curve in Fig. 4.8). Maximum undercooling is required in WQ0 because the time available for precipitation to occur is minimum in WQ0. As the precipitates nucleate at high undercooling, a high nucleation rate is expected to occur which increases exponentially with undercooling. Due to very high nucleation rate at this undercooling the nucleation density of the γ′ precipitates is very high. Also at this high undercooling (lower temperature) diffusion is rather limited which coupled with the superimposed fast quench rate allows only very limited time for partitioning of the alloying elements between the γ′ and γ phases. Consequently, the γ′ precipitates have far-from equilibrium compositions (high in Cr and low in Al), as shown in Table 1(a). These precipitates also develop necked regions due the overlap of their diffusion fields. The diffusion fields of various precipitates is observed since the inter particle distance is of the order of γ′ precipitate size due to high nucleation density. This along with the above factors like very high nucleation density and low diffusivity, results in restricted growth of γ′ precipitates, thus maintaining a spherical morphology. The high cooling rate during water-quenching prevents any further nucleation events despite the fact that non-equilibrium conditions exist. So a monomodal size distribution of γ′ precipitates is observed (Fig. 4.1).

On the other hand, the results of the other extreme of water quenched, the SC0 condition, suggests a different mechanism. The precipitation process changes significantly during slow-cooling (SC0 sample), in terms of nucleation and growth of γ′ precipitates. At slow cooling rates (~24°Cmin^{-1}), the first generation of γ′ precipitates (primary γ′) are nucleated at relatively higher temperatures (lower undercooling), where diffusion rates are sufficiently rapid. This permits equilibrium to establish between γ′ and γ compositions near the interface, thus resulting in equilibrium precipitate compositions (rightmost curve in Fig. 4.8). However due to continuous cooling of the sample the equilibrium is established only near the interface resulting in depletion zone. This is evident from the composition of the primary γ′ precipitates in Table 4.2 for the SC0 sample. Also at these relatively elevated temperatures the nucleation rate is quite low, resulting in a low number density of these precipitates, separated by large distances (refer Fig. 4.3). These particles grow due to diffusion-mediated transport of elements like Al and Ti into the precipitate and rejection of γ-stabilizing elements like Co and Cr. While local γ′-γ equilibrium (end points of the thermodynamic tie line in the γ+ γ′ two-phase field) is easily established across the precipitate/matrix interface, the limited time at that temperature reduces the diffusion distances and consequently the long-range γ composition does not reach equilibrium. This also suggests that equilibrium volume fractions are also not achieved at each temperature during the cooling. The equilibrium process is only limited to few tens of nanometers from the interface. As the precipitates grow the long-range diffusion fields from two adjacent primary γ′ precipitates start overlapping overlap (often referred to as soft impingement). Once these diffusion fields start interacting with each other (which happens quickly after the first nucleation event when diffusivities of elements are high) there is not sufficient driving force for new nucleation between these adjacent γ′ precipitates at that temperature. In other words, the matrix between the adjacent γ′ precipitates starts getting depleted. However, since the diffusivity of elements decay as a function of distance from the interface, the depletion of matrix is different far away from precipitates as compared to close to interface, which gets highly depleted and reaches equilibrium. On the other hand, even though depletion of Al and Ti occurs away from the interface, it is not as prominent as precipitate free zone. So, the γ matrix region between the primary γ′ precipitates, away from the growing γ′/γ interfaces retains a far-from equilibrium composition. With decreasing temperature during continuous cooling, there is a continual increase in the driving force of nucleation with the maximum being in the γ regions in between the primary γ′ precipitates. Eventually, the critical nucleation barrier ΔG^* at a lower temperature is low enough to have a second burst of nucleation, thus forming very fine distribution of secondary γ′ precipitates in the regions in between the primary γ′ precipitates, with the "depletion zone" separating the secondary γ′ precipitates from the primary ones (rightmost curve in Fig. 4.8). These secondary precipitates appear to be forming at temperatures even lower than those at which the monomodal γ′ precipitates nucleated during water-quenching (WQ0 sample) (refer Fig. 4.1). Similar to the monomodal γ′ precipitates; these secondary precipitates are typically spherical and exhibit a large nucleation density (Fig. 4.3(b)). They are substantially smaller in size as compared to the monomodal γ′ precipitates, and are further away from equilibrium in terms of composition, as shown in Table 4.2. It should be noted that on further cooling, depending on the supersaturation remaining in the γ matrix, additional nucleation bursts can occur resulting in multimodal size distributions of γ′ precipitates in the microstructure. The third burst of nucleation and the details are presented in the next chapter.

Finally during fast cooling (FC0 sample) an intermediate cooling rate is encountered by the sample, and this case also exhibits the presence of multimodal size distribution of precipitates similar to the SC0 sample (middle curve in Fig. 4.8). In case of the FC0 sample too, near-equilibrium composition primary γ′ precipitates and far-from equilibrium secondary γ′ precipitates are formed. After first burst of nucleation in FC0, the second burst of nucleation would happen at a very high undercooling. The undercooling in FC0 for secondary nucleation is expected to be more as compared to SC0 as the cooling rate in FC0 is much higher than SC0. Higher undercooling in FC0 would result in smaller secondary γ′ precipitates as compared to SC0 which is what was observed in EFTEM images. However, due to the complexity of the different competing thermodynamic and kinetic factors like increasing driving force with decreasing temperature, formation of depletion zones and supersaturation of matrix, change in equilibrium γ′ phase composition and volume fraction with reducing temperature and decreasing diffusion mobiliites, it is difficult to determine the exact mechanism leading to the differences in the size and composition for secondary γ′ particles in FC0 and SC0 heat-treated conditions.

4.6 Summary

The experimental 3DAP results and EFTEM analysis presented in this chapter indicate that there is a strong influence of the cooling rate on the formation of different generations of γ' precipitates, their size, morphology and composition, along with the partitioning of elements across the γ/γ' interface. With increase in cooling rate, the size of the primary and secondary γ' precipitates decreases due to the limited time available for diffusion and reduction in mobility of elements thereby affecting the growth of the γ' phase. These kinetic factors also result in non-equilibrium compositions of the secondary (and in some cases tertiary) γ' precipitates forming at high undercoolings. More detailed investigations of the different generation of γ' as well as mechanism of formation of their formation are presented in the next chapter.

4.7 References

[1] D. Blavette, E. Cadel, B. Deconihout, Mater. Char. 44 (2000) 133.

[2] M.K. Miller, Micron 32 (2001) 757

[3] D.N. Seidman, C.K. Sudbrack, YE. Yoon, Journal of Mater. 58 (2006) 34

[4] Y. Zhang, N. Wanderka, G. Schumacher, R. Schneider, W. Neumann, Acta Mater. 48 (2000) 2787

[5] S.S.A. Gerstl, D.N. Seidman, A.A. Gribb, T.F. Kelly, Adv. Mater. Process. 162 (2004) 31

[6] P.M. Sarosi, G.B. Viswanathan, D. Whitis, M.J. Mills, Ultramicrosc. 103 (2005) 83

[7] S.T. Wlodek, M. Kelly, D.A. Alden, in: R.D. Kissinger, D.J. Deye, D.L. Anton, A.D. Cetel, M.V. Nathal, T.M. Pollock, D.A. Woodford (Eds.), Superalloys 1996, TMS, Warrendale (1996) 129

[8] J.Y. Hwang, R. Banerjee, J. Tiley, R. Srinivasan, G.B. Viswanathan, H.L. Fraser, Metall. Mater. Trans. A. 40 (2009) 24

[9] A.J. Ardell, Acta Metall. 20 (1972) 61

[10] D.J. Chellman, A.J. Ardell, Acta Metall. 22 (1974) 577

[11] A.J. Ardell, R.B. Nicholson, Acta Metall. 14 (1966) 1295

[12] R. Radis, M. Schaffer, M. Albu, G. Kothleitner, P. Polt, E. Kozeschnik, Acta Mater. 57 (2009) 5739

[13] G. Boussinot, A. Finel, Y.L. Bouar, Acta Mater. 57 (2009) 921

[14] O.C. Hellman, J.A. Vandenbroucke, J. Rusing, D. Isheim, D.N. Seidman, Microsc. Microanal. 6 (2000) 437

CHAPTER 5

FORMATION OF DIFFERENT GENERATIONS OF γ' PRECIPITATES DURING CONTINOUS COOLING

5.1 Introduction

Previous chapter discussed the effect of cooling rate on the morphology size, and distribution of γ'. However, the chemical partitioning leading to the microstructural evolution causing different generations of γ' is a focus of this chapter. Slow cooling rates lead to the formation of γ' precipitates with a bimodal size distribution or in some cases even a multi-modal size distribution [1-5]. The development of multiple size ranges of γ' precipitates during continuous cooling has often been attributed to multiple distinct bursts of nucleation of precipitates at different undercoolings below the γ' solvus [3, 4]. These multiple nucleation bursts in turn result from the complex interplay of continuously increasing thermodynamic driving force for nucleation (chemical free energy difference) due to increasing undercooling, reduction in this driving force due to previous nucleation events and the rapidly declining diffusivity of alloying elements with decreasing temperature. At lower undercoolings (or higher temperatures, just below the γ' solvus temperature) lower driving force for nucleation coupled with higher diffusivities leads to the first burst of γ' nucleation forming the first generation of precipitates with low nucleation density, often referred to as primary γ' precipitates. At higher undercoolings reduced diffusivity of atoms leads to supersaturation of γ' forming elements away from the diffusion fields of the growing primary γ' precipitates, and coupled with a greater thermodynamic driving force results in further bursts of nucleation consequently forming secondary (or tertiary in some cases) γ' precipitates with a high nucleation density [1, 3, 4]. Therefore the three primary objectives of this chapter are as follows:

1. Analysis of the size distribution, morphology and composition of multiple generations of γ′ precipitates formed during continuous cooling at a relatively slow rate from the solutionizing temperature (single γ phase field) and subsequent aging – Multi-scale characterization approach coupling 3DAP, EFTEM, and SEM.
2. Detailed compositional analysis of the different generations of γ′ precipitates as well as their near and far field γ compositions using 3DAP.
3. Investigation of γ- γ′ compositional partitioning and associated diffusion fields.
4. Mechanism of formation of different generations of γ′.

5.2 Experimental Procedure

The samples were supersolvus solution treated in a vacuum furnace at 1400°C in the single γ phase field above γ′ solvus [6] for 60 minutes to dissolve any existing γ′ and then slow cooled at an average cooling rate of 24^{o}Cmin^{-1} (SC0) and 5oCmin^{-1} (ESC) in the APS facility and the diffraction pattern was recorded for different temperatures during cooing. Samples for 3DAP tomography studies in the LEAP microscope were prepared by focused ion beam milling technique. For this purpose, samples were prepared by dual-beam focused ion beam (FIB) instrument (FEI Nova Nanolab 200) system using a Ga ion beam. The ion beam thinning was carried out in multiple steps, starting with 30kV ions and finally finishing with 5kV ions to reduce the surface damage caused by the higher energy ions [7, 8]. The final tip diameter of the atom probe specimens was ~ 50 – 80nm. The 3DAP experiments were carried out using a LEAP 3000 local electrode atom probe (LEAP™) system from Imago Scientific Instruments Inc. All atom probe experiments were carried out in the electric-field evaporation mode at a temperature of 70K, with the evaporation rate varying from 0.2 – 1.0% and the pulsing voltage at 30% of the steady-state applied voltage.

TEM samples were also prepared via conventional routes, consisting of mechanical grinding and polishing of 3mm diameter discs, followed by dimple grinding, and final ion-beam milling to electron transparency. Ion beam milling was conducted on a Gatan Duo Mill and Fischione Model 1010 ion milling system, operated at 6kV. TEM analysis was conducted on a FEI Tecnai F20 field emission gun transmission electron microscope operating at 200kV. Images were obtained using the Cr M-edge in the energy filtered transmission electron microscopy (EFTEM) mode, as described elsewhere [9]. Representative regions were imaged at different magnifications to capture the relevant secondary and/or tertiary γ' precipitates in the alloy.

SEM analysis of primary γ' precipitates were done using backscattered detector on etched samples. Prior to SEM analysis the samples were polished and etched using 15ml HCl + 10ml Glycerol + 5ml HNO_3. Light etching substantially enhances the contrast between γ and γ' phase in secondary electron imaging mode of the SEM.

5.3 Multiple Nucleation Bursts of γ' Precipitates Probed In-situ using Synchrotron Studies

During slow cooling of Rene88DT from γ' solvus temperature, the interplay between thermodynamic and kinetic factors gives rises to multiple nucleation bursts of γ' precipitates. These nucleation events were captured by direct observation of the intensities of γ' superlattice reflections and basic γ reflections.

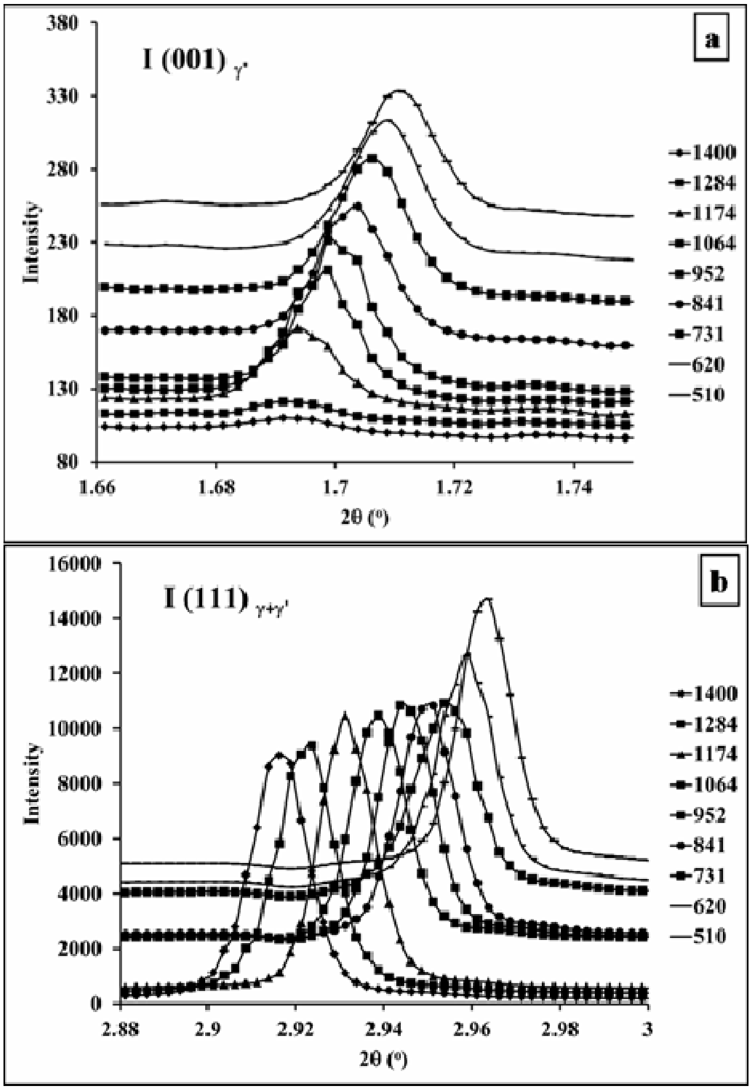

Figure 5.1. (a) Variation of (100) intensity at different temperatures during continuous cooling at 25^{o}Cmin^{-1}, (b) Variation of (111) intensity at different temperatures during continuous cooling at 25^{o}Cmin^{-1}.

During continuous cooling of Rene88DT sample during synchrotron experiment, the x-ray diffraction pattern was recorded continuously. The ring pattern was then converted into intensity versus 2θ plot. The wavelength of synchrotron x-ray being $\lambda = 0.10785A^{o}$ permits measurement of very small changes in lattice parameter. Fig. 5.1(a) and (b) show an enlarged view of the intensities of (001) γ' superlattice and (111) $\gamma + \gamma'$ basic reflections at different temperatures during slow cooling at 24^{o}Cmin^{-1}. Fig 5.1(a) shows a sudden increase in

(001) intensity after 1284°C which then increases gradually with lowering of temperature. This suggests that the formation of γ' took place around 1200°C. In addition, the shift in the position of the peak also gives an indication of in lattice parameter; decreasing with decrease in temperature. The intensity of (111) reflection as shown in Fig. 5.1(b) also shows a similar trend; however, a sudden change in intensity of (111) is not observed. (111) being an allowed reflection for both γ' and γ intensity of (111) appears as a result of combination of γ' (111) and γ (111) intensities. The combined intensity of (γ' + γ) (111) reflection also shows a gradual change in the peak position. The intensity of γ' (111) however gives a qualitative measure of γ' formation. Similar results were obtained for samples that were cooled at 5°Cmin^{-1} (ESC). The intensity of (001) reflection for γ' continuously increase as seen in Fig. 5.2(a) and intensity of (111) doesn't show much change (Fig. 5.2 (b)).

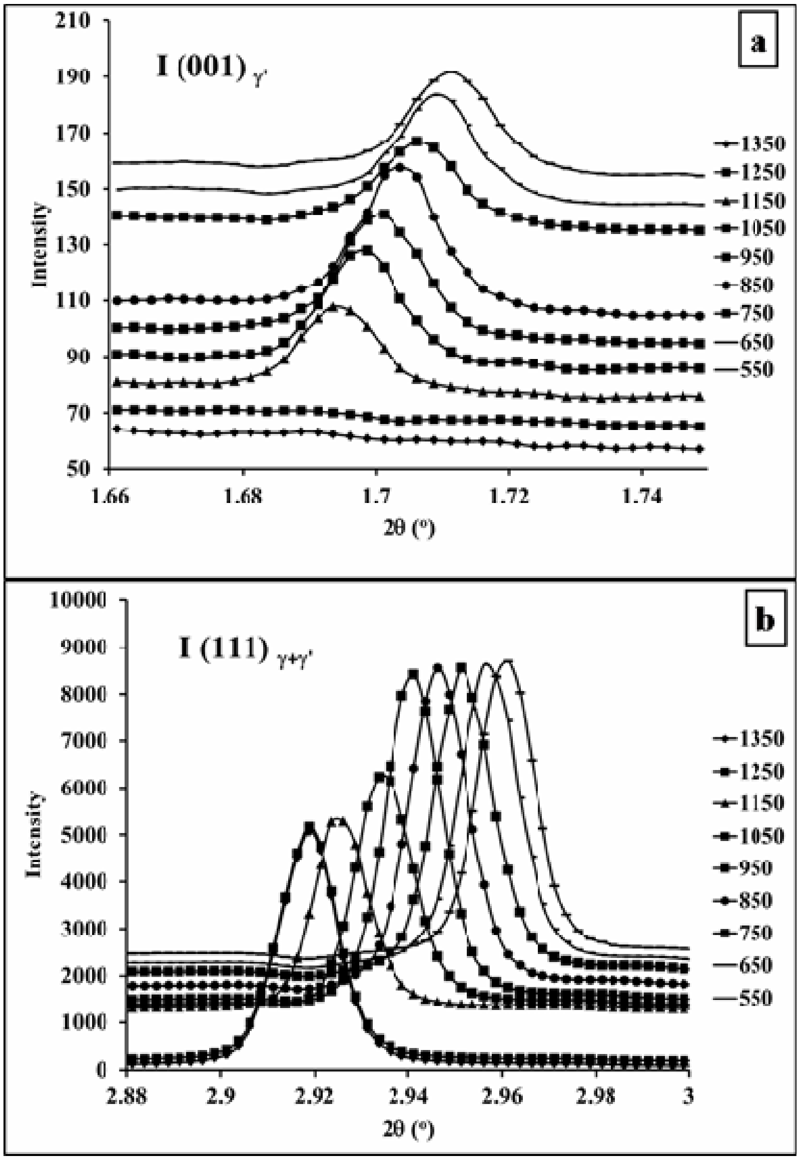

Figure 5.2. (a) Variation of (100) intensity at different temperatures during continuous cooling at 5^{o}Cmin^{-1}, (b) Variation of (111) intensity at different temperatures during continuous cooling at 5^{o}Cmin^{-1}.

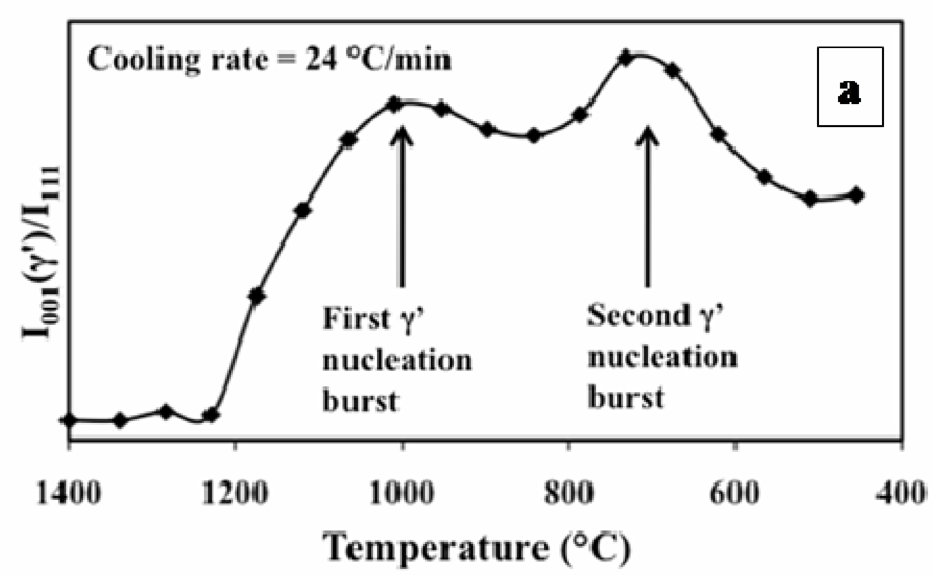

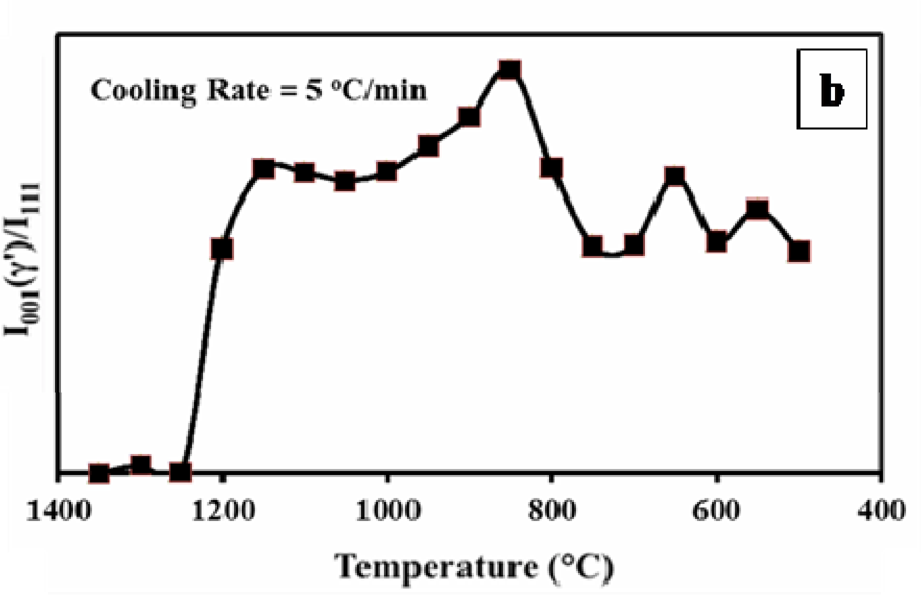

Figure 5.3. Intensity ratio plots for samples cooled at (a) 24oCmin^{-1} and (b) 5^{o}Cmin^{-1}.

The variation of γ′ intensities can be qualitatively measured by the ratio m = (001)γ′/(111) γ′ + γ as seen in Fig 5.3(a). The figure clearly shows two sudden increases in the m factor at two distinct temperatures. These rapid changes in the m factor give an indication of two different γ′ nucleation bursts, resulting in a multimodal size distribution of γ′ precipitates. It is however important to note that the intensity depends on the equilibrium volume fraction of γ' and with decrease in temperature the volume fraction of new γ' also decreases which gives rises to a smaller change in m ratio with different nucleation bursts. A possible third burst of nucleation is also possible at much lower temperatures but due to very small change in the volume fraction of γ', it is rather difficult to see any sudden changes in m ratio. The figure also shows that nucleation and growth of these precipitates occurs over a specific range of temperatures where the kinetics of γ to γ' transformation and precipitate growth are high along with thermodynamic driving force. Fig 5.1(a) and (b) as mentioned show the shifting of intensity peaks indicating change in lattice parameter for both γ' and γ with decrease in temperature. This decrease in lattice parameters is due to the integrated effect of thermal expansion and the chemical partitioning between γ' and γ phase. However, the changes in lattice parameters are not equal for γ' and γ' as seen in the figure which gives rise to increase in the lattice mismatch between γ' and γ with decrease in temperature. The change in lattice parameter is higher for γ and compared to γ'. This also alludes to the fact that the ordered γ' phase is more stable with respect to change in temperature and therefore the change in lattice parameter with temperature is minimal. The intensity ratio plots for ESC are shown in Fig. 5.3(a) and (b) which suggest multiple nucleation bursts when the sample is cooled at 5^{o}Cmin^{-1}. It is possible that in ESC the number of nucleation bursts are more as compared to SC0; however, to validate this argument, the results need further analysis. This chapter focuses only on the SC0 condition which shows multiple bursts and similar arguments can be applied to ESC.

5.4 Development of γ' Precipitates Size, Distribution and Morphology During Continuous Cooling

Slow cooling (SC0) of Rene88DT from γ' solvus after solutionizing resulted in multimodal distribution of precipitates as mentioned earlier. The size, morphology and density of these precipitates depend on the stage at which the nucleation events occur during cooling process and growth and coarsening processes occurring at different stages govern the final morphology and size of these precipitates. To probe the individual generation of γ' for their size and morphology, different characterization techniques were employed.

Fig 5.4(a) shows a backscattered SEM image of etched SC0 sample with γ' appearing darker. As seen from the figure the primary γ' develop cuboidal to irregular morphology either due to coarsening or impingement of neighboring γ' precipitates. The primary γ' precipitates have low number density as they are formed at low undercooling and it would reduce as they coarsen. It can also be seen that in SC0 also exhibits high number density of secondary γ' precipitates between primary γ' separated by a depletion zone. At higher magnification it can be seen that some γ' precipitates are either in impingement stage and some have joined to form irregular shaped precipitates and some remain cuboidal. There is a large variation in shape and size of the primary γ' precipitates as can be seen from Fig. 5.4(b). The size distribution of primary γ' precipitates (the diameter of precipitates calculated based on area assuming the precipitates to be spherical) was measured from these images (shown later). It was observed that there was a large variation in size of the precipitates ranging from 100 - 400nm in diameter with maximum precipitates in the size range of 150 - 250nm. The precipitates of this size range are best measured using SEM with minimum statistical errors. The smaller secondary were not in these images possibly because of over etching of the smaller γ' and low magnification of these images.

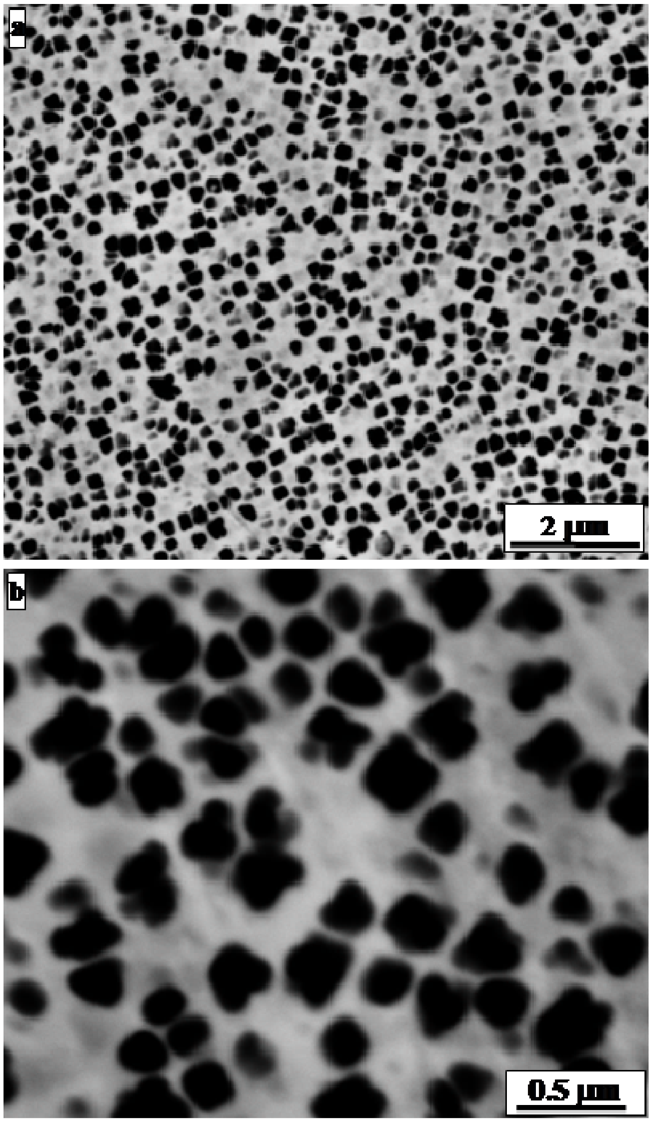

Figure 5.4. (a) Backscatter SEM image showing primary γ′ precipitates in SC0, (b) Higher magnification backscatter image showing cuboidal to irregular shaped γ′.

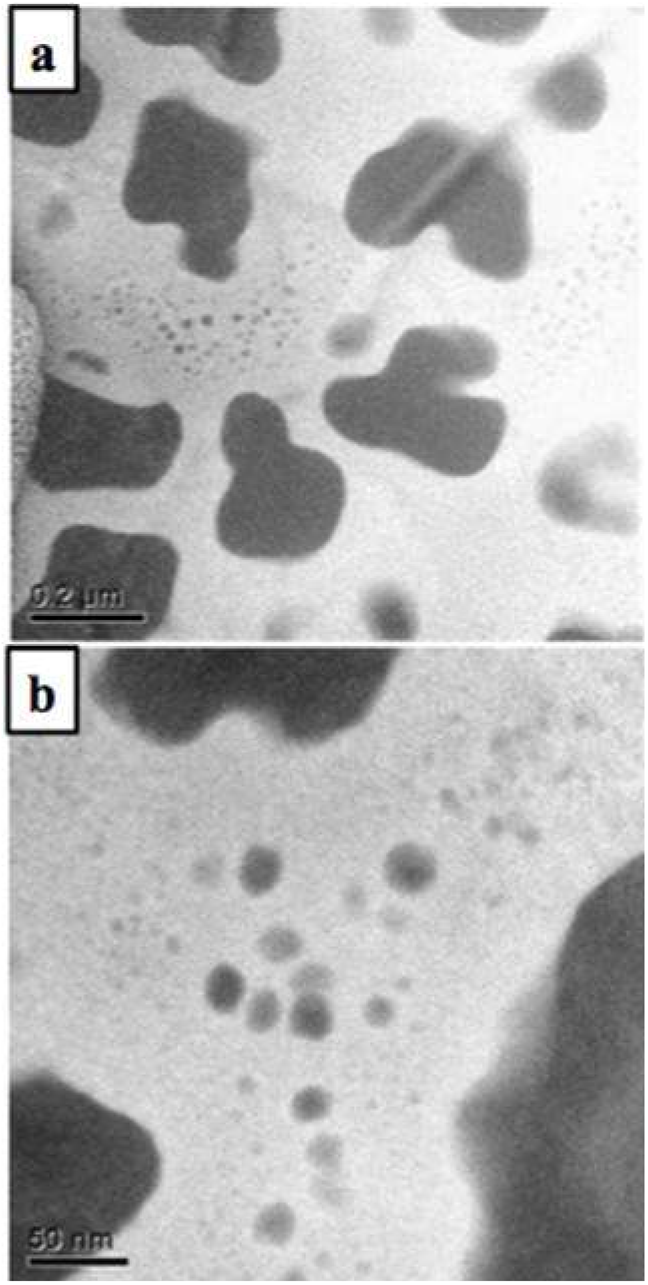

Figure 5.5. Energy-filtered transmission electron microscopy (EFTEM) images constructed using Cr M-edge in the EELS spectrum from solutionized and slow cooled SC0 sample (a) showing primary and secondary γ′ and (b) showing small tertiary γ′ between secondary γ′ and depletion zone. The γ′ precipitates, which are Cr depleted, exhibit the darker grey contrast in these images.

The secondary γ' population that nucleates at lower temperature due to very high thermodynamic driving force grows at much lower rates due to limited diffusivity as was seen at a second hump in the "m ratio" of the x-ray diffraction data (Fig. 5.3(a). This second generation of precipitates (Fig. 5.5(a)) forming away from primary γ' separated by depleted zones exists with a high number density. The very high number density of these precipitates is a result of high nucleation rate at high undercoolings. Due to limited growth these secondary γ' precipitates exhibit near to spherical morphology with size ranging from 10-30nm in diameter. At this scale analysis of EFTEM micrographs is the most suitable technique to find out statistical size and distribution of these precipitates. Smaller precipitates appear lighter in contrast due to the averaging effect of the 2D projected TEM image of γ' embedded in γ matrix. The size distribution for secondary γ' precipitates was measured using the EFTEM micrographs for the secondary precipitates. The size of these precipitates ranged from 12 - 30nm in diameter; however, most of the precipitates are in the range on 12 - 20nm. It was observed from the EFTEM analysis that the secondary γ' population was only restricted to the regions away from the primary γ' precipitates. The primary γ' precipitates that were close to each other did not contain any colony of secondary γ' precipitates between them. This suggests that the diffusion field overlap is large, the γ region gets severely depleted in solute resulting in no precipitation of γ' at lower temperatures. Another colony of precipitates seems to exist between the γ' depleted zone and secondary γ' precipitates (Fig. 5.5(b)), a lot smaller than secondary, a result of possible third burst of nucleation at much lower temperatures. But due to their very small size and limitations of EFTEM, it is hard to know the true size and distribution of these precipitates.

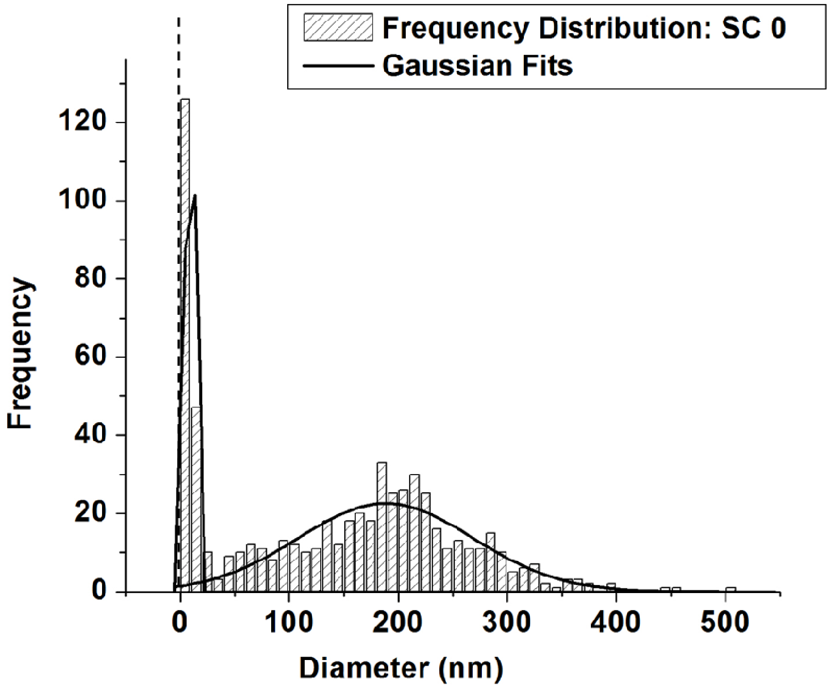

Figure 5.6. Frequency size distribution of multiple generations of γ′.

The overall size distribution of different generations of γ′ is shown in Fig. 5.6. This distribution covering different scales of γ′ has been reported by modeling using classical nucleation theory. However, the experimental evidence of the size distribution of different bursts of nucleation has never been shown. As seen in the figure, both bursts of nucleation give rise to different size scale of γ′ and each nucleation event probably occurring in a range of temperature where the driving force for nucleation is high before it reaches minimum. All three generations of γ′ show similar distribution; however, the frequency values are just arbitrary. The average diameter of primary γ′ precipitates is about 191nm with standard deviation of 78nm which is close to the fitted peak of gaussian at 188nm. Secondary γ′ precipitates have average diameter of 8nm and a standard deviation of 7nm which is also close to the peak of the gaussian at 9nm.

Therefore gaussians are in close agreement with the frequency distributions of the two generations of γ'. A third population of γ' precipitates is seen in the EFTEM images; however, it is difficult to quantify this third generation using EFTEM which is lot smaller than primary and secondary populations. It has been shown and reported that secondary and tertiary generations of γ' have much higher number density as compared to primary; however, the above distribution also suggest during each nucleation burst which occurs over a range of temperature most number precipitates nucleate at lower temperature (highest peaks of distribution) giving rise to close to exponential distribution, which otherwise would be closer to a normal distribution if all precipitates in each generation nucleated at a single temperature with almost similar sizes. A dashed line is shown in the figure which represents the third γ' generation (tertiary); however, as mentioned above the third population cannot be quantified using EFTEM, hence shown as a line. The distribution also shows that the size difference between primary and secondary γ' is more compared to secondary and tertiary γ'. In other words, the size range of tertiary and secondary γ' is closer as compared to primary γ'. This could be due the diffusivity of elements that are high very high at high temperature (steep part of curve) and decrease exponentially at lower temperatures and becomes almost constant at lower temperatures. After the first burst of nucleation due to continuous decrease in temperature and hence continuous decrease in diffusivities of elements, the primary γ' precipitates do not grow to reach their thermodynamic equilibrium volume fraction and have a tendency to grow but are limited by the kinetic factors involved. Similar effect is experienced by the successive generations of γ' which is further complicated by the continuous change in composition of γ that would have an effect on the thermodynamic driving force for nucleation of different generations of γ'.

5.5 Chemical Partitioning Between γ′ and γ for Different Generations of Precipitates

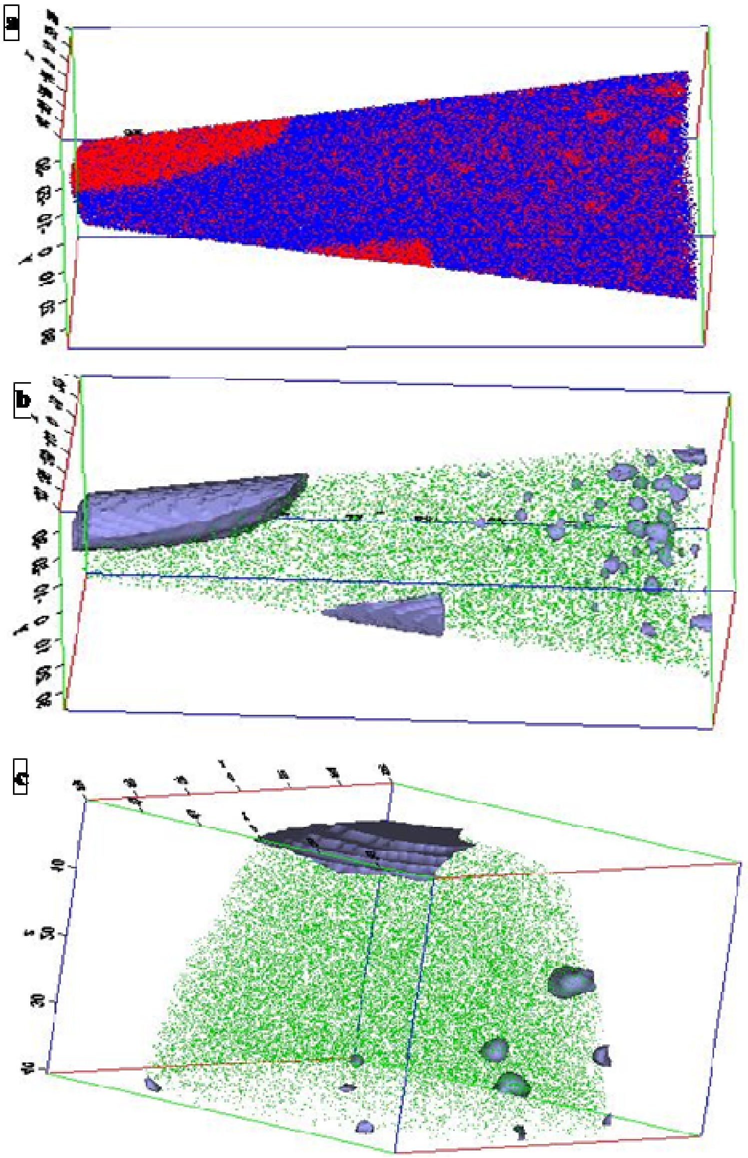

Figure 5 .7. (a) 3DAP reconstruction of Co (blue) and Al (red) atoms in SC0 atom probe sample. The γ′ precipitates are the Al-rich red regions with Co-rich blue matrix. (b) Different depiction of the same SC0 3-D reconstruction showing Cr = 14at% isosurfaces and Ni ions in green showing primary and tertiary γ′. (c) Another region of same SC0 sample.

Due to a large difference in size and the temperature at which primary and tertiary γ′ precipitate, they are expected to have the maximum difference in terms of composition. Fig. 5.7(a) represents a 3 dimensional atom probe reconstruction of SC0 sample that was heat treated in APS facility for in situ x-ray diffraction analysis. For simplicity, only two ions are showed in the figure. The red ions represent Al ions whereas blue represent Cr ions. It can be directly seen from the ion reconstruction that Al and Cr are partitioning to γ' and γ respectively. A better visual representation of the 3 dimensional reconstruction is shown in Fig. 5.7(b). It shows a Cr 14at% isosurface along with Ni ions. The isosurface clearly shows tertiary γ' precipitates inside the γ matrix, depletion zone and the primary γ' precipitate. It is the difference in sizes that clearly distinguishes primary and tertiary precipitates. The primary γ' precipitates forming at lower undercooling reach close to equilibrium composition. However, the compositions of tertiary γ' forming at lower temperatures exhibit non-equilibrium compositions as was shown in chapter 2.

The primary γ' are highly enriched in Al and Ti and depleted in Cr, Co and Mo whereas the tertiary γ' have lower Al and Ti and higher Co and Cr. Even though there is a variation in size of tertiary γ' the variability in composition among all the tertiary γ' observed was minimal. This suggests that even though one generation of γ' forms over a range of temperature, large variation in composition within a particular generation is not observed because of minimal growth of tertiary γ'. The isosurface distinguishes tertiary γ' from the matrix; however, from the raw ion reconstruction as shown in Fig. 5.7(a) there are pockets of local enrichment of Al ions between tertiary γ' and the depletion zone. These small pockets possibly have far from equilibrium but still depleted in Cr and enriched in Al as compared to matrix. More analysis of this region is done later. However, since each generation of γ' has a different composition, the γ region near the γ' also have different composition associated with γ'.

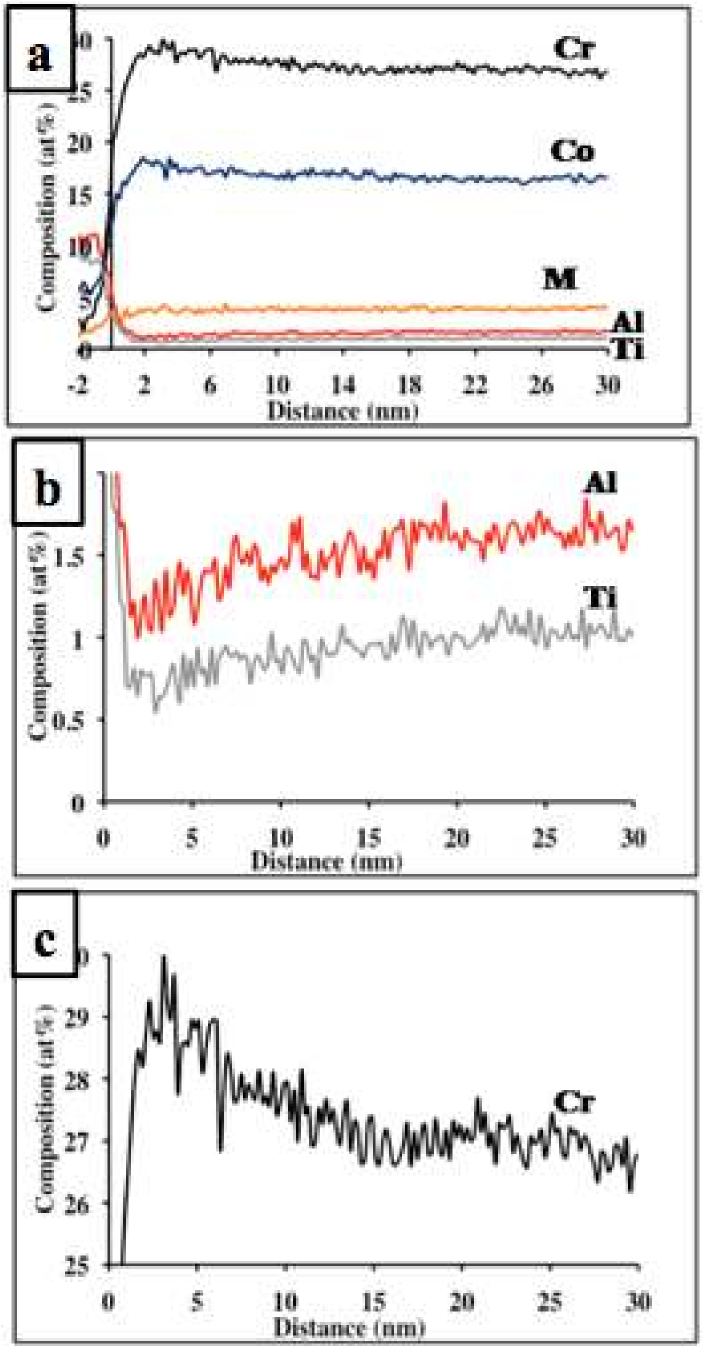

Figure 5.8. (a) Proxigram showing the composition profiles of Co, Ti, Cr, Al and Mo atoms across primary γ′/γ interface (b) enlarged view of Al and Ti composition profile close to interface, (b) enlarged view of Cr composition profile close to interface.

As show in Fig 5.8(a) depletion zone next to primary γ′ reaches equilibrium γ composition as shown by proxigram across primary γ′ precipitate. The proxigram also shows higher Al and Ti content in primary γ', whereas, the depletion zone is enriched in Cr and Co. The compositional gradient across the interface also appears sharp. Mo partitioning across the interface is not large due to low diffusivity of Mo. A closer look of the Al and Ti content in depletion zone is shown in Fig. 5.8(b) using a proximity histogram. It can be clearly seen that right next to the interface there is a local depletion of Al and Ti (approximately 1at% and 0.5at%) which gradually increases (1.7at% and 1at% respectively) inside the depletion zone. This shows that even though depletion zone is highly depleted in Al and Ti, there exists a compositional gradient; however, this gradient is less as compared to compositional gradient at the interface. The proximity histogram depletion zone width is comparable to the EFTEM depleted zone width. As seen in the Fig. 5.8(c) the Cr composition across the interface follows a similar trend. There is a local enrichment of Cr next to the interface (30at%) which slowly decays to 27at% inside the depletion zone. However, this composition away from the interface is enriched in Cr as compared to average composition and hence is considered as depletion zone. Even though the primary γ' precipitates are formed at higher temperature, due to continuous cooling and growth, these precipitates may have internal compositional variation and similarly the compositions of elements in the depleted zone are not constant as well. Away from the γ' the compositions of elements slowly go from almost equilibrium to non-equilibrium compositions gradually which leads to formation of the depletion zone.

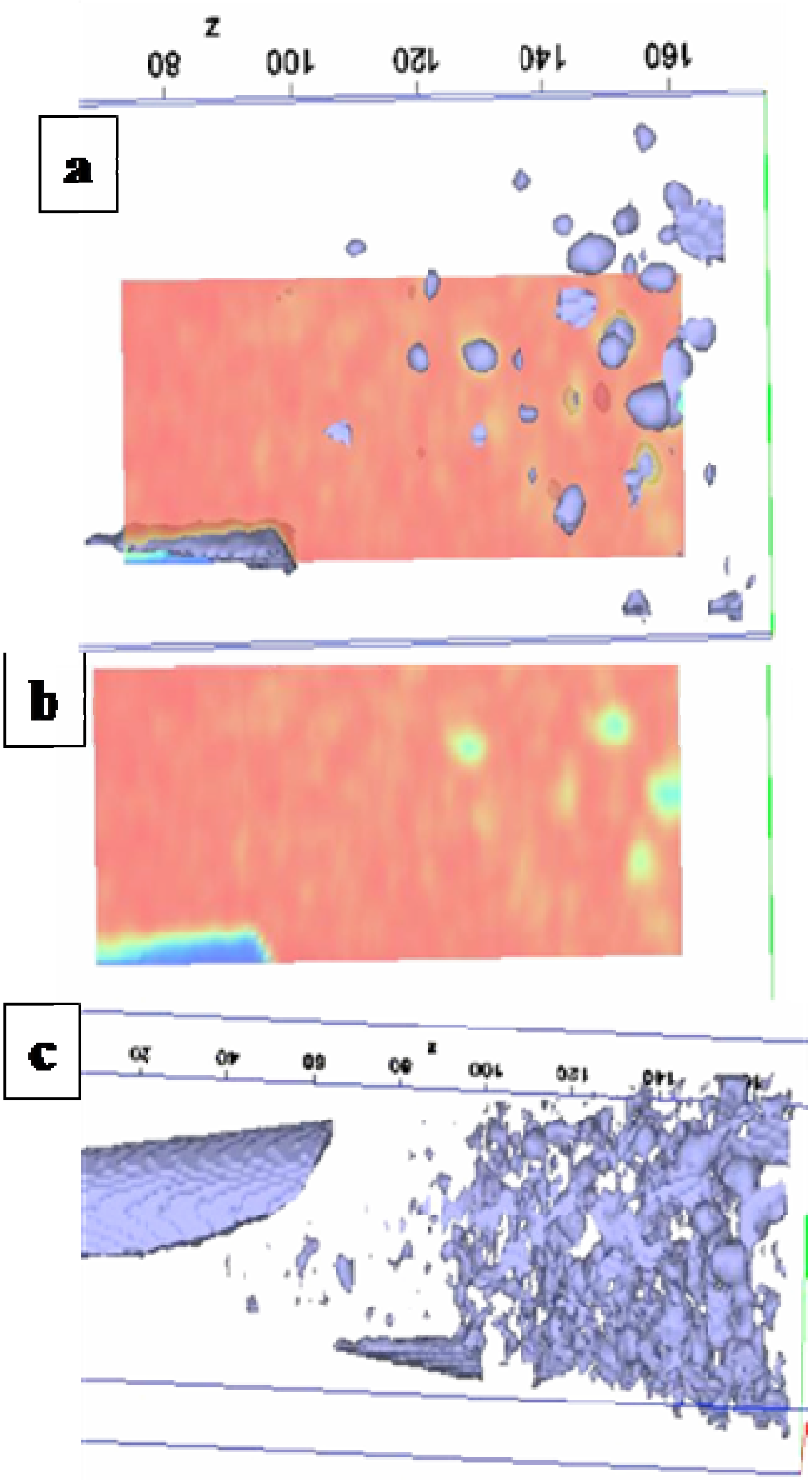

Figure 5.9. (a) 2-D composition map of Cr showing variation in composition in the matrix (yellow being Cr depleted and red being Cr enriched), also showing Cr = 14at% isosurface (c) 2-D composition may of Cr showing some regions highly depleted in Cr, (c) Cr = 18at% isosurface showing primary γ′, depletion zone and interconnected network of γ′.

The compositions of primary and tertiary γ′ show close to equilibrium and far from equilibrium conditions, and decrease in size of tertiary precipitates close to the depleted zone (EFTEM and 3-D isosurface reconstruction). However, a closer examination of the γ region near the depletion zone reveals some interesting results. A 2-D compositional map of Cr was created (2nm in thickness) across primary γ′, depleted zone and tertiary γ′ as shown in Fig. 5.9(a). This 2-D plane intersects the region of Cr = 14at% isourface which represent tertiary γ′. The 2-D map shows continuous interconnected regions of Cr depletion between tertiary γ′ and the depletion zone. It is important to note that Cr = 14at% isosurface only shows regions that have Cr content equal to 14at% or less. Fig. 5.9(b) clearly shows that there are pockets that are locally depleted in Cr but haven't reached the composition close to 14at%. The regions that reach 14at% composition away from the depleted zone appear light blue in color which a yellow region around them that shows a continuous variation of Cr across the interface and attain spherical morphology. However, there are a lot of regions that are not spherical and have interconnected nature. This is again reflected by Cr = 18at% isosurface as in Fig. 5.9(c). It shows that, away from depletion zone a lot of interconnected pockets are depleted in Cr (similar to γ′) but farthest away from equilibrium and only small regions close to equilibrium composition (small blue region inside tertiary γ′). This is an indication of spinodally decomposed matrix as suggested by Cahn [10] which would show a continuous variation in composition rather than discrete pockets that reach equilibrium composition which happens in phase separation by classical nucleation and growth. It needs to be reiterated that these regions that show continuous network of Cr depleted pockets are farthest sway from equilibrium that are formed at highest undercooling where probability of spinodal decomposition inside the miscibility gap is maximum.

According to Cahn [10] when the conditions of spinodal are reached at low temperature the system tries to reduce its free energy by phase separation that is small in degree and large in extent. The resulting phase separated domains will have composition far away from equilibrium and interface that has a wide compositional gradient as compared to sharp compositional gradient that would be seen in phase separated regions by classical nucleation and growth. As seen in Fig. 5.10(a), the compositional gradient across the interface of small tertiary γ' is large. Even though γ' is enriched in Al and Ti and γ enriched in Cr and Co, the compositional gradient appears to be wide for all the elements. Mo shows no partitioning for these precipitates. This wide interface gives an indication that these regions phase separated by non classical nucleation. Comparing Cr and Al compositional partitioning across the primary and tertiary γ' precipitates (Fig. 5.10(b)) Al and Cr exhibit a very sharp interface for primary γ' whereas a much diffused interface exists for tertiary γ'. This is in agreement with the non classical nucleation theory by Cahn where interface would be diffused and the composition inside the precipitates would reach that of matrix for highly undercooled systems. A more detailed discussion of the results on phase separation in highly undercooled Rene88DT alloy is presented in the subsequent chapter which also suggests that phase separation occurs by spinodal decomposition at very low temperatures.

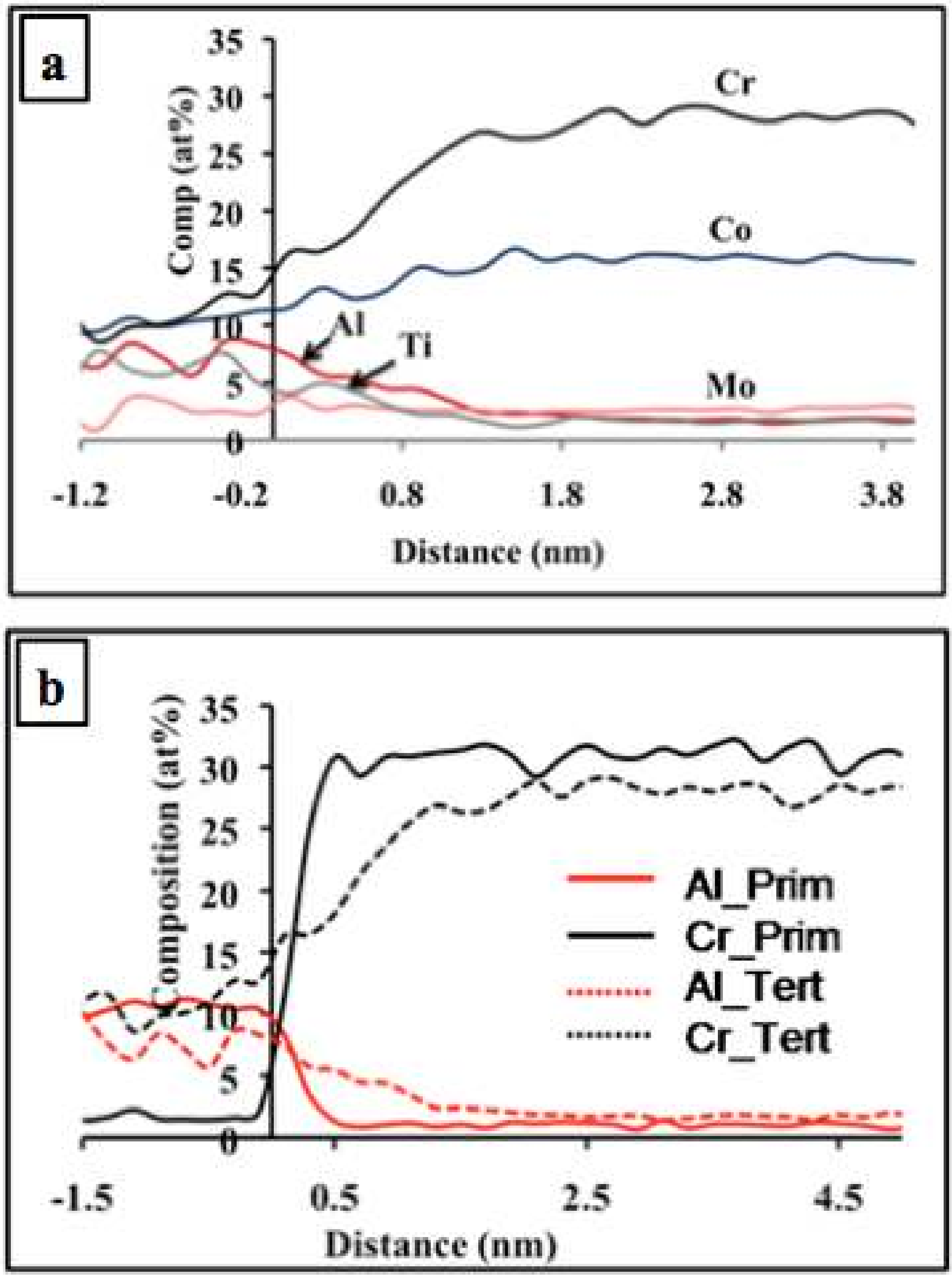

Figure 5.10. (a) Proxigram showing the composition profiles of Co, Ti, Cr, Al and Mo atoms across tertiary γ'/γ interface (b) Comparison of Al and Cr composition profile across the interface for primary and tertiary γ'

5.6 Formation Mechanism of Multiple Bursts of Nucleation

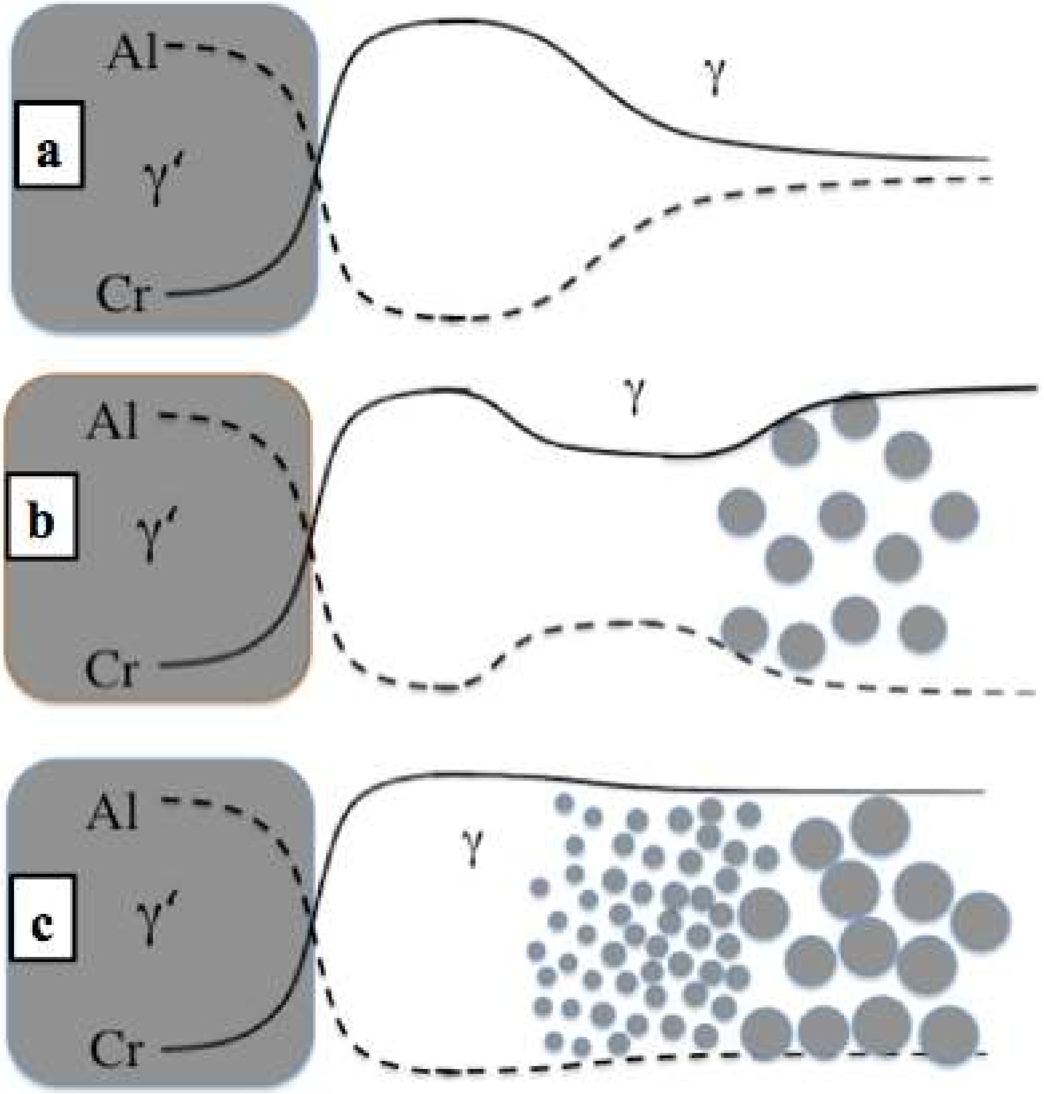

Figure 5.11. (a) Schematic showing (a) primary γʹ and composition profile ahead of γʹ formed at low undercooling, (b) Non-equilibrium composition in far γ and second nucleation burst (c) Composition profile and third nucleation burst at very high undercooling.

From the above results a schematic of the mechanism of different nucleation bursts can be explained. There are various factors facilitating the multiple bursts of nucleation during a continuous cooling experiment of Rene88DT. Due to continuous decrease in temperature there is a continuous increase in the thermodynamic driving force for nucleation. However, due to the growth of precipitates and depletion of γʹ forming elements in the matrix, the driving force for nucleation decreases. This driving force is however limited to the depletion zone which is formed due to the reduced mobility of solute with decreasing temperature and hence enrichment of solute away from the depletion zone away from the precipitates. These factors give rise to the complicated microstructure with different size distributions of γ′ and compositional variations. As seen in Fig. 5.11(a), the ordered primary γ′ forming at very high temperature under the γ′ solvus have low number density, which grow at very fast rates due to high diffusivities at high temperatures. The primary γ′ precipitates preferentially grow along <100> direction due to low elastic modulus along <100> and develop cuboidal morphology. The compositional profile across the γ′/γ interface (cube orientation) is sharp with high Al and low Cr in γ′. Across the interface the solute partitions quickly and reaches close to equilibrium concentration values over small distances in γ forming the depletion zone; however, these compositions slowly decay and reach non equilibrium compositions with supersaturation of solute over larger distances due to low number density of these precipitates. On further cooling the primary γ′ precipitates grow in size due growth and coarsening processes and develop cuboidal to irregular morphology. The depleted zone reaches equilibrium γ composition with increasing supersaturation of solute away from the depletion zone due to continuous decrease in diffusivity. Large thermodynamic driving force at low temperatures with supersaturation of solute away from the depletion zone causes second burst of nucleation of γ′ called secondary γ′ with much higher number density and increase in significant increase in γ′ volume fraction as shown in Fig. 5.11(b). Secondary γ′ forming at low temperatures grows at slower rates due to continuously decreasing diffusivity. Depletion of solute around the secondary γ′ with high number density results in overlapping of the diffusion fields and stops them for further growth. Hence, these precipitates maintain near to spherical morphology. These precipitates however remain undersaturated with solute and retain non-equilibrium compositions. The γ between the secondary γ′ quickly gets depleted in solute and hence very low driving force for any further nucleation between the secondary γ′ exists. However, between the secondary γ′ and the depleted zone the gradual increase in γ′ composition profile causes a non equilibrium composition of solute. However, sufficient thermodynamic driving force is not available there to cause any nucleation event until a really large undercooling is achieved. At this stage the reduced driving force to less solute is achieved by really high driving force due to very low temperatures. Very high driving force causes third burst of nucleation but slow kinetics and limited solute at this stage limit the growth of tertiary γ′. γ near secondary during secondary nucleation event is richer as compared to γ near primary and hence during third nucleation event due to slow cooling, the growth of tertiary γ′ is more for precipitates near the secondary causing a gradual increase in size distribution for tertiary γ′ from primary towards secondary. The nucleation of the third generation of γ′ seems to occur by spinodal decomposition with far from equilibrium composition and diffused interface with the matrix.

5.7 Summary

Coupling different characterization techniques – SEM, EFTEM and 3DAP, different generations of γ′ were identified and quantified. The results show that during continuously cooling, the interplay of thermodynamic driving force and kinetic factors results in the formation of three generations of γ′ precipitates which vary in composition. The γ composition is significantly different in the depletion region and near the tertiary γ′ which suggests that the mechanism leading to different generations of γ′ may be different. The interface of primary and tertiary γ′ being significantly different and latter being much diffused and the interconnected network of phase separated regions near the depletion zone indicate spinodal decomposition resulting in formation of γ′ at very high undercooling.

5.8 References

[1] S.S. Babu, M.K. Miller, D.A. Vitek, S.A. David, Acta Mater. 49 (2001) 4149

[2] P.M. Sarosi, B. Wang, J.P. Simmons, Y. Wang, M.J. Mills, Scripta Mater. 57 (2007) 767

[3] Y.H. Wen, J.P. Simmons, C. Shen, C. Woodword, Y. Wang, Acta Mater. 51 (2003) 1123

[4] Y.H. Wen, B. Wang, J.P. Simmons, Y. Wang, Acta Mater. 54 (2006) 2087

[5] R. Radis, M. Schaffer, M. Albu, G. Kothleitner, P. Polt, E. Kozeschnik, Acta Mater. 57 (2009) 5739

[6] S.T. Wlodek, M. Kelly, D.A. Alden, in: R.D. Kissinger, D.J. Deye, D.L. Anton, A.D. Cetel, M.V. Nathal, T.M. Pollock, D.A. Woodford (Eds.), Superalloys 1996, TMS, Warrendale, PA (1996) 129

[7] K. Thompson, D. Lawrence, D.J. Larson, J.D. Olson, T.F. Kelly, B. Gorman, Ultramicro. 107 (2007) 131

[8] J. Mayer, L. A. Giannuzzi, T. Kamino, J. Michael, MRS Bulletin. 32 (2007) 400

[9] P.M. Sarosi, G.B. Vishwanathan, D.D. Whitis, M.J. Mills, Ultramicro. 103 (2005) 83

[10] J.W. Cahn, J.E. Hilliard, J. Chem. Phys. 31 (1959) 688

CHAPTER 6

GROWTH OF DIFFERENT GENERATIONS OF γ' DURING AGING

6.1 Introduction

During continuous cooling of Rene88DT, multiple size scales of γ' precipitates are formed due to multiple nucleation events. The primary γ' precipitates that formed at low undercooling, grow and coarsening during cooling and develop cuboidal to irregular morphology. However, due to limited diffusion and continuous reduction in temperature, the secondary and tertiary γ' precipitates grow but do not coarsen and maintain non-equilibrium compositions. These results were presented in chapter 5 and it was concluded that three different generations of γ' exist past cooling of Rene88DT from 1150^{o}C. It has been shown in the literature that during growth and coarsening of precipitates the morphology of precipitates changes and may remain cuboidal or split depending on the strain contribution [1-5]. The researchers have also found that the coarsening of γ' precipitates may not be diffusion limited [6-14] but limited by the interface present between γ' and γ matrix [15]. This suggests that composition changes in the precipitate and matrix will significantly influence the growth and coarsening characteristics of the precipitates. Earlier studies of aging on Rene88DT were done by aging the slow cooled sample for 25 hours, 50 hours, 100 hours and 200 hours [16] and it was shown that the secondary γ' precipitates start coarsening beyond 25 hours of aging. Therefore, the initial stages of growth of precipitates were not captured. Hence, the present chapter discusses the aging effect on these different generations of γ' and addresses following issues;

(i) Change in morphology and distribution of primary γ' precipitates with aging; variation in size and morphology during aging of SC0 for 1 hour, 15 hour and 30 hours (SC1, SC10, SC15 respectively).

(ii) Changes in chemical partitioning between primary and tertiary γ′ and matrix during aging of SC0.

6.2 Experimental Procedure

The samples were supersolvus solution treated in a vacuum furnace at 1150°C in the single γ phase field for 30 minutes to dissolve any existing γ′ and then slow cooled at an average cooling rate of $24^{o}Cmin^{-1}$. These samples were subsequently aged for various periods of time at 760°C in a large chamber vacuum furnace and air quenched. For convenience, these samples will be subsequently referred to as SC1, SC10, and, SC15 samples in the remaining part of this chapter where the number past SC represents the number of minutes for which the samples were aged.

Samples for 3DAP tomography studies in the LEAP microscope were prepared by focused ion beam milling technique. For this purpose, samples were prepared by dual-beam focused ion beam (FIB) instrument (FEI Nova Nanolab 200) system using a Ga ion beam. The ion beam thinning was carried out in multiple steps, starting with 30kV ions and finally finishing with 5kV ions to reduce the surface damage caused by the higher energy ions [17, 18]. The final tip diameter of the atom probe specimens was ~ 50 – 80nm. The 3DAP experiments were carried out using a LEAP 3000 local electrode atom probe (LEAP™) system from Imago Scientific Instruments Inc. All atom probe experiments were carried out in the electric-field evaporation mode at a temperature of 70K, with the evaporation rate varying from 0.2 – 1.0% and the pulsing voltage at 20% of the steady-state applied voltage.

TEM samples were also prepared via conventional routes, consisting of mechanical grinding and polishing of 3mm diameter discs, followed by dimple grinding, and, final ion-beam milling to electron transparency. Ion beam milling was conducted on a Gatan Duo Mill and Fischione Model 1010 ion milling system, operated at 6kV. TEM analysis was conducted on a FEI Tecnai F20 field emission gun transmission electron microscope operating at 200kV. Images were obtained using the Cr M-edge in the energy filtered transmission electron microscopy (EFTEM) mode, as described elsewhere [19]. Representative regions were imaged at different magnifications to capture the relevant secondary and/or tertiary γ' precipitates in the alloy.

SEM analysis of primary γ' precipitates was done using immersion mode on etched samples. Prior to SEM analysis the samples were polished and etched using 15ml HCl + 10ml Glycerol + 5ml HNO_3. This light etching substantially enhanced the contrast between the γ and γ' phases in the immersion mode of the SEM.

6.3 Changes in Size, Distribution and Morphology of Primary γ′ During Growth

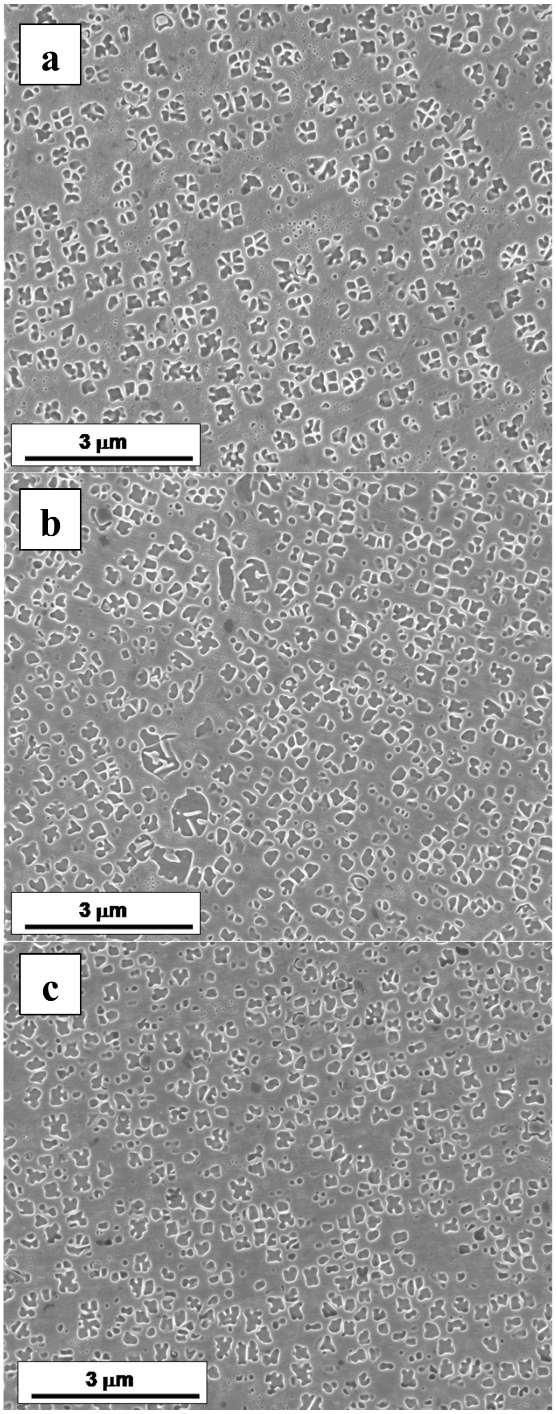

Figure 6.1. Secondary electron image of (a) SC1 (b) SC10 and (c) SC15 showing primary γ′ precipitates, in immersion mode of SEM.

During continuous cooling of Rene88DT the primary γ' precipitates formed at high temperature rapidly grow and coarsen and form cuboidal to irregular morphology as shown in previous chapters. However, when this material was aged past continuous cooling, change in morphology and sizes of the primary γ' precipitates was observed. As seen in Fig. 6.1(a) showing microstructure of SC1 sample, the primary precipitates appear to be mostly irregular shaped. A lot of precipitates appear to be in close proximity to each other giving an appearance of getting joined while other seem to have joined and formed irregular shaped precipitate. All these precipitates appear to be uniformly dispersed throughout the matrix in SC1. When material is aged for 10 hours, the morphology appears to be more cuboidal. Most of the small precipitates appear to have joined and formed larger precipitates as can be seen in Fig. 6.1(b). However, some small precipitates can still be seen close to the larger precipitates probably still in their coarsening stage. Compared to SC1, the number of smaller precipitates seems to have reduced in SC10. In addition, the number of precipitates that have cuboidal morphology seem to have increased in SC10. The cuboidal nature of precipitates seems to be most prominent in SC15 as seen in Fig. 6.1(c) and fewer number of very small γ' precipitates are visible. However, the difference between SC10 and SC15 precipitates is comparatively small as compared to SC1 and SC10. Also, precipitates that were in close proximity with each other giving an appearance of getting joined in SC1 seem to have disappeared in SC15 suggesting that coarsening of precipitates at short distances with each other is near completion after 15 hours of aging.

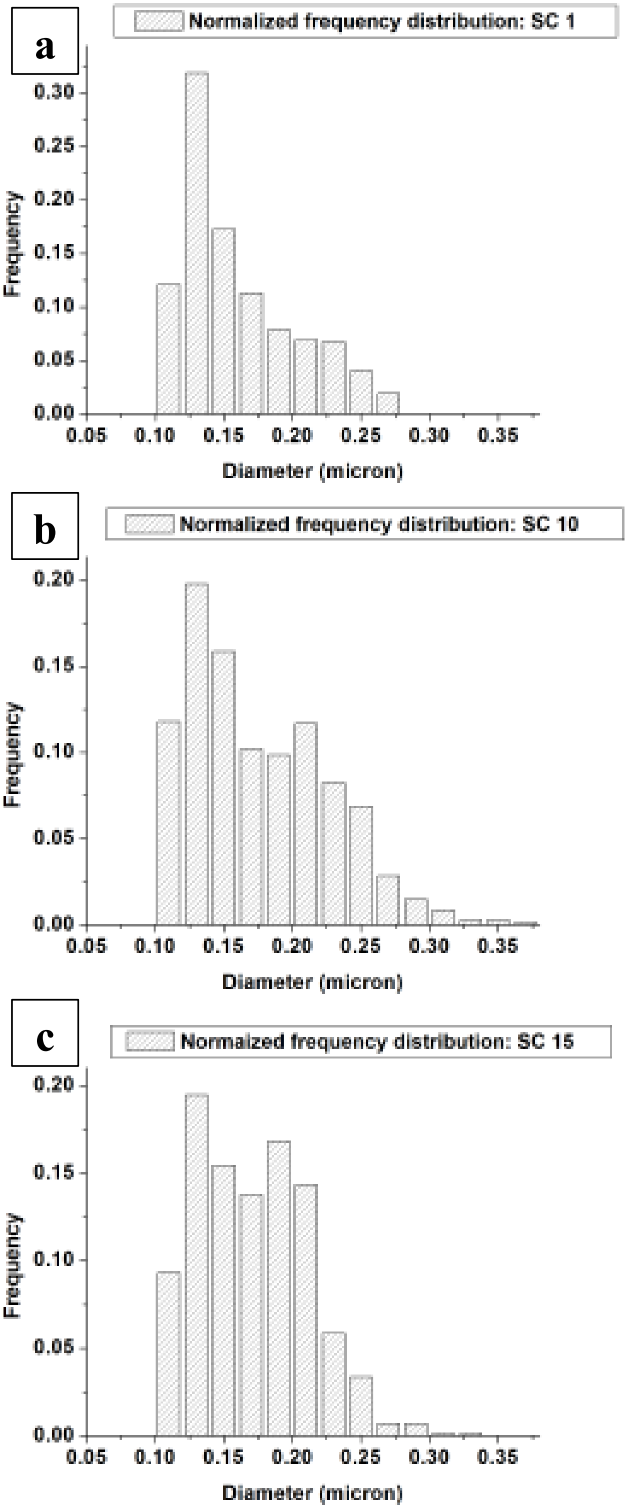

Figure 6.2. Normalized frequency size distributions for primary γ′ precipitates in (a) SC1 (b) SC10 and (c) SC15 condition.

A more statistical way of understanding the coarsening process of primary γ' precipitate was adopted by quantification of these precipitates sizes and observing their distribution. This was achieved by thresholding the SEM images using ImageJ software and calculating the area of the precipitates appearing black in white matrix. The individual area was then converted into equivalent diameter using $d = \sqrt{(4*A/\pi)}$ where A was the area of individual precipitate. The normalized frequency distribution for primary γ' precipitates was then plotted for each of the conditions as shown in Fig. 6.2(a), (b) and (c). The average size of primary γ' precipitates in SC1 was 161nm and standard deviation of 40nm but as seen in Fig. 6.2(a) the peak of the distribution is at 130nm suggesting that a significant number of precipitates are below the average size of the precipitates. These small precipitates large in number can be related to the precipitates that appeared to be in close proximity about to join and form one large precipitate. Upon aging for 10 hours (Fig. 6.2(b)), the average size of precipitates increased to 177nm with standard deviation of 50nm and an increase in number of precipitates in the range of 180nm to 300nm is seen. There is also reduction in number of primary γ' precipitates < 150nm in size. However, after 15 hours of aging (Fig. 6.2(c)), the average size if precipitates became 171nm with a standard deviation of 40nm which suggests that the average size of precipitate didn't not change after 10 hours of aging. The change in sizes is only minimal and within the standard deviation. The only difference can be observed is the change in morphology of the precipitates getting closer to cuboidal morphology. The spread in frequency distribution became narrower from 10 to 15 hours of aging resulting in decrease in standard deviation and precipitates get close to the average size.

6.4 Changes in Size, Distribution and Morphology of Secondary γ′ During Growth

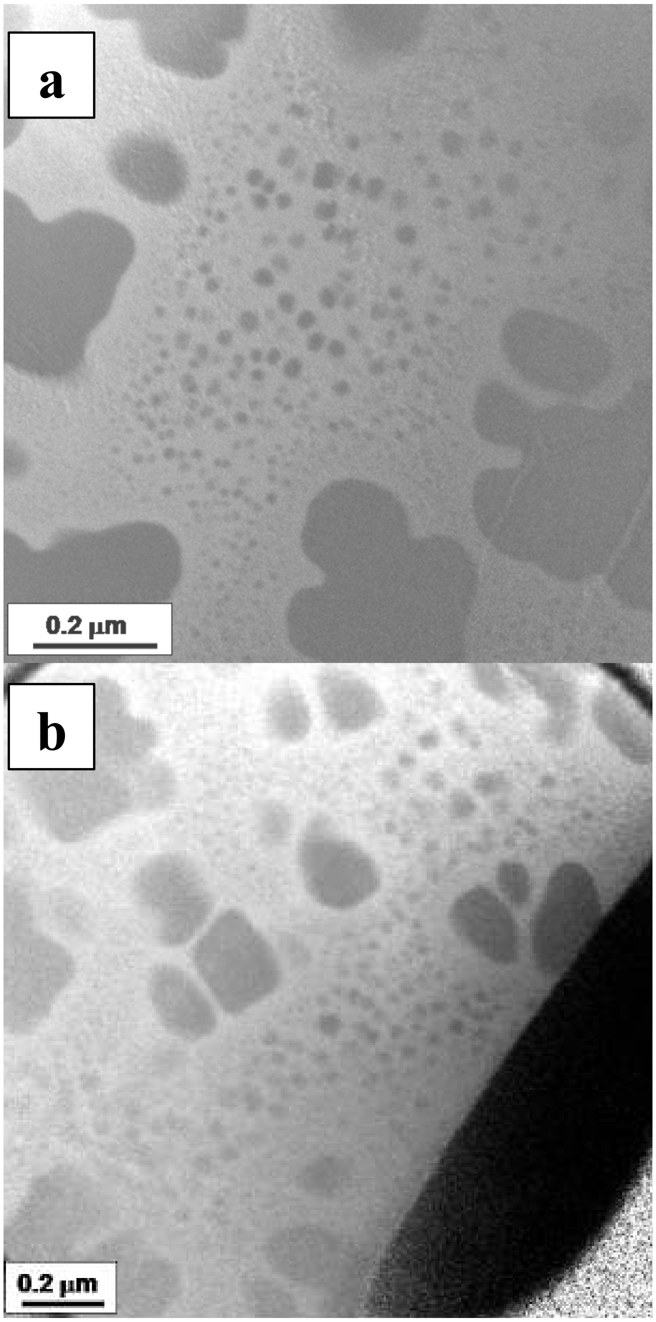

Figure 6.3. Energy-filtered transmission electron microscopy (EFTEM) images constructed using Cr M-edge in the EELS spectrum from solutionized, slow cooled and aged (a) SC1 sample showing primary, secondary and tertiary γ′ and (b) SC10 sample showing tertiary γ′ between secondary γ′ and depletion zone. The γ′ precipitates, which are Cr depleted, exhibit the darker grey contrast in these images.

The change in size, morphology and distribution was not just limited to primary γ' precipitates when the sample was aged past continuous cooling. As shown in previous chapter the tertiary γ' were barely visible by EFTEM. The sizes of the tertiary γ' precipitates were not quantifiable using EFTEM. As seen in Fig. 6.3(a), after aging for 1 hour the tertiary γ' precipitates are more clearly visible. This confirms that there indeed was a third generation of γ' precipitates formed during continuous cooling. The secondary γ' precipitate and the depletion region surround this third generation of precipitates. The secondary γ' precipitates have grown in size after 10 hours of aging, and the tertiary γ' precipitates have grown in size significantly as seen in Fig. 6.3(b). However, the tertiary γ' precipitates seem to remain unaffected by further aging (15 hours). This is probably due to the fact that matrix region closest tertiary γ' is depletion zone which is highly depleted in Al and Ti. This restricts the further growth of tertiary. As seen in Fig. 6.4(a) after aging for 15 hours the tertiary γ' grow and are visible in the EFTEM images. Very limited changes are seen in the size of primary γ' or the depleted zone around them. At higher magnification as seen in Fig. 6.4(b) these tertiary γ' are clearly visible which were not very clear in 1 hour aged sample. Even though the size of tertiary γ' is much more evident in SC15 sample, the true morphology and size of such small precipitates is difficult to determine due to the limitations of TEM. The depletion zone around the primary however remains uncharged during initial stages of growth of tertiary γ' which may change at later stages of growth and coarsening.

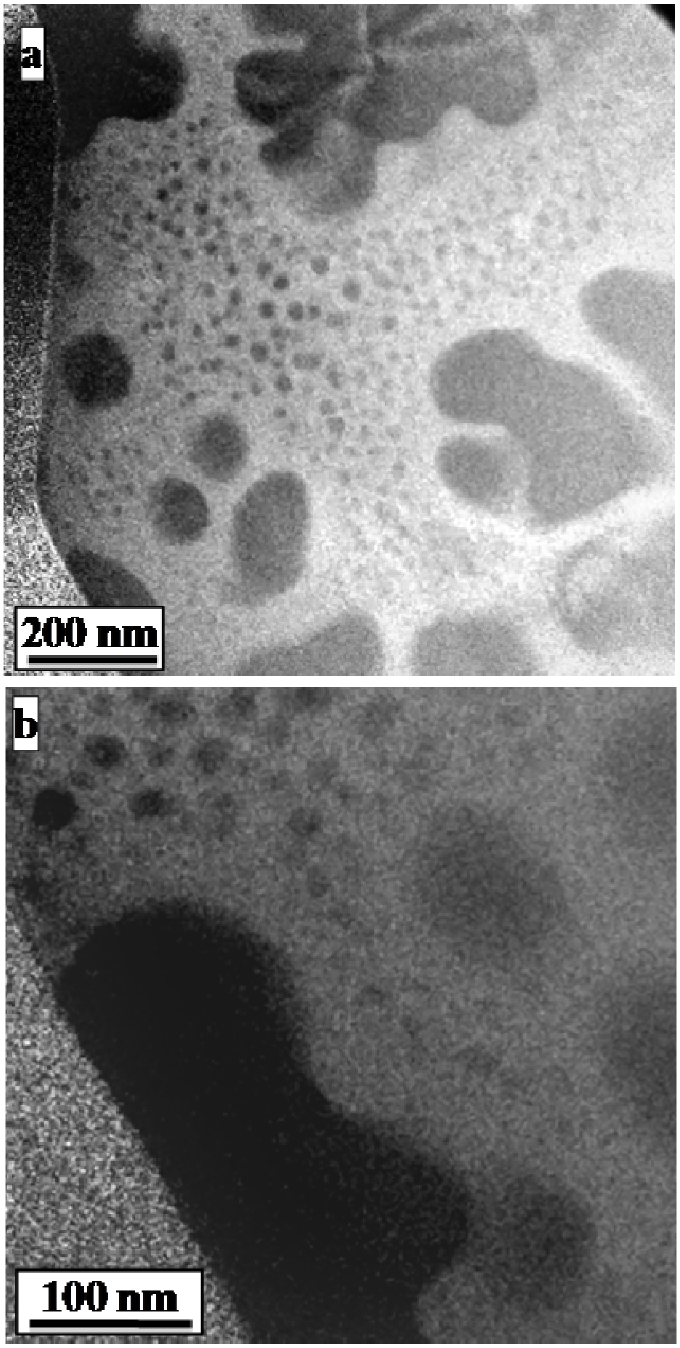

Figure 6.4. Energy-filtered transmission electron microscopy (EFTEM) images constructed using Cr M-edge in the EELS spectrum from solutionized, slow cooled and aged (a) SC15 sample showing primary, secondary and tertiary γ' and (b) SC15 sample showing grown small tertiary γ' between secondary γ' and depletion zone. The γ' precipitates, which are Cr depleted, exhibit the darker grey contrast in these images.

The change in size and distribution of secondary γ′ precipitates with aging time from 1 to 15 hours for slow cooled sample is shown in Fig. 6.5. The normalized frequency distribution clearly shows increase in number of precipitates in the size range 10 – 18nm whereas number of precipitates in the size range of 18 – 30nm, when aged from 1 to 15 hours, almost remains constant. Secondary γ′ precipitates in SC0 sample had an average size of 9nm which is comparatively less than secondary γ′ in SC1 sample which is 15nm; however, the average size of secondary γ′ precipitates is 17nm. This clearly shows that growth rate associated with small secondary γ′ precipitates, is high initially which becomes slower with time. It also complements the results shown by Tiley [16] that the increase in size of γ′ precipitates is dominated by growth upto 25 hours and coarsening after 25 hours past continuous cooling at 24^{o}Cmin^{-1}.

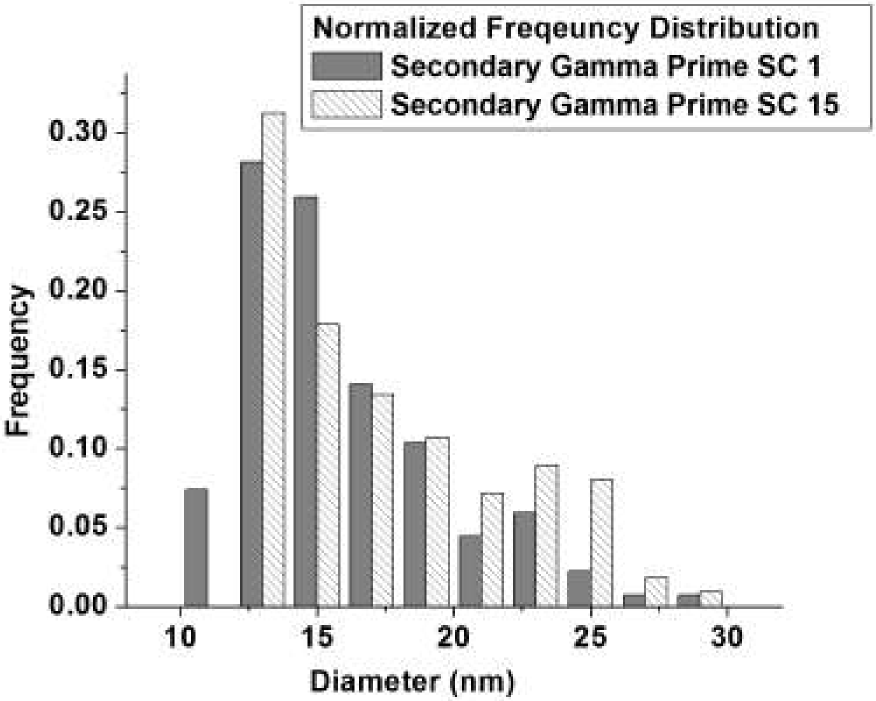

Figure 6.5. Normalized frequency size distribution of secondary γ′ precipitates in SC1 and SC15 condition showing increased size of secondary γ′.

6.5 Changes in γ' and γ Composition During Growth

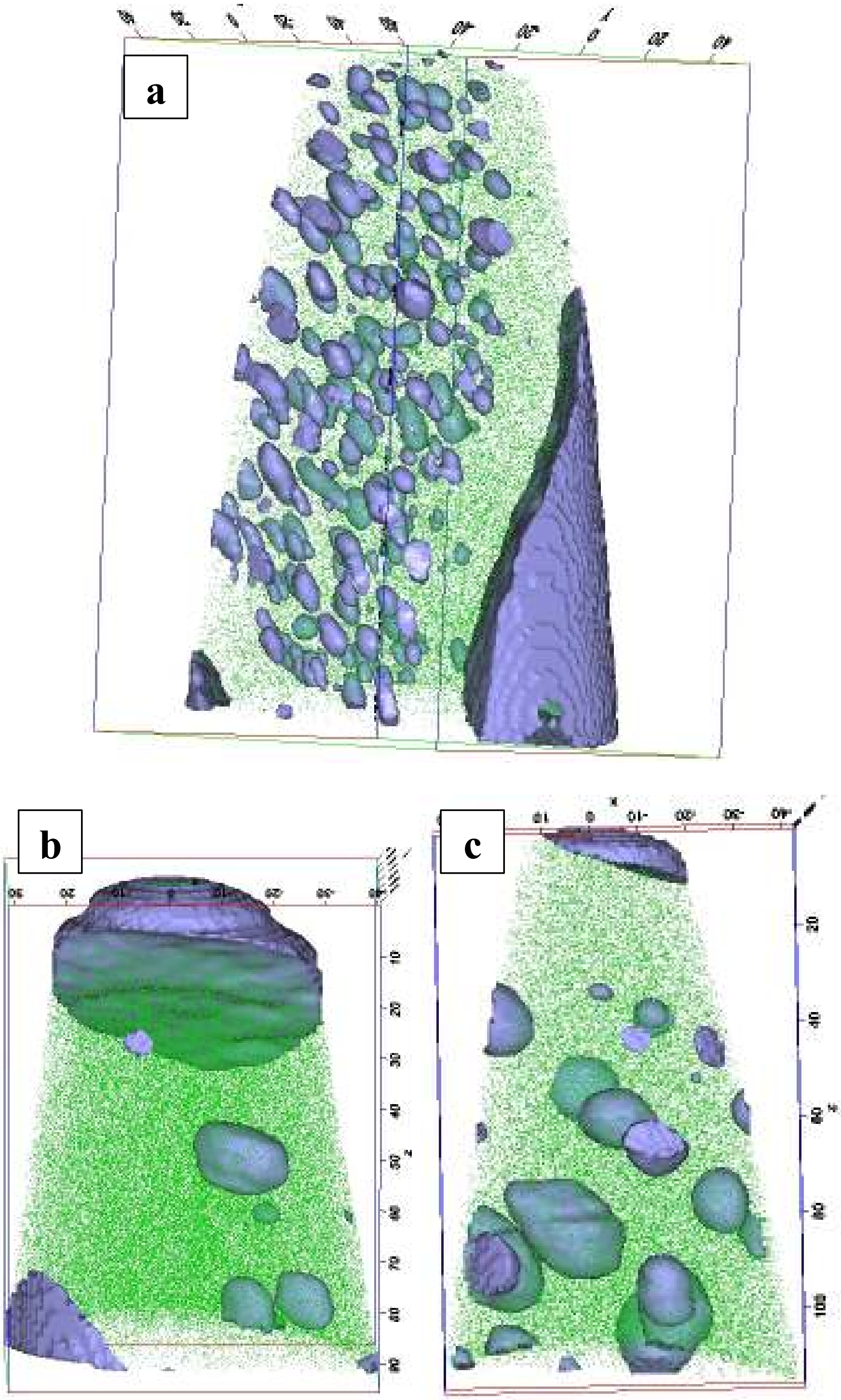

Figure 6.6. 3D atom probe reconstruction with Ni ions in green and γ' precipitates delineated by Cr = 14at% isosurface showing primary and tertiary γ' in (a) SC1, (b) SC10 and (c) SC15 condition.

Fig. 6.6(a) shows a 3D reconstruction of SC1 sample with Ni ions (green) and Cr = 14at% isosurface showing clearly γ′ precipitates. The reconstruction clearly shows primary γ′ and tertiary γ′ and depletion zone between them. The size scale of the bigger precipitate and a depletion zone besides provides a good evidence of it being primary γ′. The reconstruction clearly shows the depletion zone with no γ′. The thickness of the depletion zone (~15nm) is comparable to the thickness of depletion zone as seen in EFTEM images. The presence of smaller precipitates along the depletion zone and their size scale resembles the third generation of γ′ precipitates, also seen in EFTEM images earlier. The EFTEM due to its limitation is not a suitable technique for measuring such small precipitates; however, 3D atom probe analysis can give the true size and morphology of these precipitates as shown in Fig. 6.6(a). These precipitates range from 2 - 11nm in diameter with an average size of 4nm. This also confirms that this is indeed a third generation of precipitates nucleating after secondary which have an average size of 9nm and at much lower temperature. The precipitates closer to depletion zone look smaller as compared to ones away from the depletion zone which is due to minimal growth of these precipitates, since γ′ forming elements would be less closer to depleted zone. The tertiary γ′ also possess much higher number density as compared to primary or secondary γ′.

The tertiary γ′ grow to much larger dimensions after aging for 10 hours which can also be seen from 3-D atom probe reconstruction (Fig. 6.6(b)) of SC10 sample showing matrix rich in Ni with green dots and γ′ precipitates delineated using Cr = 14at% isosurface.. This reconstruction also clearly shows primary γ′, depletion region and tertiary γ′ grown in size. An atom probe reconstruction of SC15 is shown in Fig. 6.6(c) showing different regions; a section of primary γ′, depleted region and tertiary γ′. As seen in figure, these precipitate being closest to depletion zone have to size as much as 20nm in diameter; however, there are precipitates having smaller sizes, much smaller than the secondary γ' measured using EFTEM. This progressive increase in size of tertiary γ' precipitate away from the depletion zone is due to change in composition of the matrix away from the primary precipitate. As seen by the cylindrical compositional profile in Fig. 6.7(a), the composition of depleted region itself changes away from primary γ'. There is local enrichment of Cr and Co and depletion of Al and Ti which decays away from the precipitate matrix interface. This enrichment was more pronounced in SC0 condition, which probably decayed after aging for 1 hour. Therefore, extrapolation of this compositional profile would suggest that closer to depletion region the Al, Ti composition in the matrix would be less as compared to far away composition before third nucleation burst during continuous cooling. This would result in reduced growth of tertiary precipitates closer to depletion zone as compared to growth of precipitates away from depletion zone. After aging for 10 and 15 hours, the local enrichment of Cr and Co ceases in the depletion region and the compositional profile reaches a steady value close to equilibrium composition of the matrix as seen in Fig. 6.7(b) and (c).

Since all the precipitates do now grow equally, the smaller ones remain in non-equilibrium states even after aging for 15 hours. The composition of the tertiary γ' precipitate is different from primary even after 15 hours of aging as seen from the cylindrical profiles.

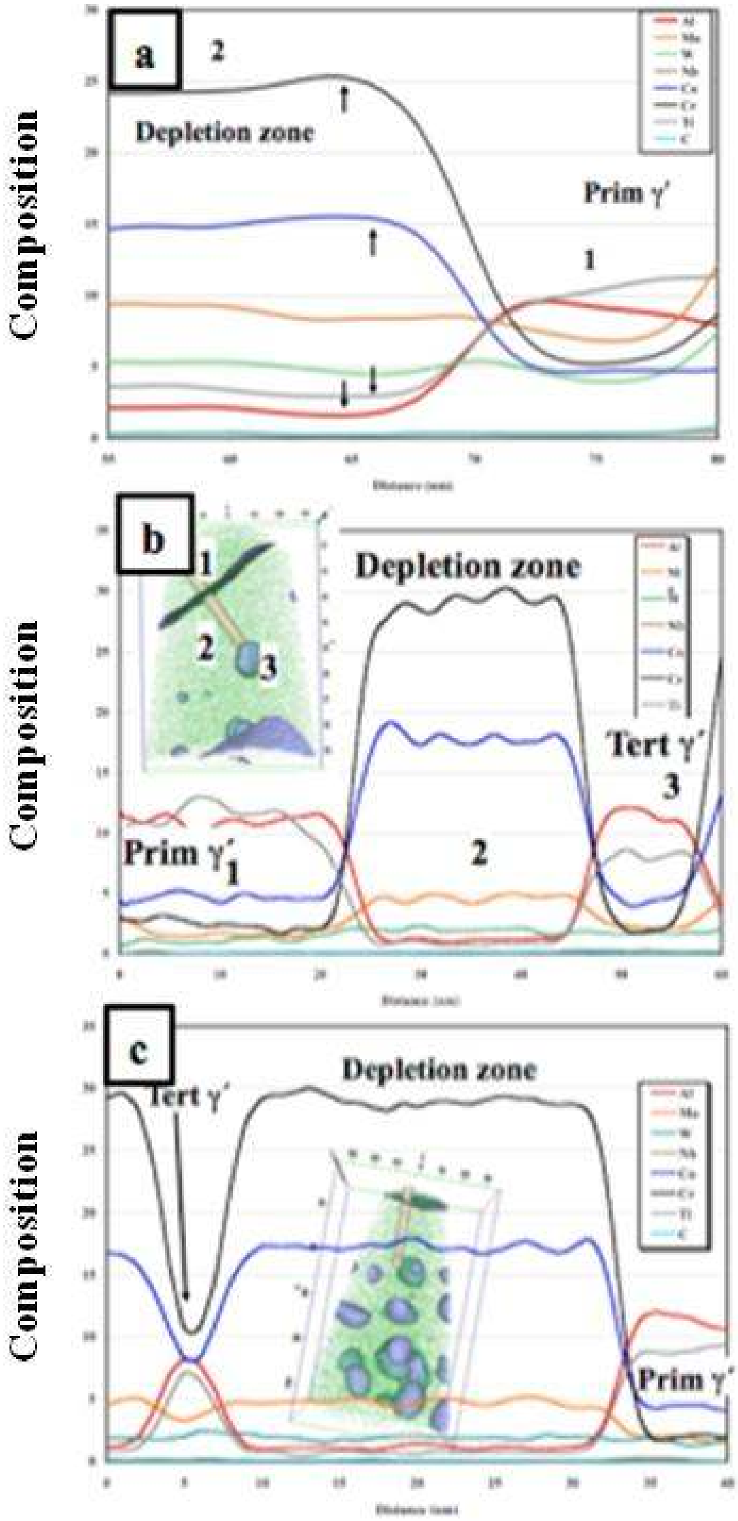

Figure 6.7. Compositional profile of Al, Ti, Co, Cr and Mo across primary γ′ and depletion zone in (a) SC1, (b) SC10 and (c) SC15 condition.

The variation in compositions of primary γ′, tertiary γ′ and the depletion zone with aging time was measured by inserting a 5nm diameter sphere in different regions. The primary γ′ composition after 1 hour of aging remains close to equilibrium composition highly enriched in Al and Ti and depleted in Cr and Co as shown in Table 6.1. The abnormal variation in the composition can be related to the fact that only a section of primary γ′ precipitate was present in the reconstruction. The cylindrical profiles clearly showed similar compositions of the primary γ′ precipitates for different aging times.

Table 6.1. Primary γ′ composition in SC1, SC10 and SC15 condition.

	Primary γ′ Composition (at %)					
Ion Type	**SC 1**	**SC 1 Error**	**SC 10**	**SC 10 Error**	**SC 15**	**SC 15 Error**
Al	9.3	0.1	11.2	0.3	12.3	0.7
Ti	8.8	0.1	11.8	0.3	8.9	0.6
Co	5.3	0.1	4.6	0.2	4.6	0.4
Cr	4.6	0.1	2.3	0.1	1.9	0.3

The variation in composition of tertiary γ′ is presented in Table 6.2. These results are more accurate since all the tertiary γ′ precipitates selected for compositional analysis were present inside the reconstruction volume. With aging time, the tertiary γ′ precipitates get enriched in Al (9.3 - 11.7at%) and Ti (8.8 - 9.2at%). They also get depleted in Cr and Co where Co composition changes from 5.3at% to 4.2at% and Cr changed from 4.6at% to 2.1at%. This shows that after 15 hours of aging the composition of the tertiary γ′ precipitates reaches close to equilibrium and therefore the growth of these precipitates would be minimal beyond 15 hours.

Table 6.2. Tertiary γ′ composition in SC1, SC10 and SC15 condition.

	Tertiary γ′ Composition (at %)					
Ion Type	**SC 1**	**SC 1 Error**	**SC 10**	**SC 10 Error**	**SC 15**	**SC 15 Error**
Al	9.3	0.1	12	0.3	11.7	0.3
Ti	8.8	0.1	8.5	0.2	9.2	0.3
Co	5.3	0.1	4.4	0.2	4.2	0.2
Cr	4.6	0.1	2	0.1	2.1	0.1

In addition to γ′ composition, the composition of the γ in depletion zone also reaches close to equilibrium after 15 hours. As seen in Table 6.3, the γ in depleted zone rejects more Al and Ti with aging, reducing their concentration from 1.8at% to 1.2at% and 2.4at% to 0.8at% respectively. Since primary γ′ precipitates are close to equilibrium composition prior to aging, the increase in Co and Cr and reduction of Al and Ti in depletion zone will be a result of diffusion of different element from neighboring tertiary γ′ precipitates. The Cr composition increases from 26at% to 28.3at% and Co increases from 15.7at%to 17.6at%. This gives direct evidence that after 15 hours of aging the growth of tertiary γ′ precipitates decay and further changes in size of tertiary γ′ precipitates would be dominated by coarsening.

Table 6.3. Depletion zone γ composition in SC1, SC10 and SC15 condition.

	γ in depletion zone composition (at %)					
Ion Type	**SC 1**	**SC 1 Error**	**SC 10**	**SC 10 Error**	**SC 15**	**SC 15 Error**
Al	1.8	0.1	1.2	0.1	1.2	0.1
Ti	2.4	0.1	0.8	0.1	0.8	0.1
Co	15.7	0.3	17.5	0.3	17.6	0.3
Cr	26	0.4	29.5	0.4	28.3	0.4

6.6 Summary

The results presented in this chapter give a direct evidence of coarsening of primary γ′ precipitates during aging up to 15 hours, after solutionized and cooled at $24^{o}Cmin^{-1}$. The secondary γ′ precipitates however are growth dominated. The composition of primary γ′ precipitates remain close to equilibrium composition and no effect of aging was noticed for these precipitates. However, tertiary γ′ precipitates that were barely seem in EFTEM past slow cooling in SC0 grew after 1 hour of aging and seemed to grow at a rapid rate until 15 hours of aging. The tertiary γ′ composition starts from non equilibrium condition and steadily progress towards equilibrium with aging. However, very small difference was seen in size and composition between SC10 and SC15 samples. Therefore, in aging up to 15 hours the microstructural changes are dominated by growth of secondary and tertiary γ′ precipitates and coarsening of primary γ′ precipitates.

6.7 References

[1] R.A. Ricks, A.J. Porter, R.C. Ecob, Acta Metall. 31 (1983) 43

[2] M. Doi, T. Miyazaki, T. Wakatsuki, Mater. Sci. Eng. 67 (1984) 247

[3] A.G. Kachaturyan, S.V. Semenovskaya, J.W. Morris, Acta Metall. 36 (1988) 1563

[4] T. Miyazaki, M. Imamura, T. Kozaki, Mater. Sci. Eng. 54 (1982) 9

[5] A. Hazotte, T. Grosdidier, S. Denis, Scripta Mater. 34 (1996) 601

[6] I.M. Lifshitz, V.V. Slyozov, J. Phys. Chem. Sol. 19 (1961) 35

[7] C.Z. Wagner, Elektrochem. 65 (1961) 581

[8] A.J. Ardell, Acta Metall. 20 (1972) 61

[9] C.K.L. Davies, P. Nash, R.N. Stevens, Acta Metall. 28 (1980) 179

[10] A.D. Brailsford, P. Wynblatt, Acta Metall. 27 (1979) 489

[11] P.W. Voorhees, M.E. Glicksman, Acta Metall. 32 (1984) 2001

[12] N. Akaiwa, P.W. Voorhees, Phs. Rev. E. 49 (1994) 3860

[13] J.A. Marqusee, J.J. Ross. Chem. Phys. 80 (1984) 536

[14] M. Tokuyama, K. Kawasaki, Physica A. 123 (1984) 386

[15] A.J. Ardell, V. Ozolins, Nat. Mater. 4 (2005) 309

[16] J. Tiley, G.B. Viswanathan, R. Srinivasan, R. Banerjee, D.M. Dimiduk, H.L. Fraser, Acta Mater. 57 (2009) 2538

[17] K. Thompson, D. Lawrence, D.J. Larson, J.D. Olson, T.F. Kelly, B. Gorman, Ultramicro. 107 (2007) 131

[18] J. Mayer, L.A. Giannuzzi, T. Kamino, J. Michael, MRS Bull. 32 (2007) 400

[19] P.M. Sarosi, G.B. Vishwanathan, D.D. Whitis, M.J. Mills, Ultramicro. 103 (2005) 83

CHAPTER 7

DECOMPOSITION PATHWAY INVOLVING ORDER-DISORDER TRANSFORMATION AND PHASE SEPARATION

7.1 Introduction

Concurrent chemical clustering and ordering processes occurring within the same supersaturated solid solution comprise an interesting class of solid-solid phase transformations that can often lead to a homogeneous distribution of nanoscale ordered precipitates within a disordered solid solution matrix [1-3] often resulting in enhanced mechanical properties such as high temperature strength. Typically, these two processes are considered mutually exclusive since chemical clustering involves a preference towards formation of bonds between like atoms, leading to compositional partitioning within the metallic solid solution, while ordering involves a preference towards the formation of bonds between unlike atoms leading to an ordered structure. When a disordered solid solution is rapidly cooled (or quenched) from a single phase field to a temperature corresponding to a two-phase field, the resulting highly undercooled and supersaturated disordered solid solution is often unstable (or metastable) with respect to both clustering and ordering processes [3]. There are a number of examples in the literature that discuss the possibility of such concurrent clustering and ordering processes in metallic solid solutions including Fe-Al [4], Ni-Al [5,6], Ni-Ti [7,8], and Cu-Ti [9,10]. While the order-disorder reaction in Fe-Al is a second (or higher) order reaction, in case of Ni-Al and Ni-Ti alloys the ordering involves a first-order reaction. Furthermore, there has been a substantial amount of controversy in the literature regarding whether the spinodal clustering (or phase separation) precedes or is subsequent to the ordering reaction. In most cases, reports indicate that the chemical ordering precedes the spinodal decomposition since the ordering process involves short-range atomic jumps which are relatively easy to accomplish and hence take place faster compared with the longer range diffusion required for spinodal decomposition [1-3, 11]. A few exceptions to this include the reports in Ni-Ti [6, 7] and more recently in the Cu-Ni-Sn [11] systems, where spinodal decomposition has not only been reported to precede but also has been a prerequisite for the ordering reaction to take place. The proposition is that since the Cu-15Ni-8Sn alloy composition cannot undergo congruent ordering, spinodal decomposition creates Sn-rich domains within which DO_{22} (and subsequently $L1_2$) ordering can take place [12]. Despite these interesting experimental observations, in almost all these cases the evidence indicating concurrent spinodal decomposition and ordering is based primarily on diffraction (electron or x-ray) data as well as diffraction contrast images recorded in a transmission electron microscope. Direct observation of the early stages of concurrent (or sequential) spinodal decomposition and ordering processes is simply not possible using these particular techniques. Recent developments in aberration-corrected scanning transmission electron microscopy (STEM) and complementary technique such as atom probe tomography (APT) now permit the visualization of these complex solid-state transformations at their very early stage. Therefore, this chapter focuses on capturing and directly imaging these complementary processes of spinodal decomposition and chemical ordering at atomic resolution as well as measuring the resultant compositional partitioning at very early stages of the transformation.

In the case of formation of the γ', Ni_3Al-based ($L1_2$ ordered) phase within the disordered face-centered cubic (fcc) γ solid-solution matrix of nickel base alloys containing Al and other alloying additions, there has been some controversy in the literature regarding the precipitation mechanism. Thus, while a number of reports clearly classify γ' precipitation in the γ matrix as a classical nucleation and growth process [12, 13], there are others which have claimed spinodal behavior [14, 15]. For example, Hill and Ralph [14] suggested that the precipitation process may involve spinodal decomposition, based on results of atom probe field-ion microscopy (APFIM) studies of Ni-Al alloys. Interestingly, there are issues regarding this interpretation of their results. For example, Wendt and Hassan noted from [14] that in samples of the quenched alloy that have been briefly aged (30 minutes at 898K) the composition of the Al-rich regions (~5nm) was Ni-25at%Al, i.e. the stoichiometric γ' composition, implying that the phase separation was complete. Actually, it was reported in [14] that the composition of Al-rich regions in the as-quenched alloy also corresponds to stoichiometry. Based on this argument, it was claimed [13] that the precipitation process involved a classical nucleation and growth mechanism. Because of these conflicting views, it is clear that the γ' precipitation mechanisms are not known. This study reports novel results which permit identification of these mechanisms of γ' precipitation in highly undercooled samples of a nickel base superalloy by coupling aberration-corrected STEM with APT investigations.

7.2 Experimental procedure

Experiments were carried out on the commercial Ni base superalloy alloy, Rene88DT [16]. In order to obtain the highest possible cooling rates, thin sections of the alloy (< 2mm) were solution treated in the single γ phase-field at 1150°C for 60 minutes in vacuum followed by a very rapid quench in ice-water that was kept in an inert Ar atmosphere. The purpose of the very rapid quench was to arrest or capture the formation of the ordered γ' precipitates at the earliest stage. Following quenching, the samples were aged at 760^{o}C for 1, 5, 30 and 60min. Samples for transmission electron microcopy (TEM) studies were prepared by extracting a thin foil by the focused ion beam method (FIB), followed by low energy Ar ion milling on Fischione Model

1040 nano-mill system. Atomic resolution, Z(atomic mass)-contrast imaging was carried out in the High Angle Annular Dark Field (HAADF)-STEM mode on an FEI Titan 80 – 300kV microscope, operated at 300 kV, equipped with a CEOS probe aberration corrector. Nanometer-scale compositional analysis of the same samples was carried out using APT in a local electrode atom probe system (Cameca's LEAP™). Samples for atom probe analysis were prepared in a dual-beam FIB as per details discussed elsewhere [17]. All atom probe experiments were carried out in the laser pulse evaporation mode at a temperature of 50K using a pulse energy of 0.2nJ and a pulse frequency of 200kHz.

7.3 Investigation of Early Stages of Decomposition leading to γ′ Formation

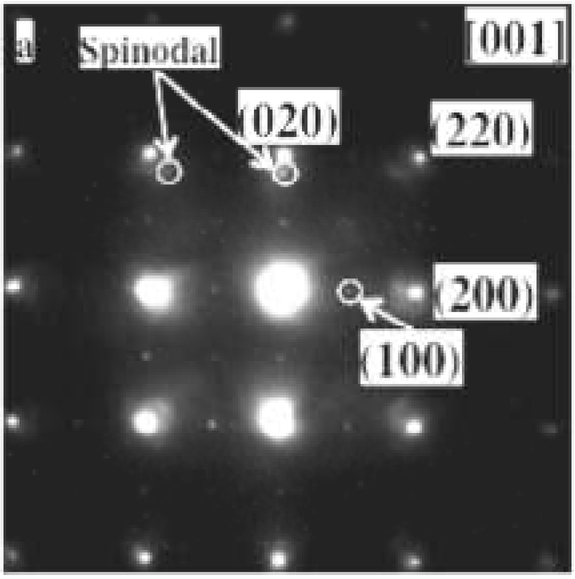

Figure 7.1. Selected area diffraction pattern of EWQ sample along <001> showing 4-fold symmetry, ordered spots and satellite reflections.

Fig. 7.1 shows a selected area electron diffraction (SAD) pattern from the as-quenched Rene88DT Ni-base superalloy sample recorded along the [001] zone axis of the fcc γ matrix. The SAD pattern shows 4-fold symmetry γ along the [001] zone. The {200} show a variation in intensity possibly due to slight deviation from the zone; however, this deviation is not significant as the 4-fold symmetry of the higher order planes is still visible ({400} planes). In addition to the fundamental {200} and {220} reflections (or intensity maxima) from the fcc γ matrix, there are additional weak superlattice reflections clearly visible at the {100} and {110} locations, indicating the presence of $L1_2$ ordering within the γ matrix. Additionally, satellite reflections are present near the fundamental matrix reflections. Two such reflections have been marked in Fig. 7.1 and their presence is indicative of phase separation (or compositional clustering) consistent with previous observations of spinodal decomposition [11, 18]. Hence, these satellite reflections have been labeled "spinodal" in the diffraction pattern. These satellite intensity maxima correspond to a modulation wavelength of ~ 2nm. The diffused satellite reflections also suggest that this compositional modulation is not present along a particular direction. It has been reported in the past that the compositional modulation may exist along <001> direction when the lattice mismatch is significant [12]. This is also consistent with our observation as the lattice mismatch between γ and γ' is not significant. Therefore the collective diffraction evidence (i.e., superlattice and satellite reflections) is consistent with the co-existence of spinodal decomposition and chemical ordering within the fcc matrix.

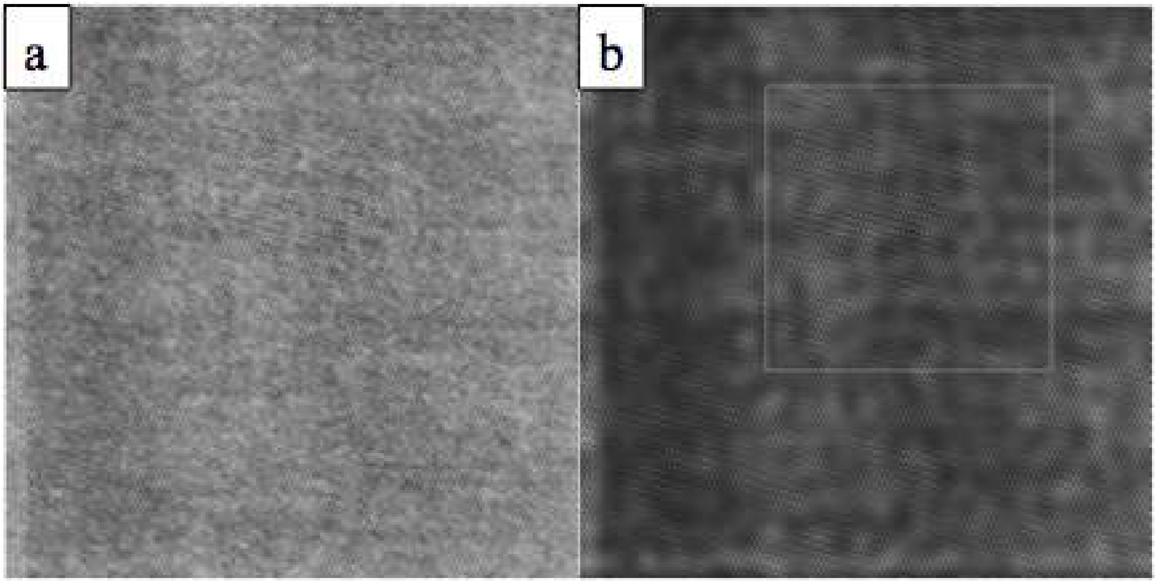

Figure 7.2. (a) RAW HAADF-STEM image of EWQ taken along <011> zone, (b) Background subtracted same HAADF-STEM image.

To understand the microstructural evolution at atomistic length scaled high angle annular dark field (HAADF) STEM imaging was done. High-resolution Z-contrast imaging, carried out in HAADF-STEM mode in an aberration-corrected electron microscope, revealed atomic scale information regarding the nature of these ordered regions as shown in Figs. 7.2(a) and (b). Fig. 7.2(a) shows the raw HAADF-STEM image recorded with the electron beam parallel to the [011] zone axis of the γ matrix. It clearly shows some ordered regions corresponding to γ′ phase; however, due to the presence of background noise in the image the Z contrast and ordering information in the micrograph is abased. Fig. 7.2(b) shows the filtered (i.e., background-subtracted) image which provides for improved contrast and enhanced image clarity. The contrast visible in these HAADF-STEM can be correlated directly to Z-contrast or atomic mass contrast, where brighter regions have a higher concentration of heavier solute elements (e.g. Co, Cr, W, Nb) while regions of darker contrast are likely to contain higher concentrations of lighter elements (e.g. Al, Ti). Interestingly, these regions of brighter and darker contrast, visible in the

HAADF-STEM images appear to be interconnected, a feature characteristic of a spinodally-decomposed microstructure [20]. Due to low magnification of the image it is difficult to identify the ordered regions. However, from contrast difference (bright and dark regions) the occurrence of phase separation in the material can be justified.

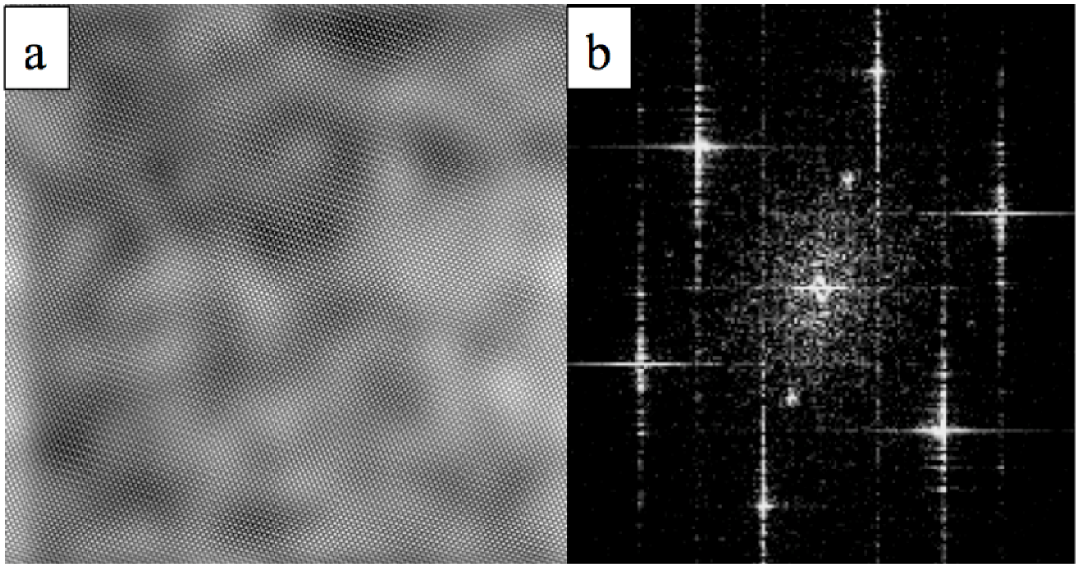

Figure 7.3. (a) Section of filtered HAADF-STEM image showing Z contrast and interconnected nature and ordered regions, (b) Fast Fourier Transform of the same image.

An enlarged view of a cropped area from Fig 7.2(b) is shown in Fig. 7.3(a) and can be assumed to be representative of whole sample. This micrograph clearly shows the phase separated regions and ordering in some regions. The darker regions exhibit an interconnected morphology indicating phase separation by spinodal decomposition resulting in darker and brighter regions with different average atomic contrast. Similar conclusions can be drawn for the differences in contrast between individual atomic columns in these HAADF-STEM images, with the brighter columns belonging to the Ni sublattice in the Ni_3Al-based $L1_2$ ordered structure, while the darker atomic columns belong to the Al sublattice. Closer inspection of these regions shows the presence of an ordered structure within these regions with rows of brighter atomic columns (Ni sublattice) alternating with rows containing 50% brighter (Ni sublattice) and 50% darker (Al sublattice) atomic columns. This pattern is consistent with an $L1_2$ ordered structure viewed along the [011] axis. $L1_2$ ordering is also confirmed by the presence of {100} and {110} spatial frequencies in the Fourier transform of the HAADF-STEM image shown in Fig. 7.3(b). Based on the HAADF-HRSTEM analysis, the ordered domains nominally lie in the size range of 3 – 6nm. In contrast, the nanometer-scale brighter regions in the HAADF-STEM images shown in Fig 7.3(a), do not appear to exhibit the periodic arrangement of brighter and darker atomic columns, but rather all the atomic columns within the brighter regions appear to be nominally of the same contrast indicating a random solid solution. A more detailed analysis of the ordering and disordering in various regions will be presented subsequently in this letter.

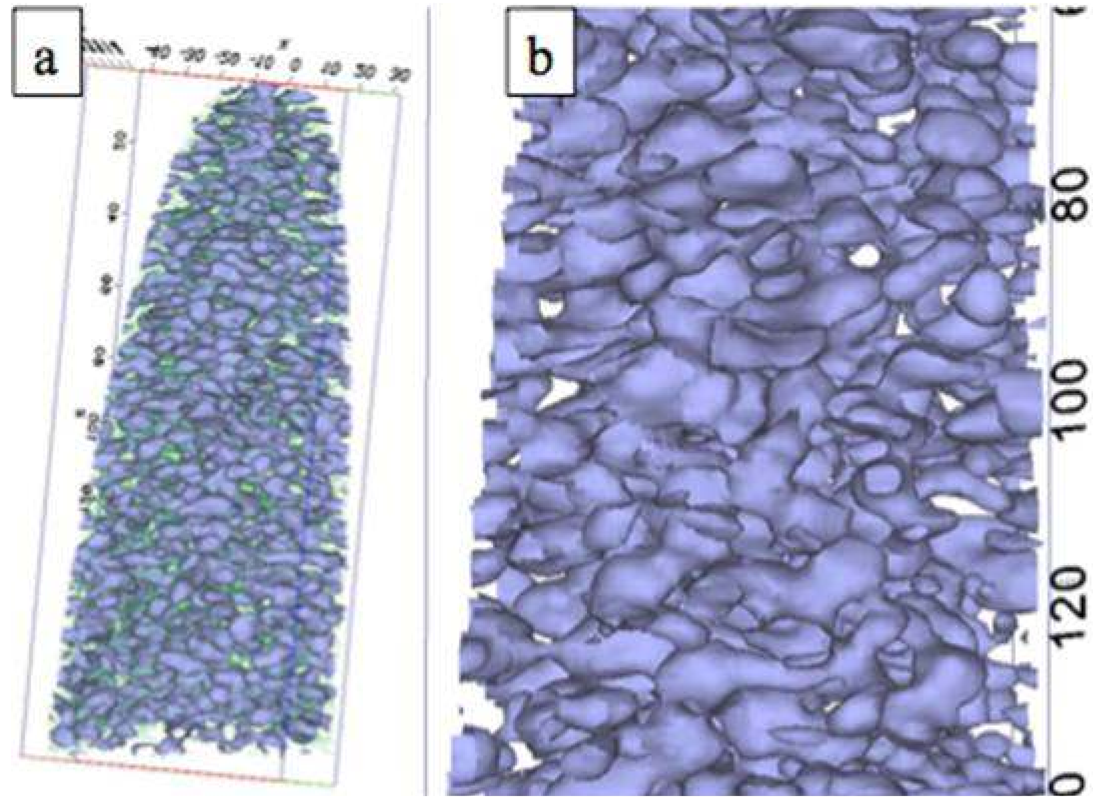

Figure 7.4. (a) 3DAP reconstruction of EWQ sample with Ni ions in green and Cr = 18at% isosurface, (b) enlarged section of same reconstruction showing interconnected morphology.

Even though the HAADF-STEM analysis showed the Z contrast corresponding to phase separation, to confirm the results obtained by TEM, atom probe investigations were performed to complement these results. 3D reconstruction (70nm x 70nm x 180nm) of the atom probe data recorded from the rapidly cooled sample is shown in Fig. 7.4(a). Since previous studies on the same Ni base superalloy [21] indicate that Cr is the most strongly partitioning element between the γ and γ′ phases in this alloy, the Cr-rich and Cr-depleted regions have been clearly delineated by plotting a Cr = 18at% iso-concentration surface (or isosurface) in Fig. 7.4(a). Thus, the regions within this Cr isosurface (encompassed by concave interfaces) contain less than 18%Cr while the regions outside the isosurface contain higher amounts of Cr. A section of a 3D tomographical reconstruction is shown in Fig. 7.4(b). This 3D reconstruction reveals several interesting aspects of the microstructure. Firstly, despite the rapid quench rate experienced by this sample, there is significant partitioning of Cr at the nanoscale. Secondly, the Cr-enriched and Cr-depleted regions are interconnected as would be expected in case of a spinodally decomposed microstructure. These results complement the results obtained by HAADF-STEM that phase separation occurred at the atomic length scales and there is no particular direction in which the phase separation occurs. In other words the compositional modulation is not associated only with elastically soft direction <100> possibly due to small lattice mismatch between equilibrium γ′ and γ. In addition, during the initial stages of spinodal decomposition, since the partitioning of elements is minimal, the resulting lattice mismatch between γ′ and γ phase would also be negligible.

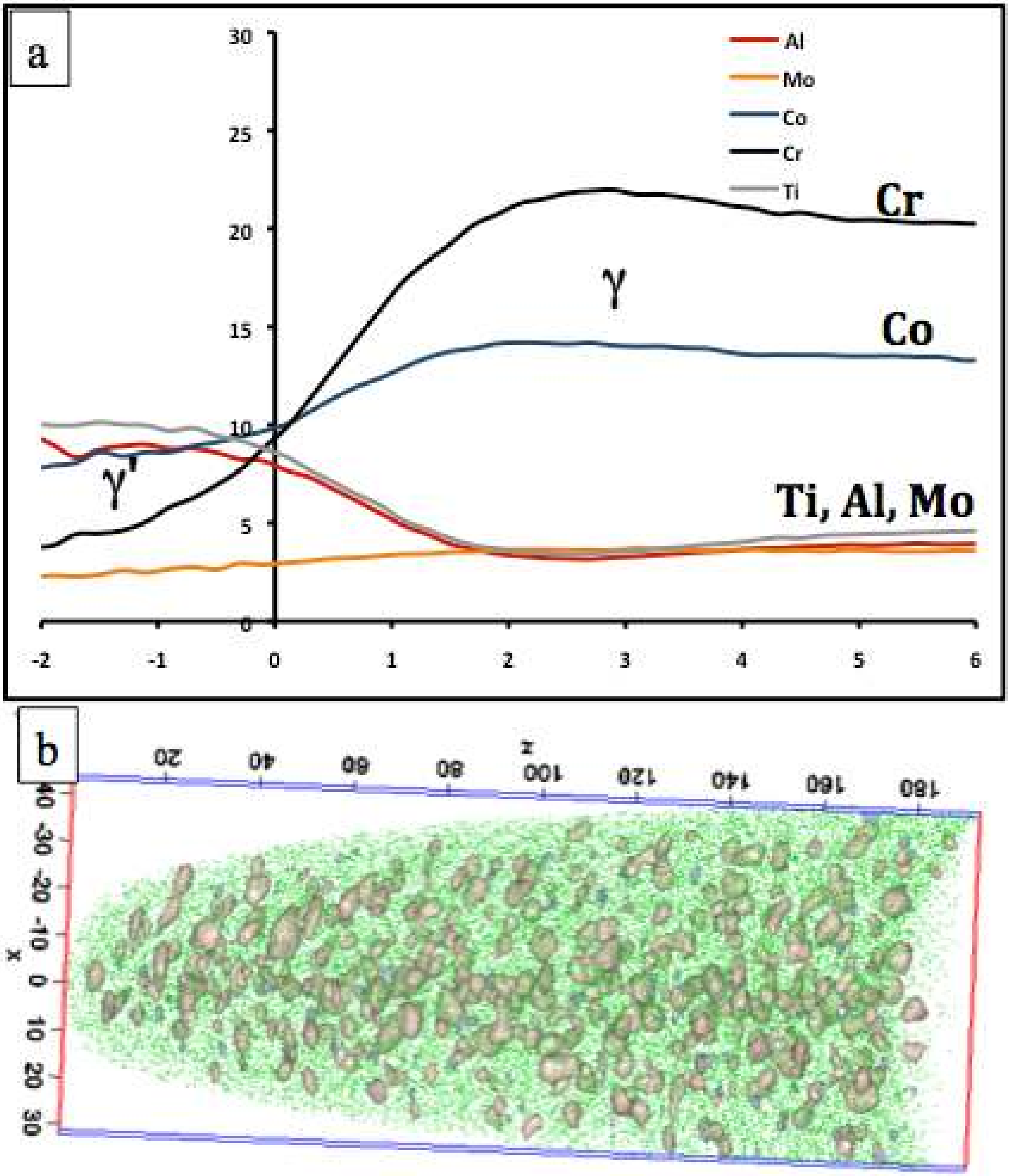

Figure 7.5. (a) Proximity histogram of Al, Ti, Cr, Co and Mo of Cr = 14at% isosurface, (b) 3DAP reconstruction of EWQ sample with Ni ions in green and Cr = 14at% isosurface.

Fig. 7.52(a) shows a proximity histogram analysis for the Cr = 14at% isosurface. Composition profiles for the primary solute elements in this Ni-base alloy, Cr, Co, Ti, Al, and Mo, across the interface defined by the isosurface, have been plotted in this figure. While there is partitioning of the solute elements across the interface, the compositional gradient is rather diffuse for all these elements with an interface width ~ 4nm (for Cr, Ti, and Al). Such a diffuse compositional gradient is consistent with the early stages of a spinodally-decomposed microstructure with compositional modulations of small amplitude present throughout the matrix [20] leading to local nanometer scale domains enriched in Al and Ti while being depleted in Co, Cr, and Mo. Apart from a compositionally diffuse interface, the γ' composition doesn't reach a steady state and therefore can be concluded that these regions are still in their early stages of elemental partitioning. As compared to primary γ' the composition near to the interface also doesn't reach near to equilibrium which also alludes to similar conclusion. Based on the HAADF-STEM images (Fig. 7.2(b)) it appears that the $L1_2$ ordered domains are discrete and lie in the size range of 3 – 6nm. Therefore, the Cr = 18at% isosurface, exhibiting an interconnected network, possibly does not delineate the γ' domains. Previous results indicate that the γ' phase can be best delineated using a Cr = 14at% isosurface for this alloy [21, 22]. Using a similar analogy in the present study, constructing a Cr = 14at% isosurface (Fig. 2(c)) results in Cr-depleted domains in the range of 3 - 8nm, which is in good agreement with the HAADF-STEM results (Fig. 7.2(b) and 7.3(a)). The average composition of these Cr-depleted ordered regions was determined to be Ni-9.1Co-6.9Cr-8.5Al-9.4Ti-2.7Mo (all in at%). The composition of these ordered domains is substantially different from the near-equilibrium composition of larger γ' precipitates (Ni-6.5Co-1.7Cr-12.3Al-9.2Ti-2.9Mo, all in at%) reported in previous atom probe studies of the same alloy after long-term aging at 760°C [22]. The substantially higher concentration of Co and Cr and a lower concentration of Al within the γ' precipitates in the rapidly quenched alloy are indicative of ordering taking place at far-from equilibrium compositions.

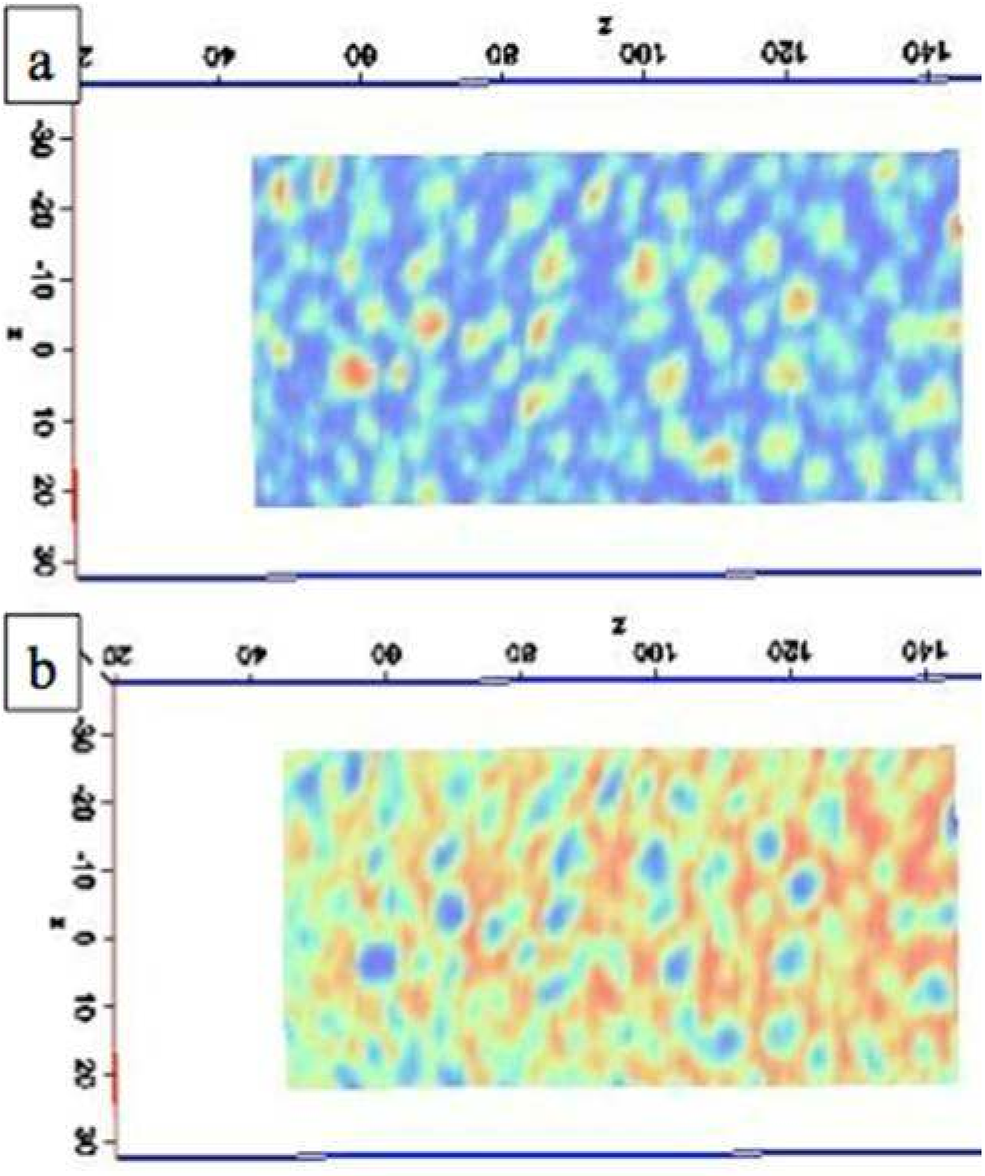

Figure 7.6. 2-D compositional map showing (a) Al rich (red) and Al depleted regions (blue), (b) Cr rich (blue) and AL depleted regions (red) regions.

The ordered γ' regions being smaller than the phase separated regions can also be seen using a 2-D concentration map of Al and Cr from atom probe reconstruction. A section 40nm x 5nm x 150nm was chosen with major axis along the Z direction as shown in Fig. 7.6(a) and (b). Fig. 7.6(a) shows a 2-D concentration map of Al directly revealing a compositionally modulated structure with red regions representing very high Al concentration and dark blue indicting regions of low Al content. This image also gives an indication that there is interconnected network of phase separated regions and very few regions that have very high Al content are isolated (possibly ordered). This is analogous to the HAADF-STEM image which also showed a compositionally modulated and interconnected network of dark areas and some regions being ordered. The red regions are also of the same size scale as the ordered ones in HAADF-STEM micrograph. Similar 2-D compositional map of Cr is shown in Fig. 7.6(b) for Cr which also complements to these results.

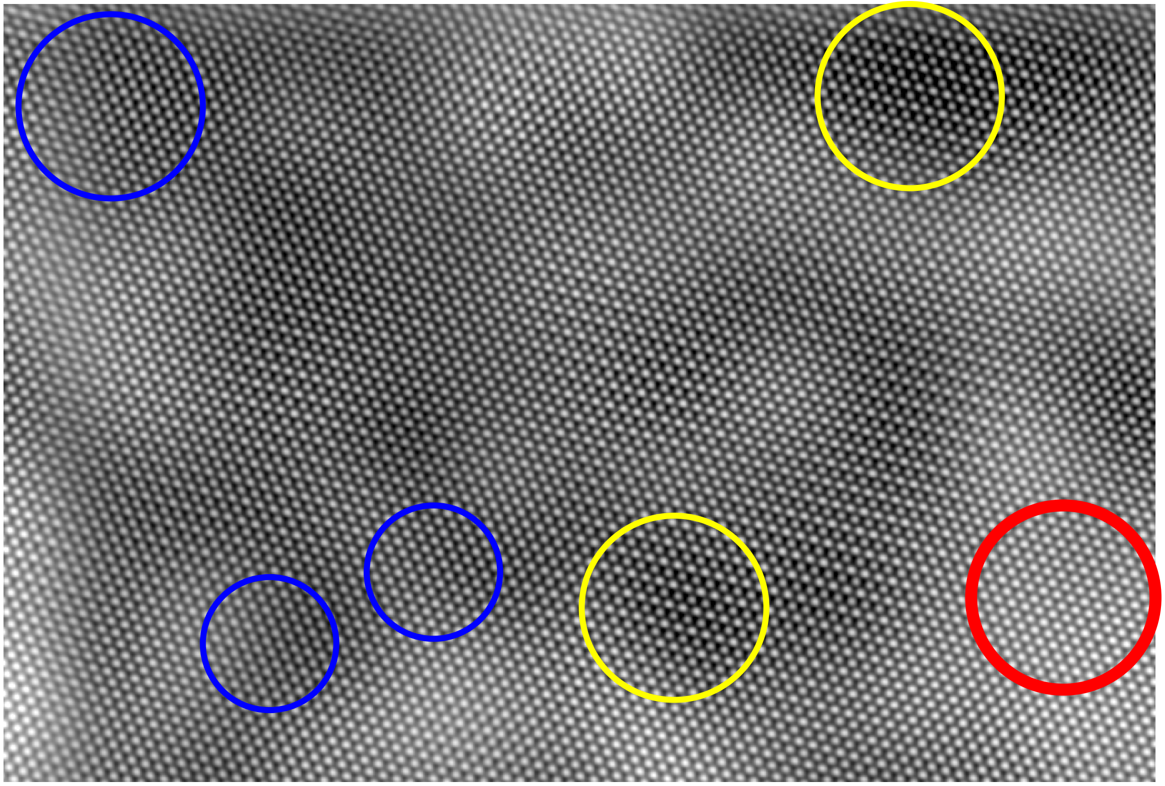

Figure 7.7. Filtered HAADF-STEM image showing dark-disordered (blue), dark-ordered (yellow) and bright-disordered (red) regions.

A closer examination of the HAADF-STEM micrograph differentiates the three regions; yellow circles encompassing ordered dark, blue circles encompassing disordered dark and red circle encompassing disordered bright regions as shown in Fig. 7.7. As per the previous atom probe investigation and the TEM analysis, these regions can be uniquely correlated with a particular phase transformation mechanism discussed later in the chapter. The patchy contrast exhibited by the micrograph doesn't follow any specific direction and seems to be randomly distributed. In addition, the variation within darker contrast should not be correlated with variation in Z (atomic mass) as variation in size and some overlapping of the matrix may also result in the variation. Therefore to avoid any confusion these regions would only be treated as dark ordered, dark disordered and bright disordered regions.

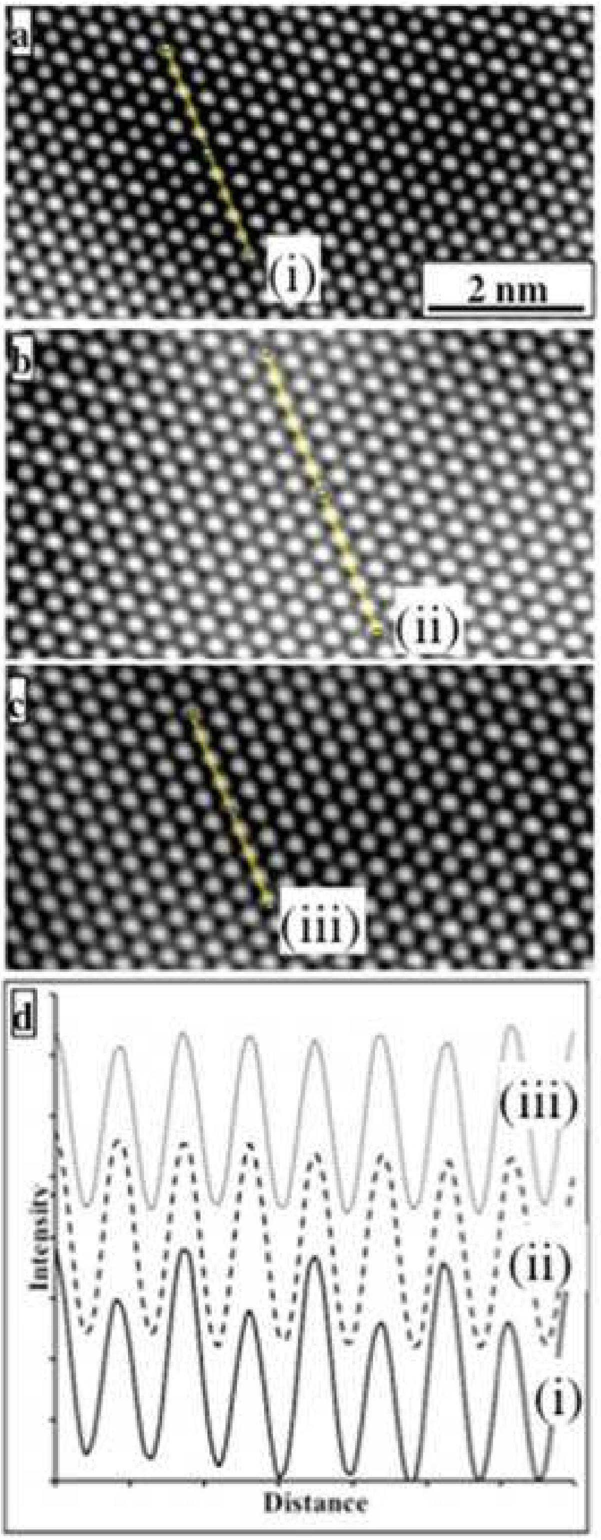

Figure 7.8. (a) Dark ordered region (b) bright disordered region (c) dark disordered region. (d) Intensity profiles along <002> direction in dark-ordered, bright disordered and dark disordered regions.

A more detailed analysis of the ordered and disordered structures present within different regions of the fcc γ matrix can be done using intensity profiles to obtain ordering-disordering nature of different regions more qualitatively as shown in Fig. 7.8(a), (b) and (c). The corresponding intensity profiles, plotted along the <111> fcc direction (marked with a line in each figure) for each of these regions is shown in Fig. 7.8(d), confirming the ordered and disordered regions. Fig. 7.8(d) shows that intensity profile for different regions. A periodic variation in the intensity is observed for case (i) which is dark whereas no periodic variation of intensity is observed for case (ii) which is bright or case (ii) which is dark. These observations as well as other similar analyses carried out on different regions of the fcc matrix are indicative of a particular transformation sequence. As summarized by Soffa and Laughlin [3] there could be different transformation sequences that can exist leading to the precipitation of γ′. However, as evident from the HAADF-STEM and atom probe tomography results the mechanism has to involve spinodal decomposition of the matrix. Thus, the two possible transformation sequences are, congruent ordering within the entire matrix followed by phase separation (via spinodal decomposition) and subsequent disordering of the phase that reaches closer to γ′ composition, or phase separation followed by ordering of phase that reaches closer to γ′ composition. In terms of contrast levels, the former sequence that involves ordering prior to phase separation would result in all regions exhibiting dark contrast being ordered. This is because; once ordering occurs the phase separation would result in two compositionally different phases that are ordered. In other words both dark and bright regions would be ordered after phase separation. Subsequently, only the bright region would get disordered. Therefore no region that is close to γ composition will be disordered and therefore all dark regions would be ordered. In contrast, the latter sequence would result in some regions exhibiting dark contrast being ordered (complete transformation sequence) while other dark regions are disordered (incomplete sequence), as observed in the present case. This is because; when phase separation occurs prior to ordering all regions would be disordered. The regions that are reach γ' composition get ordered and regions that are near to γ' composition but not yet reached the γ' composition would still appear dark and ordered. This particular transformation sequence would result in the microstructure as shown by HAADF-STEM.

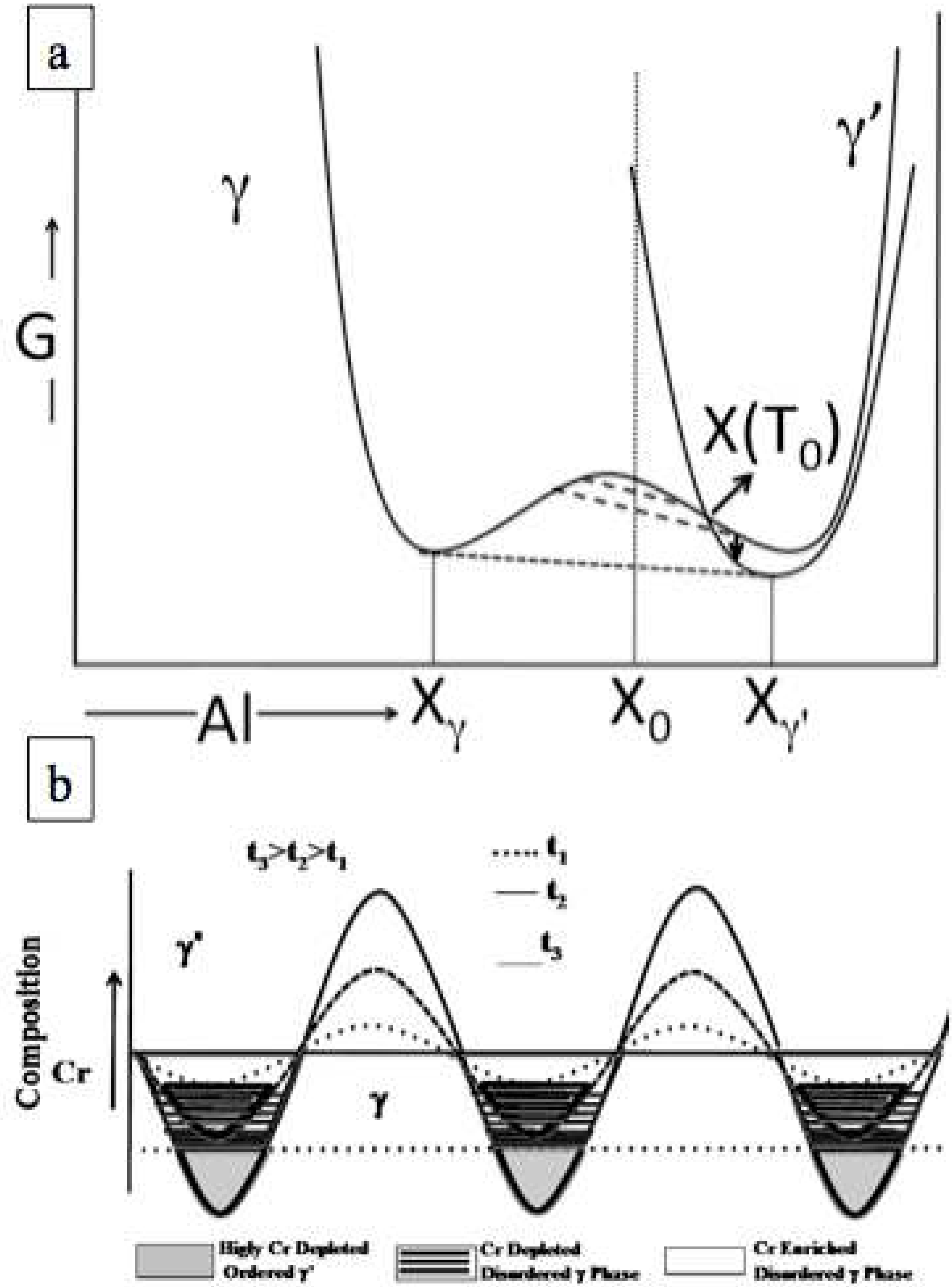

Figure 7.9. (a) Simplified G-X plot showing Order-Disorder transformation pathway, (b) Schematic of growth of spinodal wave and ordering process with time.

The experimental observations presented can only be interpreted via a γ' precipitation mechanism involving a phase separation (via spinodal decomposition), creating nanoscale domains depleted in certain solute elements (e.g. Co, Cr, and Mo) while being enriched in other solute elements (e.g. Al and Ti) within the fcc γ matrix, which subsequently undergo an $L1_2$ ordering reaction to form nanoscale γ' precipitates. This mechanism can be simply illustrated based on schematic Gibbs free energy (G) – composition (X_{Al}) plots of the γ and γ' phases, at a low temperature (highly undercooled into the γ+γ' phase field) where a miscibility gap arises for the fcc γ phase, as shown in Fig. 7.9(a). Since the average composition of the Ni-base alloy (X_0) lies within the spinodal region of the γ miscibility gap, the γ phase is unstable with respect to compositional fluctuations leading to continuous phase separation. This leads to solute (Al) lean and solute-enriched domains within the matrix. The continually increasing amplitude and wavelength of the compositional modulations eventually lead to the solute-rich domains crossing the $X(T_0)$ point, providing a driving force for $L1_2$ ordering and the formation of nanoscale γ' precipitates. However, this ordering takes place at a composition far-from equilibrium as observed experimentally. Subsequent isothermal annealing is expected to increase the solute partitioning driving the composition of the γ' precipitates towards equilibrium. The compositional fluctuation leading to phase separation can also be explained by a schematic of spinodal decomposition as shown in Fig. 7.9(b). As seen in the figure the compositional wave changes with time ($t_3 > t_2 > t_1$). The amplitude of the concentration increases with time. Initially when the spinodal starts due to small amplitude the contrast due to very small changes will not be observed. However, with increase in time, as phase separation grows, some regions get richer in Al (depleted in Cr) and appear darker. With time, this modulation reaches a critical composition of Al and Cr (hypothetical) which results in some regions getting ordered.

7.4 Growth of γ' Precipitates During Isothermal Annealing

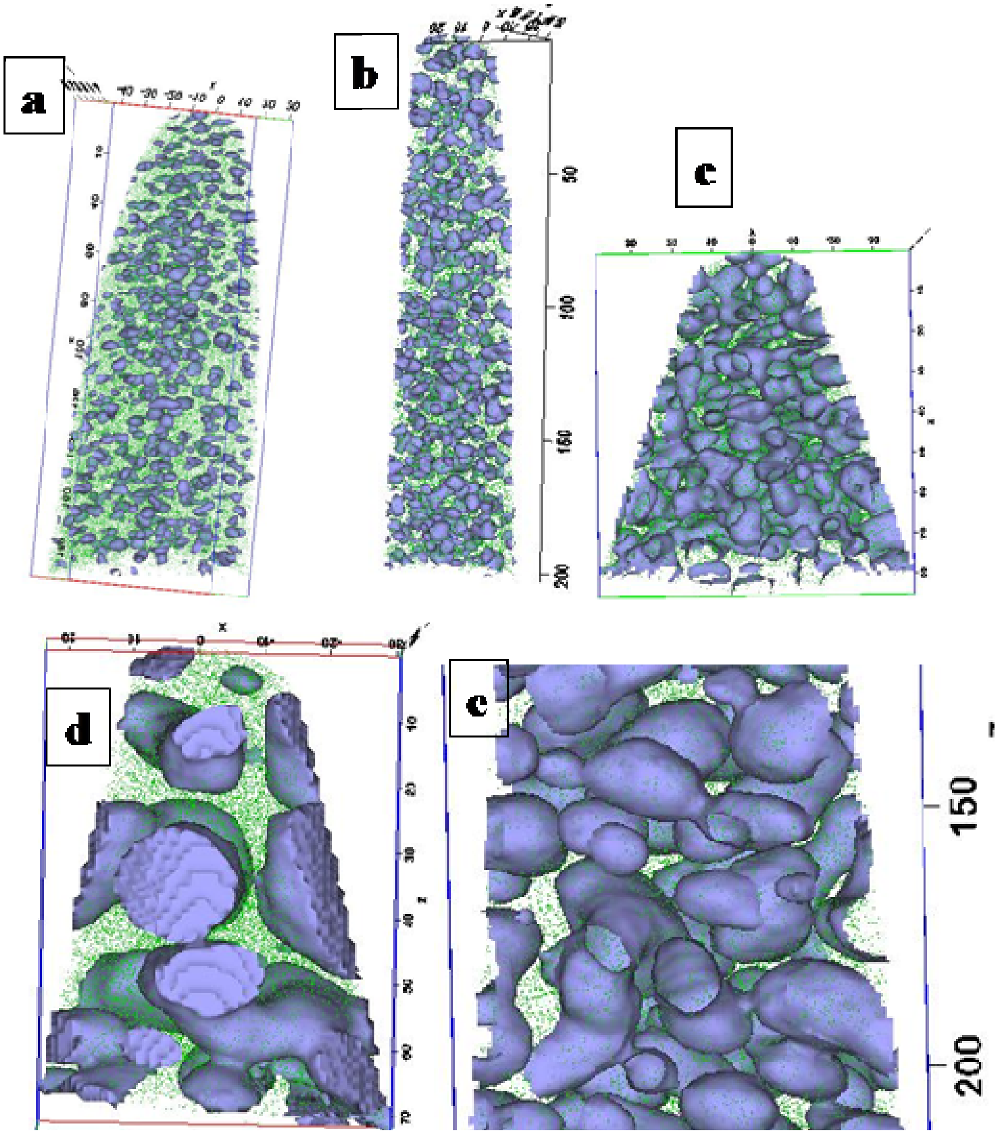

Figure 7.10. 3DAP reconstruction showing Ni ions and in green and Cr 14at% isosurface for (a) EWQ, (b) EWQ + 1 min, (c) EWQ + 5 min, (d) EWQ + 30 min and (e) EWQ + 60 min aged, sample.

The growth of spinodal resulting in increase in degree of chemical partitioning of elements between different phases was observed by aging the extreme water quenched alloy at 760^{o}C for different time periods; 1min, 5min, 30min and 60min. Fig. 7.10 shows the atom probe reconstruction of EWQ with different aging time using Cr = 14 at% isosurface which delineates the γ and γ' phases. Fig. 7.10(a), (b), (c), (d) and (e) correspond to atom probe reconstruction of EWQ specimens quenched and aged at 760°C for 0, 1min, 5min, 30min and 60min respectively. The reconstructions clearly show the interconnectivity of the phase separated regions continuously increasing with aging time. This gives an indication of the growth of spinodal decomposition. The size of the phase separated pockets also seem to be increasing, indicating that the volume fraction of the phase separated regions is increasing with time. This also shows that, the interaction of the diffusion field around the phase separated regions increases with time. It is difficult to measure the size distribution of these regions using atom probe, due to their high volume fraction and interconnectivity which makes it impossible to isolate the regions. This is also true for a spinodally decomposed structure where the composition waves would interact with each other and form a 3 dimensional interconnected network. Initially, in water quenched situation the γ' phase domains are isolated in the γ matrix, which increase in size on aging for 1min. However, after aging for 5min these γ' domains start interacting with each other and form an interconnected network, which grows upon further aging. It is important to note that the isolated nature of γ' domains is not a true representation of phase separation. It was shown in earlier section using HAADF-STEM and atom probe 2-D results that the phase separation is continuous and interconnected and only the ordered regions might be isolated.

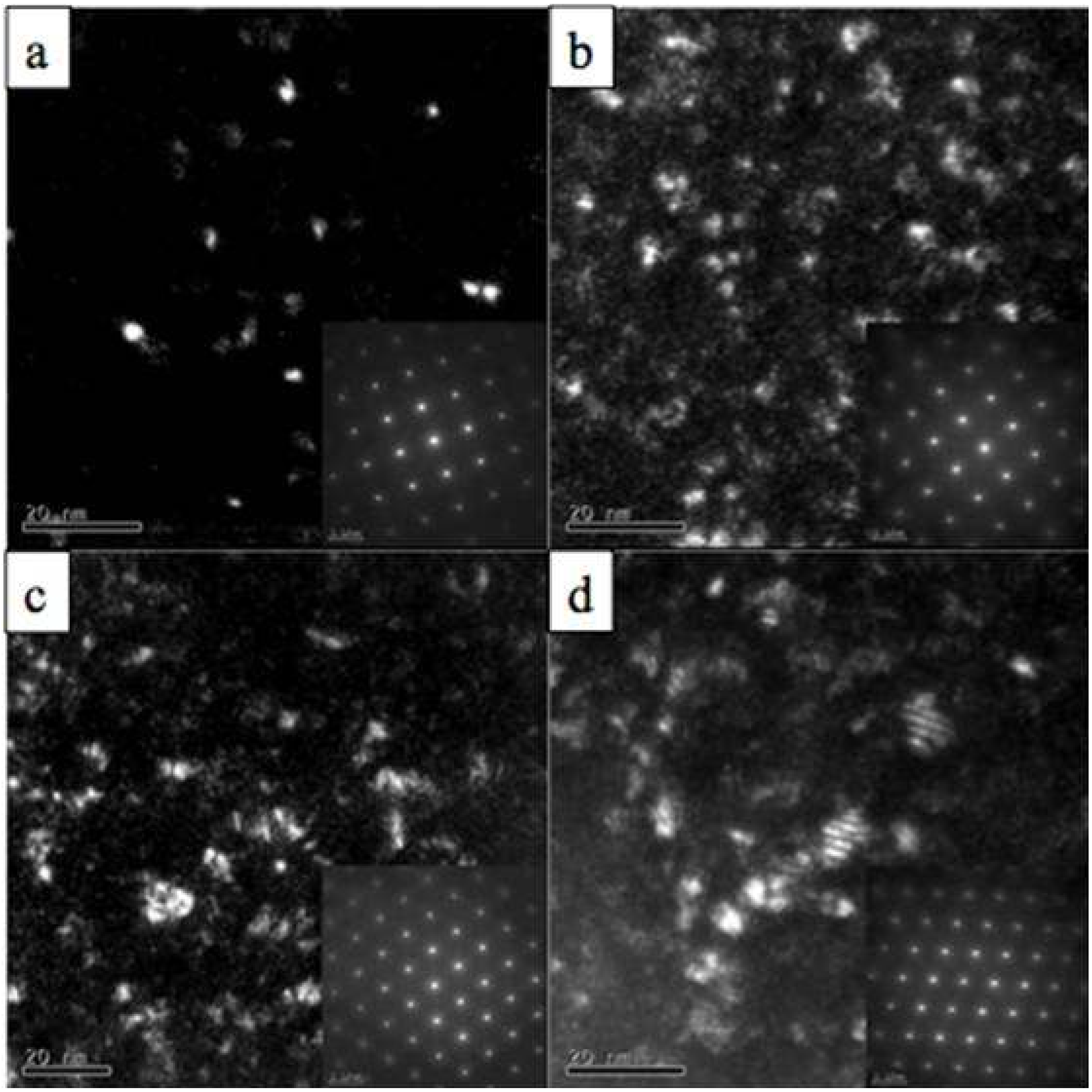

Figure 7.11. Dark field image taken along <001> zone showing ordered γ' in (a) EWQ + 1min aged, (b) EWQ + 5min aged sample. Dark field image taken along <011> zone showing ordered γ' in (c) EWQ +30 min aged, (d) EWQ + 60min aged sample.

High magnification dark field images are shown in Fig. 7.11(a), (b), (c) and (d) for different heat treated conditions; EWQ + 1min, 5min, 30min and 60min respectively. The images clearly show that the size of the ordered γ' precipitates have increased with aging time and the interconnectivity of the ordered regions has also increased. These results complement the results of atom probe analysis that showed increase in interconnectivity of phase separated region with increase in aging time period. Inset for each condition shows that selected area diffraction pattern. The SAD for water quenched and 1 and 5min aging were taken along <001> direction as shown in the inset showing four fold symmetry and for 30min and 60min were taken along <011> direction exhibiting two fold symmetry. The SADs show faint super lattice reflections showing the ordered nature of γ' precipitates. It was evident from HAADF-STEM analysis that in EWQ conditions the γ' precipitates were all discrete and only the phase separation was interconnected. Even after aging for 1 and 5min, the ordered γ' precipitates appear to be separated as shown in Fig. 7.11(a) and (b). However, after aging for 30min and 60min the γ' precipitates start getting interconnected as shown in Fig. 7.11(c) and (d). It has to be kept in mind that these dark filed images were taken using single variant of <001> and therefore there could be lot more γ' precipitates present in the sampled area. Hence these images are not a true quantitative representation of the number of precipitates in the sample, rather a qualitative analysis. From the dark field images it also appears that size of the γ' precipitates has also increased.

As only one of the variants was selected for dark field study, a semi quantitative analysis of the γ' particle size was done. The dark field images were converted to binary images and threshold was done to create black γ' precipitates in white matrix. ImageJ software was used to measure the particle sizes and a distribution of particle size was plotted for 1min, 5min and 30min aged condition. Normalized frequency distribution for γ' precipitates for different heat treated conditions is shown in Fig. 7.12(a), (b) and (c). A gaussian fit for the size distribution is also shown in the respective histograms. As can be seen from the histograms, the precipitates show a unimodal size distribution for different heat treatments. In addition to that, the peak of the gaussian shifts toward the right with increase in aging time which gives an indication that size of the γ' precipitates is increasing with aging time. Xc is approximately constant for 1, 5min however huge change is observed in 30min; 1.9 and 1.7 and 2.9 respectively which shows that there is increase in size of γ' precipitates corresponding to maximum number of precipitates. The width of the gaussian changes significantly from 1 to 30min showing significant increase in size of the γ' precipitates. Therefore, from size distribution analysis of γ' precipitates it can be concluded that , there is a significant increase in size of γ' precipitates from 5 to 30min aging, also seen from the dark field TEM images. A significant change in the interconnectivity of the γ' precipitates can also be observed as the water quenched sample is aged for long times (30min) which can result in the increase in the size of precipitates and width of the gaussian.

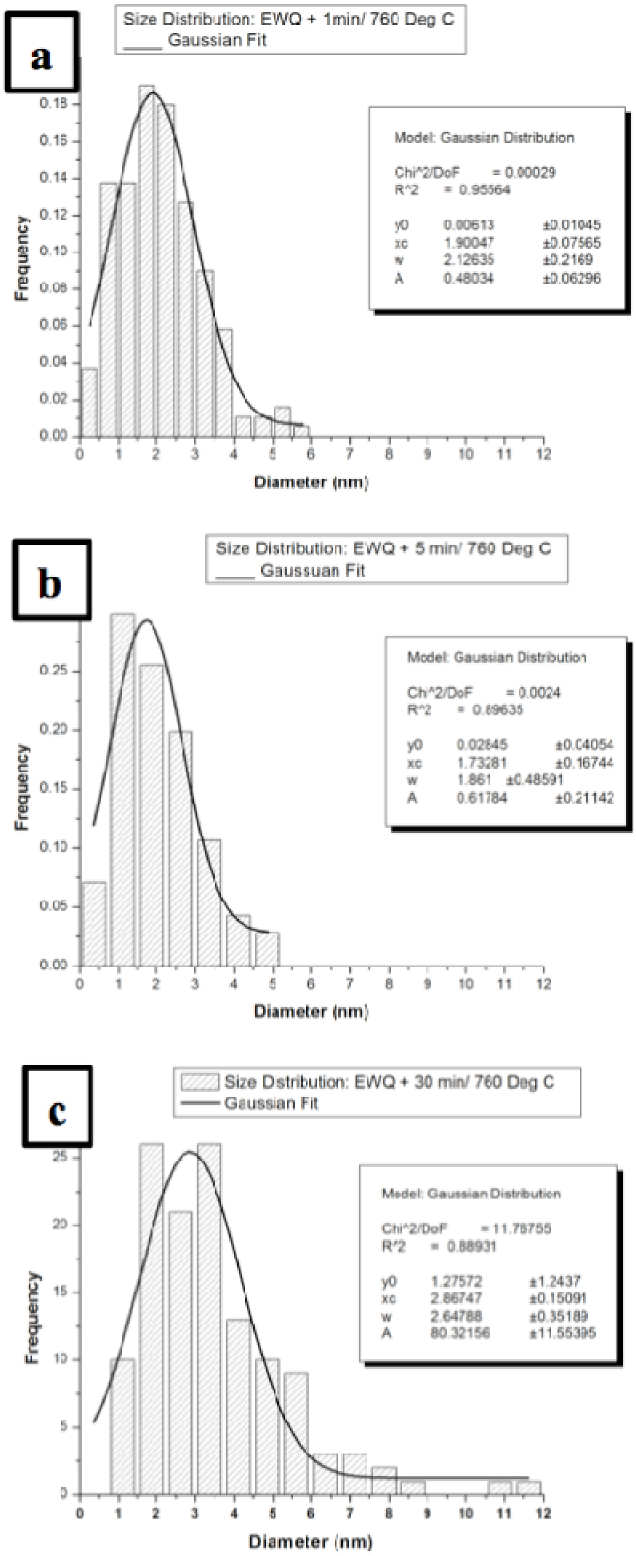

Figure 7.12. Frequency size distribution of γ′ precipitates using dark field imaged for (a) EWQ + 1min, (b) EWQ + 5min, and (c) EWQ + 30min condition.

The Cr = 14at% isosurface showed the increase in chemical partitioning between γ′ and γ. It was also concluded from the earlier results that aging up to 5min increased the size of the γ′ but did not create an interconnected morphology of the ordered regions. The proximity histogram that represents the profile of chemical partitioning between γ′ and γ was used to see the change at the interface with increase in aging time. Bin width of 0.2nm was used to measure the composition change across the interface. Fig. 7.13(a), (b), (c), (d) and (e) show the proximity histogram for Cr = 14at% isosurface between γ′ and γ for sample extreme water quenched and aged for 0, 1, 5, 30 and 60min respectively. From Fig. 7.12(a) and (b) it is evident that initially the compositional gradient across the interface is very broad and both γ′ as well and γ do not attain steady state compositions away from the interface. Local enrichment of Cr and Co is also observed in these condition and this enrichment decreases sway from the interface due to highly non equilibrium composition in the matrix. With aging time as the precipitates grow, the partitioning across the interface reaches closer to the equilibrium as can be seen in Fig. 7.13(c), (d) and (e) and the interface gets sharper. The increase in partitioning across the interface with time can be directly related to the increase in amplitude of the spinodal concentration wave. The diffuseness of the interface which gets sharper with time also gives an indication of the growing spinodal decomposition. Ultimately the compositions in the matrix and precipitate reach steady state as can be seen in Fig. 7.13(d) and (e) and the interface becomes sharp. However, the compositions in the γ regions still maintain non equilibrium conditions.

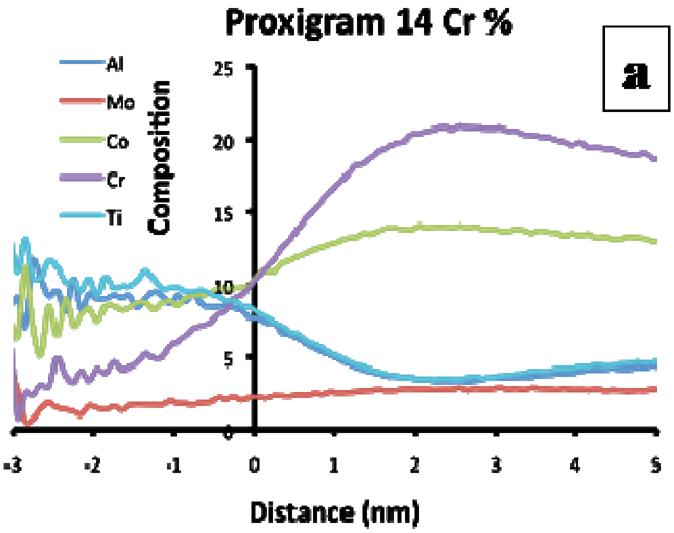
Proximogram 14 Cr %
a
Al
Mo
Co
Cr
Ti
Composition
25
20
15
10
5
0
-3
-2
-1
0
1
2
3
4
5
Distance (nm)

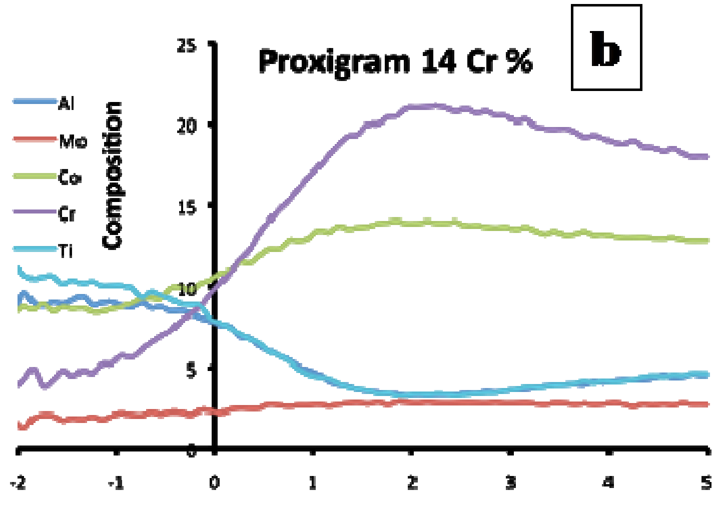
Proxigram 14 Cr %
b
Al
Mo
Co
Cr
Ti
Composition
25
20
15
10
5
0
-2
-1
0
1
2
3
4
5
Distance (nm)

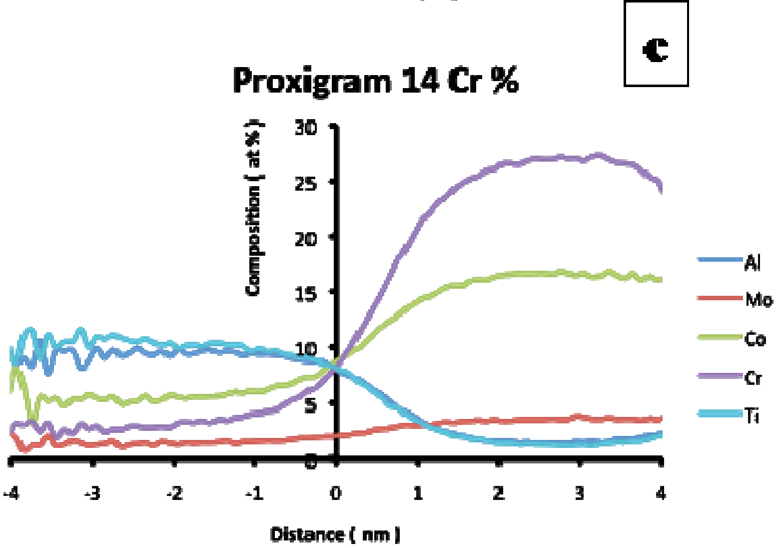
c
Proxigram 14 Cr %
Composition (at %)
30
25
20
15
10
5
0
-4
-3
-2
-1
0
1
2
3
4
Distance (nm)
Al
Mo
Co
Cr
Ti

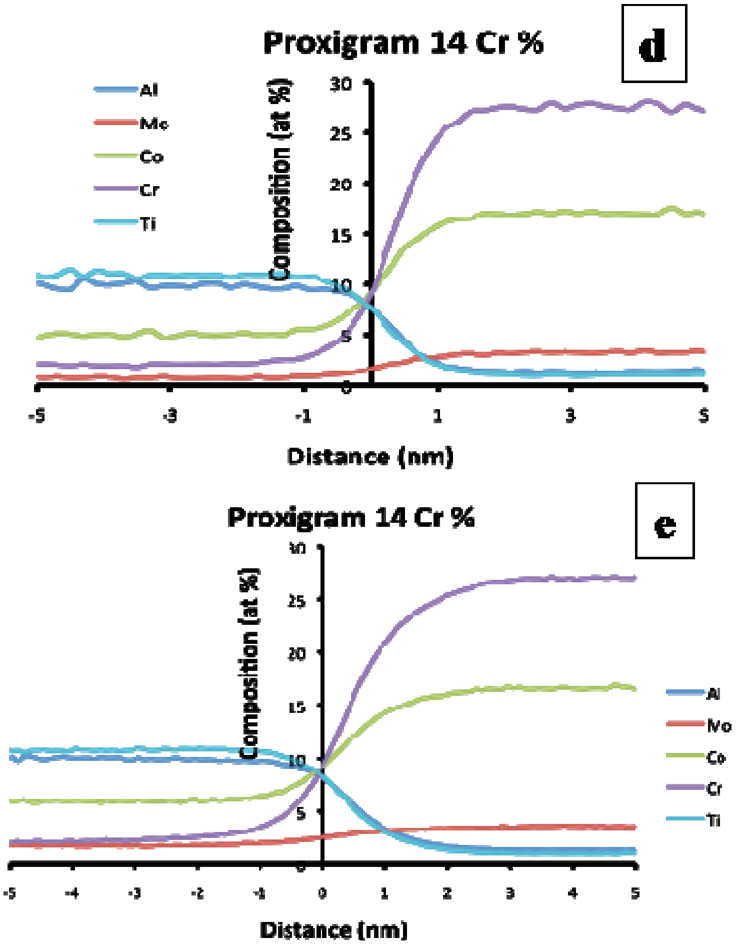

Figure 7.13. Proxigram of Cr 14at% isosurface as a function of aging time, (a) EWQ, (b) EWQ + 1min, (c) EWQ + 5min, (d) EWQ + 30min and (e) EWQ + 60min aged sample.

The compositions of the γ′ and the γ phase were calculated by extracting the regions enclosed by Cr = 14at% isosurface in individual reconstruction and measuring their bulk compositions. The compositions obtained for γ′ and γ are summarized in Table 7.1 and 7.2 respectively. A progressive in crease in composition of concentrations of Al and Ti can be observed from 8.46at% to 10.56at% and 9.33at% to 10.27at% respectively. The compositions of Cr and Co significantly decrease from 7.57at% to 2.88at% and 9.29at% to 5.96at% respectively. Hence, the γ′ get richer in Al and Ti and get depleted in Co and Cr with aging as the amplitude of spinodal increases. Similarly composition of γ also shows a similar trend as shown in Table 7.2.

The concentrations of Al and Ti in γ decrease from 4.05at% to 2.79at% and 4.27at% to 2.21at% respectively. The concentrations of Cr and Co on the other hand increase from 19.28% to 21.32at% and 13.48at% to 15.11at% respectively. The concentration of Mo in γ′ and γ shows minimal change due to low diffusivity. These results also indicate that the partitioning of elements at lower temperature is achieved by spinodal decomposition.

Table 7.1. Composition of γ′ as a function of aging time.

γ' Comp	**EWQ**		**EWQ + 1**		**EWQ + 5**		**EWQ + 30**		**EWQ + 60**	
Ion Type	**Comp. at. %**	**Error**	**Comp. at. %**	**Error**	**Comp. at. %**	**Error**	**Comp. at. %**	**Error**	**Comp. at. %**	**Error**
Al	**8.46**	**0.04**	**8.41**	**0.03**	**9.51**	**0.03**	**10.32**	**0.04**	**10.56**	**0.01**
Ti	**9.33**	**0.04**	**9.09**	**0.03**	**9.47**	**0.03**	**10.22**	**0.04**	**10.27**	**0.01**
Co	**9.29**	**0.04**	**9.64**	**0.03**	**6.41**	**0.02**	**5.62**	**0.03**	**5.96**	**0.01**
Cr	**7.57**	**0.03**	**7.27**	**0.03**	**5.16**	**0.02**	**3.02**	**0.02**	**2.88**	**0.01**
Mo	**2.01**	**0.02**	**2.20**	**0.01**	**2.36**	**0.01**	**0.98**	**0.01**	**2.46**	**0.01**

Table 7.2. Composition of γ as a function of aging time.

γ Comp	**EWQ**		**EWQ + 1**		**EWQ + 5**		**EWQ + 30**		**EWQ + 60**	
Ion Type	**Comp. at. %**	**Error**	**Comp. at. %**	**Error**	**Comp. at. %**	**Error**	**Comp. at. %**	**Error**	**Comp. at. %**	**Error**
Al	**4.05**	**0.01**	**4.03**	**0.01**	**3.07**	**0.01**	**2.36**	**0.01**	**2.79**	**0.00**
Ti	**4.27**	**0.01**	**4.03**	**0.01**	**2.94**	**0.01**	**1.80**	**0.01**	**2.21**	**0.00**
Co	**13.48**	**0.01**	**13.42**	**0.01**	**14.67**	**0.02**	**16.06**	**0.03**	**15.11**	**0.01**
Cr	**19.28**	**0.02**	**19.28**	**0.02**	**22.10**	**0.03**	**24.60**	**0.04**	**21.32**	**0.01**
Mo	**2.72**	**0.01**	**2.76**	**0.01**	**3.16**	**0.01**	**3.23**	**0.01**	**4.04**	**0.00**

The compositions of γ' and γ as a result of spinodal decomposition were calculated using Cr = 14at% iso-concentration surface. However, a more statistical method to represent a spinodal decomposition of a homogenous alloy was developed by Langer, Baron and Miller also known as LBM method [23]. This method assumes a homogenous distribution of elements in a reconstruction and divides the reconstruction into small bins and calculates frequency and composition of each bin such that the distribution of these bins can be represented by a gaussian curve. A homogeneous alloy would show a normal distribution of the bins, whereas a spinodally decomposed alloy would deviate from a normal. Normalized LBM is shown in Fig. 7.14 for different aging time for Cr. As evident from the frequency distribution, EWQ does not show any split, however it is not a perfect normal. With aging a clear spilt in the peaks can be seen resulting from increase in phase separation. At 5 minutes of aging a huge split in the peaks corresponding to phase separation can be observed which increases in amplitude at 30 minutes and remains almost constant on further aging. This shows that huge compositional fluctuation takes place after 5min of aging up to 30min. A more quantitative analysis of this distribution can be done by fitting a gaussian to the raw data. Any deviation from normal can be represented by combination of two gaussians. The results of the gaussians are summarized in Table 7.3 which gives the mean composition of the gaussian corresponding to composition of γ' and γ and the area under each gaussian corresponds to the volume fraction of each phase. It is evident from the results that the Cr composition increases in γ from 19.4at% to 24.7at% and decreases in γ' from 9.4at% to 4.7at% with increase in aging time. The volume fraction of γ' also increases from 10% to 35% and volume fraction of γ decreases from 90% to 65% respectively. The results also suggest that after 1 hour of aging the γ a γ' phases do not reach equilibrium composition and volume fraction. Interestingly, aging for 1 minute does not changes the composition of the phase separated regions, in fact the volume fraction of the phase separated regions increases after which a continuous change in composition and volume fraction of phase separated regions occurs. Therefore, this analysis gives true representation of the spinodal decomposition resulting in the formation of γ'.

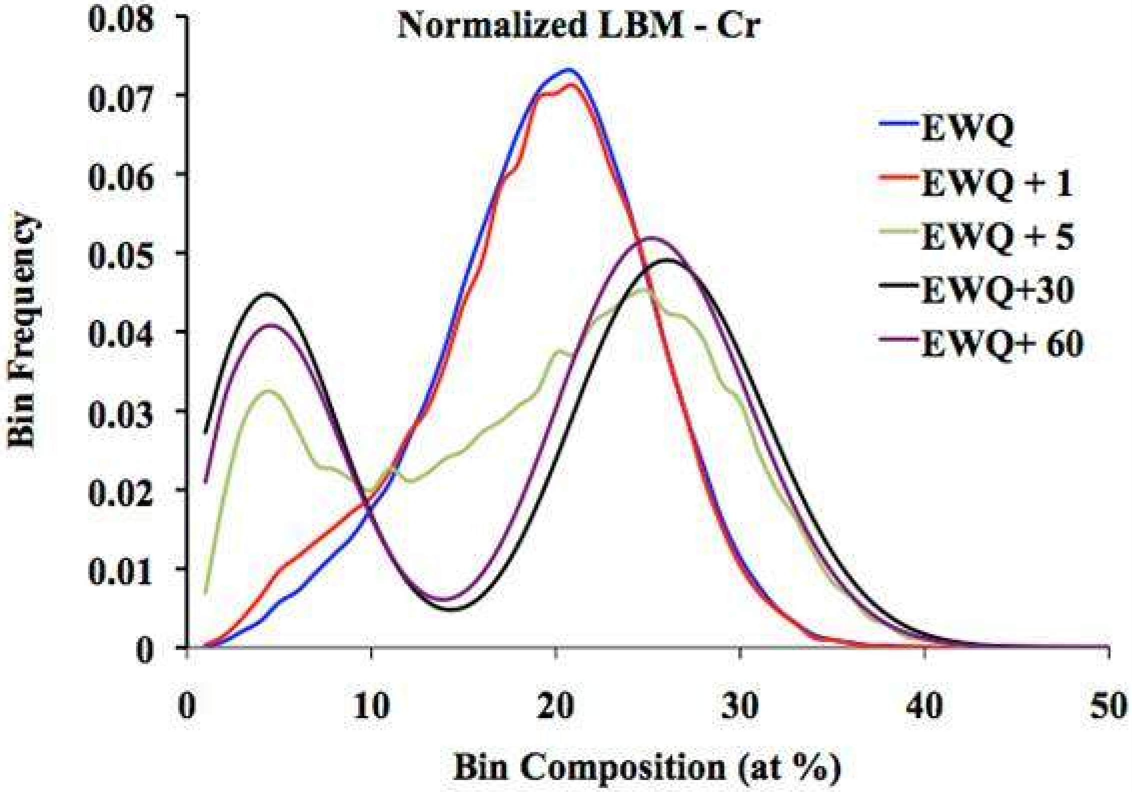

Figure 7.14. Normalized LBM plot showing phase separation of Cr with aging.

Table 7.3. Composition of Cr rich and Cr depleted regions and their volume fraction predicted by LBM.

LBM	**Cr Composition**		**Volume fraction**	
Condition	**γ′** **(at %)**	**γ** **(at %)**	**γ′**	**γ**
EWQ	9.4	19.4	10	90
EWQ + 1min	9.1	20.1	18.2	81.8
EWQ + 5min	8	24	37.5	62.5
EWQ + 30min	4.5	25.5	38.1	61.9
EWQ + 60min	4.7	24.7	35	65

7.5 Summary

This chapter presents, for the first time, atomic resolution evidence of synergistic spinodal decomposition and chemical ordering within a metallic solid solution. The specific example of a Ni-base superalloy highlights the important role played by prior phase separation within the fcc γ solid solution matrix resulting in appropriate nanoscale compositional domains within which ordering can take place. HAADF-STEM gives a true atomic level Z contrast which gives a direct evidence of phase separation and together with atom probe tomography this phase separation was quantified. The size scale of phase separated pocket encapsulated by Cr = 18at% isosurface is same as that of γ' domain in HAADF-STEM for EWQ condition. The composition of these pockets is far from equilibrium and get closer to equilibrium with aging. Aging up to 1 hour at 760^{o}C shows a continuous increase in Al and Ti in γ' and reduction in Cr and Co giving evidence of spinodal decomposition. The volume fraction of Al and Ti rich regions also increases with aging which also gives an indication of spinodal growth.

7.6 References

[1] W.A. Soffa, D.E. Laughlin, Proc. Int. Conf. Solid-Solid Transformations, ed. H.I. Aaronson, D.E. Laughlin, R.F. Sekerka and C.M. Wayman, TMS, Warrendale, Pennsylvania, 159 (1982)

[2] D.E. Laughlin, W.A. Soffa, Physical Properties and Thermodynamic Behavior of Minerals, NATO ASI Series C, Vol. 255, ed. E.K.H. Salje, D. Reidel, Dordrecht, 213 (1988)

[3] W.A. Soffa, D.E. Laughlin, Acta Metall. 37 (1989) 3019

[4] S. Allen, J.W. Cahn, Acta Metall. 24 (1976) 425

[5] W.O. Gentry, M.E. Fine, Acta Metall. 20 (1972) 181

[6] C.L. Corey, B.Z. Rosenblum, G.M. Greene, Acta Metall. 21 (1973) 837

[7] K. Saito, R. Watanabe, Japan J. Appl. Phys. 8 (1969) 14

[8] R. Sinclair, J.A. Leake, B. Ralph, Phys. Status Solidi. 264 (1974) 285

[9] D.E. Laughlin, J.W. Cahn, Acta Metall. 23 (1975) 329

[10] D.E. Laughlin, J.W. Cahn, Met. Trans. 5 (1974) 492

[11] J.C. Zhao, M.R. Notis, Acta Mater. 46 (1988) 4203

[12] A.J. Ardell, R.B. Nicholson, Acta Metall.14 (1967) 1295

[13] H. Wendt, P. Haasen, Acta Metall. 31(1983) 1649

[14] S.A. Hill, B. Ralph, Acta Metall. 30 (1982) 2219

[15] W.O. Gentry and M.E. Fine, Acta Metall. 20 (1972) 181

[16] S.T. Wlodek, M. Kelly, D.A. Alden (1996) In: R. D. Kissinger, D.J. Deye, D.L. Anton, A.D. Cetel, M.V. Nathal, T.M. Pollock, D.A. Woodford (ed) Superalloys 1996, TMS, Warrendale, PA (1996) 129

[17] K. Thompson, D. Lawrence, D.J. Larson, J.D. Olson, T.F. Kelly, B. Gorman, Ultramicrosco. 107 (2007) 131

[18] D.E. Laughlin, Acta Metall. 24 (1976) 53

[19] A.J. Ardell, R.B. Nicholson, Acta Metall. 14 (1966) 1295

[20] J.W. Cahn, Acta Metall. 9 (1961) 795

[21] J.Y. Hwang, R. Banerjee , J. Tiley, R. Srinivasan, G.B. Viswanathan, H.L. Fraser, Metall. Mater. Trans. A. 40 (2009) 24

[22] J.Y. Hwang, S. Nag, A.R.P. Singh, R. Srinivasan, J. Tiley, G.B. Viswanathan, H.L. Fraser, R. Banerjee, Metall. Mater. Trans. A. 40 (2009) 3059

[23] J.S. Langer, M. Bar-on, H.D. Miller, Phys. Rev. A. 11 (1975) 141

CHAPTER 8

SUMMARY AND FUTURE WORK

The present research was focused on getting a new insight into the formation of different generations of γ' in Rene88DT. Initial investigation showed change in morphology, size and distribution of γ' precipitates with change in cooling rate using energy filtered transmission electron microscopy (EFTEM). It was also observed that the composition of the matrix and the γ' precipitates vary with cooling rate using atom probe tomography (APT). It was concluded that with decrease in cooling rate the size distribution changes from unimodal to multimodal and that the different size scales of precipitates had different morphologies. The multimodal distribution during slow cooling forms as a result of changing thermodynamic driving force and diffusivities in the matrix causing different nucleation bursts.

Further investigation of different generations of γ' revealed that each generation of γ' possesses different elemental composition. The γ' precipitates also called primary nucleate at high temperature and reach equilibrium composition (highly enriched in Al and Ti and depleted in Cr and Co) during slow cooling. However, due to changing diffusivities and build up of supersaturation in the γ matrix, the system nucleates further generations of γ' at low temperatures and due to limited growth, these precipitate maintain spherical morphology and non-equilibrium compositions. The system tries to reach equilibrium state by nucleation of multiple generations of γ' in a continuously changing environment. Therefore, the microstructure evolves during continuous cooling by formation of primary γ' precipitates, depletion zone and secondary and tertiary γ' precipitates. It was also found out that the compositional partitioning near between depletion region and secondary γ' had an interconnected nature.

The growth and coarsening of primary and secondary and tertiary γ' showed that that secondary and tertiary γ' grow and reach close to equilibrium composition after 15 hours of aging at 760°C whereas primary γ' coarsen and increase in size. The composition of primary γ' does not change with aging.

Finally, the atomic level characterization of the highly undercooled Rene88DT alloy showed that the γ' formation at lower temperatures occurs by non-classical nucleation as opposed to generally considered nucleation and growth mechanism. Using HAADF-STEM and APT the ordering and phase separation mechanisms were uniquely identified. It was postulated from the results that at γ' formation at low temperatures similar to tertiary γ' form as a result of spinodal decomposition. A particular phase transformation pathway was identified and shown that the phase separation in a supersaturated matrix occurs by spinodal decomposition first and the regions that get enriched in Al and Ti (depleted in Cr and Co) then undergo ordering process to form ordered γ' with non equilibrium composition. Aging the EWQ sample for different time periods showed the amplitude of spinodal decomposition growing with time. The interfaces of primary and tertiary γ' precipitates with the matrix during slow cooling are sharp and diffused showing classical and non-classical nucleation phenomenon respectively.

However, more research needs to be done to understand the precipitation mechanism of γ'. From the results obtained, huge scope for further research is seen as mentioned below:

(i) Step quench experiments can be done to capture each generation of γ' and individually study the formation of secondary and tertiary γ' precipitates. This would help in finding out the temperatures of each nucleation event and their nucleation mechanism.

(ii) Since the partitioning of elements is quite complex, the effect of different elements can be understood by choosing simpler ternary system and investigate the role of each alloying addition in phase separation and ordering process.

(iii) Faster quenching can be done to retain the disordered γ phase and subsequently annealed for different time periods to investigate the order-disorder transformation and by changing the composition (equilibrium volume fraction) the change in phase transformation mechanisms can be investigated.